9 Single Rotor Machines

9.1 MODELING OF PROCESSING MACHINES USING ELEMENTARY STEPS

By dissecting polymer processing into *elementary steps*, and analyzing each step in isolation, we are able to uncover the underlying, basic mechanisms of each individual step, and its theoretical foundation. As we discussed in Section 2.11, this process is part of a systematic scientific methodology for modeling any complex system. In our case, the complex system is the polymer processing discipline as a whole. Along similar lines, we showed in Section 6.2 that the machines themselves can also be dissected or ''deconstructed'' into basic elements and building blocks, which capture the basic underlying mechanism or essence of a particular machine. We further showed in Section 6.2 that we can synthesize new machines by systematically and rationally recombining the building blocks in imaginative ways.

In this chapter and in Chapter 10, we *synthesize* or *design* prototype polymer processing machines using these elementary steps and building blocks. The uniqueness of each prototype machine is determined by the *building blocks* of the machine itself, and the particular combination of elementary steps and elementary-step mechanisms utilized to create it.

However, once we have conceptually designed the prototype machine, which involves selecting the elementary steps and the particular mechanisms we wish to use, and describing them in terms of mathematical subsystem models, we can assemble them into a comprehensive *mathematical model* of the whole machine and proceed through *simulation* to design-specific machines for given sets of requirements.[1]

This chapter focuses on single rotor machines. Specifically, we analyze the single screw extruder (SSE) and the co-rotating disk processor (CDP). The former, based on two parallel plates in relative motion (building block 1 in Fig. 6.2) was chosen not only because it enjoys a dominant role in the processing industry, and therefore ought to be studied by all processing engineers, but also because of its inherent capability to perform *all* the elementary steps of polymer processing. Indeed, the versatility of the SSE, coupled with its design simplicity, is what makes it so useful. The CDP, based on jointly moving parallel

1. It is worthwhile noting that polymer processing was among the first engineering disciplines in which comprehensive mathematical modeling was used for the design of machines. This was pioneered by Imrich Klein and Donald I. Marshall in their book *Computer Programs for Plastics Engineers*, Reinhold, New York, 1968.

Principles of Polymer Processing, Second Edition, by Zehev Tadmor and Costas G. Gogos.

plates (building block 2 in Fig. 6.2), was chosen because it can also perform all the elementary steps in a radically different geometrical configuration, and the juxtaposition of these two very different machines helps gain better insight into each of them.

9.2 THE SINGLE SCREW MELT EXTRUSION PROCESS

Melt-fed SSEs are used in *post–reactor processing*. This involves three stages: (a) compounding of various additives into the polymer after it exits the reactor; (b) pressurization of the melt; and (c) pelletizing of the polymeric melt. The compounding takes place in either a batch mixer (e.g., Banbury-type internal mixer) or a continuous mixer (CM), feeding an SSE equipped with a pelletizing plate. An alternative solution calls for using a twin screw extruder (TSE) equipped with kneading elements that compounds, pressurizes, and pelletizes the polymeric melt.

In this section, we discuss the design of a melt extruder and derive the appropriate mathematical model. This will also introduce the reader to the plasticating extrusion process discussed in the following section.

Figure 9.1 shows a schematic view of a metering-type melt extruder, consisting of a deep channel feed section, a compression section, and a shallow metering section. The geometrical variables that must be specified to cut a screw are depicted in the figure, and they include the screw diameter, D_s, the total length and the flighted length, L, the length or number of turns in each geometrical section (feed, tapered, and metering), the lead, L_s, the feed depth, the metering depth, and the flight width, e. In addition, one must specify the shank and the bearing diameters, the keyway, the feed pocket, the front and rear radii, and the nose cone, but these do not affect simulation within the accuracy of the existing models.

The screw is placed within a barrel of diameter $D_b = D_s + 2\delta_f$, where δ_f is the radial flight clearance. This is shown schematically in Fig. 9.2. The figure shows a pelletizing extruder, but the discussion that follows is valid for *any* melt extruder equipped with any kind of die, and for the melt region in a plasticating extruder as well.

The *system* consists of three *subsystems*: the feed port, the screw, and the pelletizing plate, which are connected in *series*. Therefore, for steady state operation with atmospheric inlet and outlet conditions, the mass flow rate in each subsystem G_i is constant

$$G_i = G_0 \tag{9.2-1}$$

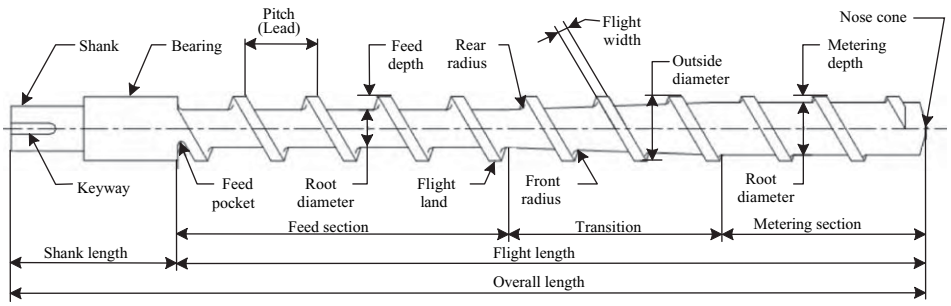

Fig. 9.1 A metering-type screw indicating the geometrical variables that must be specified for cutting a screw, and their common names.

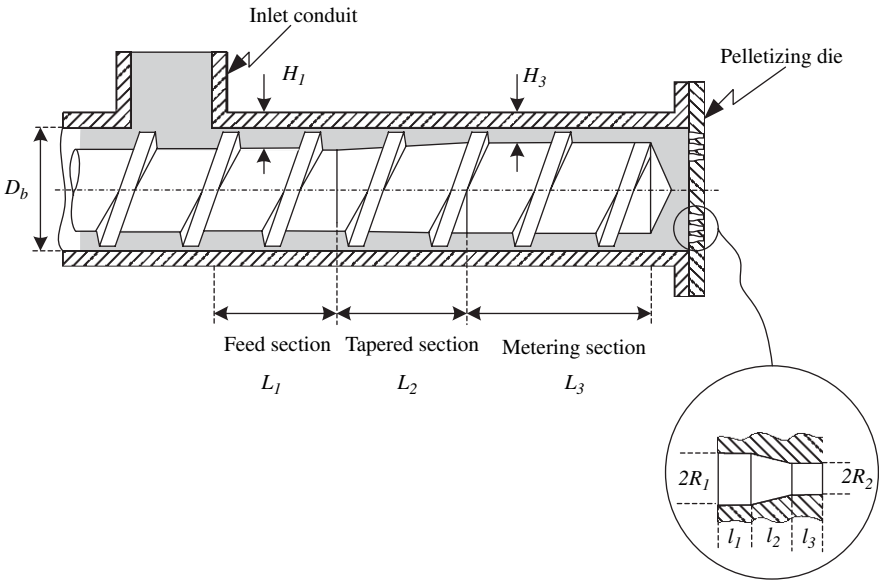

Fig. 9.2 Schematic view of a melt extruder. The extruder is equipped with a feed port and a pelletizing plate.

where G_0 is the throughput, and the sum of pressure changes over the entire process is zero

$$\Delta P_i = 0 \tag{9.2-2}$$

which implies that the pressure *rise* in the extruder equals the pressure *drop* over the pelletizing plate. In designing a pelletizing system, therefore, we first of all need to relate flow rate to pressure change over each subsystem. However, the mass flow rate or throughput and pressure changes are not the only operational variables of interest. Linked to the pressurization step are also bulk temperature changes and temperature distributions, which may affect the uniformity of the pellets, and of course power input through the shaft of the extruder, which determines the size of the drive system. We may also be interested in the mean strain, strain, and residence time distribution functions.

The assembled models of the subsystems provide relationships between the main process variables mentioned earlier (flow rate, pressure profile, temperature profile, power requirements, residence time), the relevant geometrical variables (i.e., design variables), the rheological and thermophysical properties of the melt, and the main operational variables (i.e., frequency of screw rotation or ''screw speed,'' barrel temperature profile, and die temperature settings). These relationships can, therefore, be used both for new machine design or for the analysis (optimization) of existing ones. In addition to the main process variables, there are other variables that may be worthwhile studying, such as cross die variation in temperature (leading to uneven pellets), flow-rate fluctuations, swelling and shape stability, and parameter sensitivity of the process. Chapter 12, on die forming, deals with some of these issues.

The Isothermal Newtonian Model for Constant Channel Depth Screw

We now proceed to the main task of subsystem modeling. The inlet flow to the extruder is simple gravitational flow through (generally) a tubular conduit. In such slow flows, the shear rate range is very low and the isothermal Newtonian assumption is valid. For a vertical tubular entrance, the flow rate is given by the Haagen–Poiseuille law (Table 12.2)

$$Q = \frac{\pi(P_0 - P_L)R^4}{8\mu L_0} \tag{9.2-3}$$

where $P_z = P_0 - \rho g z$, z is the downward distance in the inlet conduit of height L_0. Therefore, for a melt column of height L_0, $P_0 - P_L = \rho g L_0$, and

$$Q = \frac{\pi\rho g R^4}{8\mu} \tag{9.2-4}$$

Drag-induced pressurization in shallow screw channels was discussed in Section 6.3, and the flow rate is given in Eqs. 6.3-27 and 6.3-28. The former can be rewritten as

$$Q_s = \frac{1}{2}\pi N D_b \cos\theta_b W\left(H - \delta_f\right)F_d - \frac{WH^3}{12\mu}\frac{\Delta P_s}{L}\sin\bar{\theta}(1 + f_L)F_p \tag{9.2-5}$$

where Q_s is the volumetric flow rate in the extruder, L is the axial length of the screw, ΔP_s is the pressure rise over the screw from inlet to exit, and f_L is given in Eq. 6.3-28. Note that in Eq. 9.2-5, we use an average helix angle to convert helical length to axial length; whereas, for the barrel velocity, we use the helix angle at the barrel inner surface. In developing Eq. 6.3-27, it was assumed that a congruent velocity distribution exists in the channel, and therefore, we neglected the end effects. However, in Eq. 9.2-5, we applied it to a finite-length screw. This introduces an error called the oblique end effect, as shown schematically in Fig. 9.3. This error is discussed by Tadmor and Klein (1) and was originally suggested by Booy (2). For low L/D screws, it may be important, and both pressure and drag flows have to be multiplied by correction factors, which are only functions of L/D and θ.

Equation 9.2-5 can be represented by plotting the flow rate Q_s versus the pressure rise ΔP_s. Such plots, called *screw characteristics*, appear in Fig. 9.4. The intersection with the ordinate gives the drag-flow rate value and that with the abscissa, the maximum pressure at closed discharge. For isothermal flow of a Newtonian fluid in the absence of leakage flow,

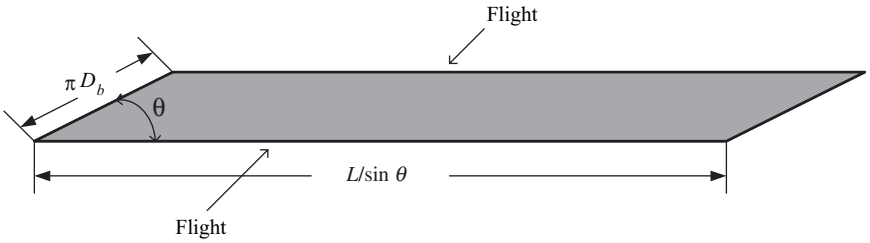

Fig. 9.3 Top view of an "unwound" screw channel indicating the oblique ends of the channel. The significance of this geometrical end-effect correction factor is of the order $\pi \sin\theta \cos\theta/(L/D)$.

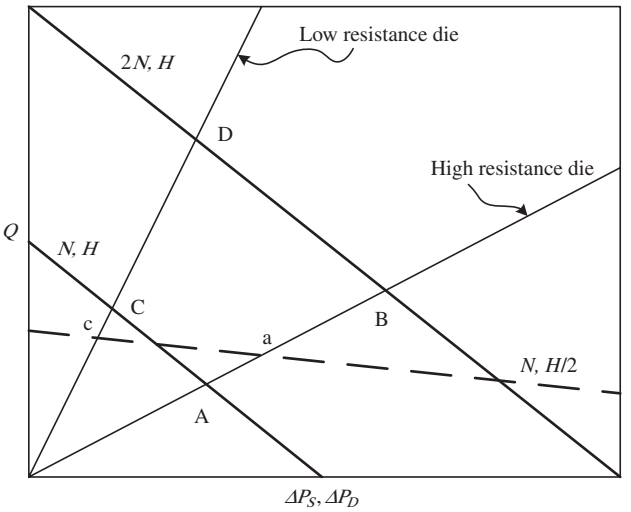

Fig. 9.4 Schematic views of screw characteristic lines for Newtonian fluids and isothermal flow. The points where the screw and die characteristic lines cross are the operating points of the extruder. The effect of the screw speed and the channel depth on the operating points is demonstrated.

the screw characteristics are straight lines with a negative slope of $-(WH^3/12\mu)(\sin\bar{\theta}/L)F_p$. Figure 9.4 illustrates the effect of two important variables on screw characteristics: frequency of screw rotation, or screw speed, as it is commonly referred to, and channel depth. Changing the former shifts the screw characteristic, whereas the latter affects both its level and slope.

A general equation for the isothermal pressure flow of an incompressible Newtonian fluid in a die (without moving parts like, e.g., wire coating dies), can be written as

$$Q_D = \frac{K}{\mu}\Delta P_D \tag{9.2-6}$$

where K is the *die constant* or ''flow conductance'' term, determined by the die geometry, and ΔP_D is the *pressure drop* over the die. For relatively simple dies, K can be calculated from basic principles (e.g., for the orifice die from Eq. 9.2-1 we find that $K = \pi R^4/8L_0$), but for more complex ones, it must be determined experimentally. Equipping an extruder with a valve is tantamount to a die with a variable K. Figure 9.4 shows two die characteristic lines, one at high die resistance and one at low die resistance. Clearly, the operating point of the former (C, D) is at higher flow rates and lower pressure drops than the latter (A, B). Note that reducing the channel depth may have a different effect with high and low resistance dies. In the case shown in Fig. 9.4, the flow rate increases with the former (operating point C shifts to c) and it drops with the latter (operating point A shifts to a). We noted in Section 6.3 that there is an optimum channel depth for maximum output or pressure, and in this schematic example, the two cases happen to fall on opposite sides of the optimum. Finally, it should be noted that, for non-Newtonian fluids and/or nonisothermal flow, the general

behavior remains the same, but the extruder and die characteristics, as shown later, will no longer be straight lines but curved ones.

By combining Eqs. 9.2-5 and 9.2-6, with $Q_S = Q_D = Q$ and $\Delta P_S = \Delta P_D = \Delta P$, the operating point of the extruder is obtained

$$Q = \frac{0.5\pi N D_b \cos\theta_b W\left(W - \delta_f\right)F_d}{1 + \left[WH^3 \sin\bar{\theta}(1 + f_L)F_p\right]/12LK} \tag{9.2-7}$$

$$\Delta P = \frac{0.5\mu\pi N D_b \cos\theta_b W\left(H - \delta_f\right)F_d}{K + \left[WH^3 \sin\bar{\theta}(1 + f_L)F_p\right]/12L} \tag{9.2-8}$$

These two equations, together with Eq. 9.2-4, form the complete model for the problem at hand.

This is the simplest model of a melt extruder–die system, but it qualitatively represents the behavior of *any* melt extruder–die combination, and it even provides good order of magnitude for them.

Example 9.1 Power and Temperature Consideration in Batch and Continuous Systems Before proceeding with the single screw modeling, we want to make a few general observations on temperature and power considerations in batch and continuous systems.

The temperature of an incompressible fluid element in a deforming medium is governed by the equation of thermal energy, Eq. 2.9-14. This excluding the reversible compression term, and in terms of specific heat, is

$$\rho C_v \frac{DT}{Dt} = -(\boldsymbol{\nabla} \cdot \mathbf{q}) + (-\boldsymbol{\tau} : \boldsymbol{\nabla}\mathbf{v}) \tag{E9.1-1}$$

which states that the change of the temperature of a fluid element in a flowing system is the sum of the heat gain (loss) by conduction and the rate of viscous dissipation in the element. Since viscosities of polymeric are high and thermal conductivities are low, efficient heat transfer must be secured to control the system at a desired temperature. The integral of the second over the volume of the system gives the total rate of conversion of mechanical energy into heat, E_v

$$E_v = \int_V (-\boldsymbol{\tau} : \boldsymbol{\nabla}\mathbf{v})\, dV \tag{E9.1-2}$$

In order to evaluate E_v we need to know the velocity and temperature fields as well as the rheology of the fluid.

For a batch system the macroscopic energy balance,[2] in the absence of kinetic and potential energy changes, reduces to

$$\frac{du}{dt} = \rho C_V M \frac{dT}{dt} = q_h + P_w \tag{E9.1-3}$$

2. The macroscopic energy balance is obtained by integrating Eq. 2.9-10.

where u is the internal energy, M is the mass in the system, q_h is the total heat added (removed) to the system, and P_w is the total power (rate of work) input. Note that for incompressible fluids $C_V = C_P$. Thus, all the input power is dissipated into heat and if isothermal conditions are desired, all the power input must be removed by conduction.

In a steady, continuous system, the macroscopic energy balance in terms of enthalpy $\hat{h}$ (per unit mass) reduces to

$$\Delta\hat{h} = \hat{q}_h + \hat{P}_w \tag{E9.1-4}$$

where $\hat{q}_h = q_h/G$ and $\hat{P}_w = P_w/G$, G being the mass flow rate. Now, the enthalpy can be expressed in terms of temperature and pressure

$$\Delta\hat{h} = \int_{T_1}^{T} C_P\, dT + \frac{\Delta P}{\rho} \tag{E9.1-5}$$

Thus, from Eqs. E9.1-4 and E9.1-5 we obtain

$$\Delta T = \frac{1}{C_P}\left(\hat{q}_h + \hat{P}_w - \frac{\Delta P}{\rho}\right) \tag{E9.1-6}$$

The macroscopic mechanical energy balance[3] reduces to

$$\hat{P}_w = \hat{E}_v + \frac{\Delta P}{\rho} \tag{E9.1-7}$$

or

$$P_w = E_v + (\Delta P)Q \tag{E9.1-8}$$

where Q is the volumetric flow rate. Thus, the total power input is partly used to increase the pressure and the rest dissipated into heat (Eq. E9.1-2). In other words, the rate of energy dissipated into heat in a continuous processor is given by the total shaft power input less the product of the volumetric flow rate with the pressure rise. By substituting Eq. E9.1-7 into Eq. E9.1-6) we obtain the temperature change in terms of heat input (loss) and viscous dissipation

$$\Delta T = \frac{1}{C_P}\left(\hat{q}_h + \hat{E}_v\right) \tag{E9.1-9}$$

Next we calculate the power input of a screw extruder. Equation E9.1-8 indicates that for calculating the total power we need to know the viscous energy dissipation and the pressure rise. To calculate the former according to Eq. E9.1-2, we need the complete velocity and temperature fields inside the machine. However, it is easier to calculate the total power input by multiplying the shear stress at any point on the barrel surface with the barrel velocity and integrating over the surface of the barrel. This will be equivalent to the total shaft power input. In tensor form, accounting for the direction of the shear stress and velocity, this is given by

$$P_w = \int_S (-[\mathbf{n}\cdot\boldsymbol{\tau}]\cdot\mathbf{v})\, dS \tag{9.2-9}$$

3. The macroscopic mechanical energy balance is obtained by integrating Eq. 2.9-11.

where S is the surface of the barrel, $\mathbf{n}$ is the outward normal unit vector, $\boldsymbol{\tau}$ is the stress tensor at the barrel surface, and $\mathbf{v}$ is the barrel velocity. Equation 9.2-9 for the simple model discussed previously reduces to

$$P_w = -\left[\tau_{yz}(H)V_{bz} + \tau_{yx}(H)V_{bx}\right]WZ \tag{9.2-10}$$

where Z is the total ''unwound'' channel length. The shear stress component $\tau_{yz}(H)$ is obtained from Eq. E2.5-20 by replacing V_0 by V_{bz} and q_p/q_d with $Q_p/Q_d = Q/Q_d - 1$, whereas, the $\tau_{yx}(H)$ is obtained by replacing V_0 by V_{bx} and setting $Q = 0$, since neglecting leakage over the flight, there is no net flow in the cross-channel direction.[4] Substituting these into Eq. 9.2-10 results in

$$P_w = \mu\frac{\pi^2 N^2 D_b^2 WL}{\sin\bar{\theta}H}\left(4 - 3\,\cos^2\theta_b\frac{Q}{Q_d}\right) \tag{9.2-11}$$

The total power input is at minimum under open discharge conditions ($Q = Q_d$) and is at maximum under closed discharge conditions ($Q = 0$). However, in addition to the power consumption in the channel, we must account for the power consumption in the flights,[5] which is by no means negligible (1a).

The rate of power input dissipated into heat can be obtained from Eq. 9.2-11 by subtracting the term $Q\Delta P$, which is the power input for pressurization (Eq. E9.1-8), to give

$$E_v = \mu\frac{\pi^2 N^2 D_b^2 WL}{\sin\bar{\theta}H}\left[4 - 6\cos^2\theta_b\frac{Q}{Q_d} + 3\cos^2\theta_b\left(\frac{Q}{Q_d}\right)^2\right] \tag{9.2-12}$$

This expression can also be obtained by integrating the term $0.5\mu\,(\dot{\boldsymbol{\gamma}} : \dot{\boldsymbol{\gamma}})$ over the volume of the channel (Eq. E9.1-2).

Calculating the adiabatic temperature rise can make an approximate test of the validity of the isothermal assumption is obtained from Eq. E9.1-9

$$\Delta T = \frac{1}{C_p}\frac{E_v}{\rho Q} \tag{9.2-13}$$

If ΔT is significant, we reject the isothermal assumption, but if it is small, local temperature effects may still be important.[6]

Without too much difficulty, we can extend the model to any screw design consisting of constant depth channels, and moderate tapers by using the taper correction factors of Eq. 6.4-4 separately for each section, and adding up the pressure drops (rises) according to Eq. 9.2.2. Thus, for a tapered channel, the drag and pressure flow terms are multiplied by the expressions $2/(1 + \zeta_0)$ and $2/\zeta_0(1 + \zeta_0)$, respectively, where $\zeta_0 = H_0/H_1$, with H_0

4. Note that, for calculating power, we neglect the effect of the leakage flow on the value of $\tau_{yx}(H)$, but we account for leakage flow for flow rate and pressure generation. This is not consistent, but acceptable in mathematical modeling of an engineering system because the former (depending in flight clearance) is less critical than the latter.

5. If we do this, we must make a minor correction to account for the loss of the barrel surface over the flight.

6. In Section 12.1 we show that in capillary flow average temperature rise may be very misleading, because even low values may hide large temperature rises at the capillary wall. The same may hold in this case, although the cross-channel circulatory flow brings about mixing of the melt-reducing cross-channel nonuniformities.

being the channel depth at the inlet and H_1 at the outlet, and H in Eq. 9.2-5 being replaced by H_0.

Example 9.2 The Design of a HDPE Pelletizing Extruder Design an 18,000-lb/hr pelletizing extruder for high-density polyethylene (HDPE) melt at 450°F to generate 2500 psi head pressure. Assume a constant channel depth extruder with an axial length of 60 in. The melt density is 54 lb/ft^3, the viscosity is 0.15 lb$_f$s/in^2, and the specific heat is 0.717 Btu/lb°F.

Solution This is an open-ended problem, which has many possible solutions. We need to find the diameter of the barrel, the channel depth, and the screw speed needed to generate the head pressure. We shall assume a square pitched screw, and use British units (in, s, Btu, lb$_f$).

First we compute the volumetric flow rate

$$Q = \frac{18{,}000(\text{lb/h}) \times 1728(\text{in}^3/\text{ft}^3)}{3600(\text{s/h}) \times 54(\text{lb/ft}^3)} = 160\left(\text{in}^3/\text{s}\right)$$

Next we turn to Eq. 9.2-5 and derive the optimum channel depth for the maximum pressure rise at fixed screw speed and barrel diameter. We rewrite Eq 9.2-5, neglecting the effect of the flight clearance and the shape factors, as follows

$$\frac{\Delta P \sin\bar{\theta}}{L} = \frac{6\mu\pi N D_b \cos\theta_b}{H^2} - Q\frac{12\mu}{WH^3}$$

Next, we take the derivative of this equation with respect to channel depth to obtain the optimum channel depth, H_{op}

$$\frac{d\left(\Delta P \sin\bar{\theta}/L\right)}{dH} = 6\mu\left(\frac{-2\pi N D_b \cos\theta_b}{H^3} + \frac{6Q}{WH^4}\right) = 0$$

to give

$$H_{\text{op}} = \frac{3Q}{\pi N W D_b \cos\theta_b}$$

It is easy to show that, with the optimum channel depth, $Q_d = 3\,Q/2$ and $Q_p = Q/2$.

We now take the drag and pressure flow terms in Eq. 9.2-5 and substitute the relevant numerical values. We assume a square pitched screw, neglecting the difference between mean and barrel surface helix angle, and neglecting shape factors and flight clearance. We further assume that flight width is 10% of the barrel diameter. We can make these simplifying assumptions because, at this point, we only wish to select the barrel diameter and the screw speed. The channel width can be expressed in terms of the screw diameter as follows:

$$W = D_b \cos\bar{\theta} - e = 0.953D_b - 0.1D_b = 0.853D_b$$

where we neglected the difference between the helix angle at the barrel surface and at the midchannel plane. Now, using Eq. 9.2-5, we can write for the drag flow term

$$Q_d = 1.5Q = 0.5\pi N D_b (0.853D_b)\cos\theta_b H_{\text{op}} = 1.28D_b^2 N H_{\text{op}}$$

and substitute 160 in^3/s for the net flow rate to get

$$D_b^2(\text{in}^2)H_{\text{op}}(\text{in})N(\text{s}^{-1}) = 187.97(\text{in}^3/\text{s})$$

Next, we write the pressure flow term

$$Q_p(\text{in}^3/\text{s}) = 0.5Q = \frac{(0.853D_b)H_{\text{op}}^3}{12(0.15)}\frac{(2500)(0.302)}{(60)} = 5.963\ H_{\text{op}}^3 D_b$$

and the power input per unit volume is obtained from Eq. 9.2-12 divided by the channel volume $WLH_{\text{op}}/\sin\bar{\theta}$, which within the approximation we made, gives

$$e_v(\text{lb}_\text{f}\ \text{in}/\text{in}^3\ \text{s}) = 2.38\left(\frac{ND_b}{H_{\text{op}}}\right)^2$$

Note that the mean shear rate in the channel is given by

$$\bar{\dot{\gamma}} = \frac{\pi N D_b}{H_{\text{op}}}$$

The channel volume divided by the net volumetric flow rate gives the mean residence time

$$\bar{t}(s) = \frac{(0.853D_b)H_{\text{op}}(60/\sin\bar{\theta})}{160} = 1.0578D_bH_{\text{op}}$$

Finally, the mean temperature rise is given by

$$\Delta\bar{T}(^\circ\text{F}) = 4.7795 \times 10^{-3} e_v(\text{lb}_\text{f}\ \text{in}/\text{in}^3\ \text{s})\bar{t}(\text{s})$$

From the preceding equations, we can now select a barrel diameter, calculate the optimum channel depth, then the screw speed, the mean shear rate, and the power per unit volume. In the following table, the results are shown with barrel diameters from 8 in to 16 in.

D_b (in)	H_{op} (in)	$N(\text{s}^{-1})$	N (rpm)	$\bar{\dot{\gamma}}(\text{s}^{-1})$	e_v ($\text{lb}_\text{f}\text{in}/\text{in}^3\text{s}$)	$\bar{t}$ (s)	$\Delta\bar{T}$ (°F)
8	1.188	2.472	148	52.2	659	10.0	31.7
10	1.103	1.704	102	48.5	568	11.7	31.7
12	1.038	1.258	75	45.7	503	13.2	31.7
14	0.986	0.973	58	43.4	454	14.6	31.7
15	0.964	0.867	52	42.4	434	15.3	31.7
16	0.943	0.779	47	41.5	415	16.0	31.7

At first sight, based on the results we have, any of these extruders would be able to do the job. The 8-in extruder would need 7.5 turns to build up the required pressure, whereas the 16-in one will only need 3.75 turns. We note that both mean shear rate and specific power input per

unit volume drop significantly with increasing diameter, but the mean residence time increases, resulting in a constant mean temperature of about 31°F. This is quite a significant temperature rise, particularly if we take into account that the temperature over the channel height is not uniform, and may exhibit a significant local maximum that may be as high as twice the mean value. In actual operation, the barrel at this section may be cooled, somewhat reducing the mean temperature rise, but this does not eliminate the local maxima. In fact, overcooling, because of the interplay between convection and creation of a cool viscous melt layer near the barrel surface, may increase rather than decrease it. This is a rather important point, because temperature nonuniformities in a pelletizing extruder will yield unequal pellet sizes. Therefore, a reasonable first choice would be to select an extruder of 14 or 15 in diameters, where the shear rates and specific power inputs are low and the residence time reasonable. Subsequently, one would go to a more detailed solution without the simplifying assumptions introduced here, using a nonisothermal and non-Newtonian computer package.

Non-Newtonian and Nonisothermal Models

Distributed Parameter Models Both non-Newtonian and shear-thinning properties of polymeric melts in particular, as well as the nonisothermal nature of the flow, significantly affect the melt extrusion process. Moreover, the non-Newtonian and nonisothermal effects interact and reinforce each other. We analyzed the non-Newtonian effect in the simple case of unidirectional parallel plate flow in Example 3.6 where Fig.E 3.6c plots flow rate versus the pressure gradient, illustrating the effect of the shear-dependent viscosity on flow rate using a Power Law model fluid. These curves are equivalent to screw characteristic curves with the cross-channel flow neglected. The Newtonian straight lines are replaced with *S*-shaped curves.

Let us next consider the simple *isothermal* drag flow ($dP/dz = 0$) of a shear-thinning fluid in the screw channel. The cross-channel flow, induced by the cross-channel component of the barrel surface velocity, affects the down-channel velocity profile and vice versa. In other words, the two velocity profiles become coupled. This is evident by looking at the components of the equation of motion. Making the common simplifying assumptions, the equation of motion in this case reduces to

$$\frac{\partial \tau_{yz}}{\partial y} = 0 \tag{9.2-14}$$

and

$$\frac{\partial \tau_{yx}}{\partial y} = -\frac{\partial P}{\partial x} \tag{9.2-15}$$

Expressing the stress components in terms of the velocity gradients, we obtain the following two *coupled* differential equations

$$\frac{dv_z}{dy} = -\frac{C_1}{m}\left[\left(\frac{dv_x}{dy}\right)^2 + \left(\frac{dv_z}{dy}\right)^2\right]^{(1-n)/2} \tag{9.2-16}$$

and

$$\frac{dv_x}{dy} = \frac{1}{m}\left[\left(\frac{dv_x}{dy}\right)^2 + \left(\frac{dv_z}{dy}\right)^2\right]^{(1-n)/2}\left(\frac{dP}{dx}\right)(y - y_e) \tag{9.2-17}$$

where C_1 and y_e are integration constants to be evaluated from the boundary conditions $v_x(0) = V_z(0) = 0, v_x(H) = -V_b \sin\theta$, and $v_z(H) = V_b \cos\theta$. The constant C_1 is the shear stress component in the down-channel direction, and y_e is the channel height where the cross-channel velocity profile exhibits an extremum point. Clearly, the down-channel velocity profile $v_z(y)$, in spite of the constant shear-stress component value or absence of down-channel pressure gradient, is no longer linear. In physical terms, the cross-channel shear-rate distribution affects the non-Newtonian viscosity, which varies with y, hence, in the down-channel direction, the liquid responds as a rheologically nonhomogeneous liquid. Consequently, the deviation from linearity becomes a function of the helix angle; as the helix angle approaches a value of zero, the parallel-plate model is regained.

Next, we explore some nonisothermal effects on of a shear-thinning temperature-dependent fluid in parallel plate flow and screw channels. The following example explores simple temperature dependent drag flow.

Example 9.3 Nonisothermal Drag Flow of a Power Law Model Fluid Insight into the effect of nonisothermal conditions, on the velocity profile and drag flow rate, can be obtained by analyzing a relatively simple case of parallel-plate nonisothermal drag flow with the two plates at different temperatures. The nonisothermicity originates from viscous dissipation and nonuniform plate temperatures. In this example we focus on the latter.

We assume an exponential temperature dependence of the parameter m

$$m = m_0 e^{-a(T-T_0)} \tag{E9.3-1}$$

If $a = 0$, the non-Newtonian viscosity is temperature independent and the equations of motion and energy can be solved independently from each other; if, however, $a \neq 0$, they are coupled. Next, we assume that viscous dissipation is negligible $\mathrm{Br} \to 0$, and that the moving plate at velocity V_0 is T_1 and the lower stationary plate is T_0. The equations of motion and energy reduce to

$$\frac{d}{d\xi}\left[\left(\frac{du_z}{d\xi}\right)^n e^{b\Theta}\right] = 0 \tag{E9.3-2}$$

and

$$\frac{d^2\Theta}{d\xi^2} = 0 \tag{E9.3-3}$$

where $\Theta = (T - T_0)/(T_1 - T_0)$ and $b = -a(T_1 - T_0)$. The boundary conditions are $\Theta(0) = u_z(0) = 0$ and $\Theta(1) = u_z(1) = 1$. Solving Eqs. E9.3-2 and E9.3-3 yields the velocity and temperature profiles

$$u_z = \frac{1 - e^{-b'\xi}}{1 - e^{-b'}} \tag{E9.3-4}$$

and

$$\Theta = \xi \tag{E9.3-5}$$

where

$$b' = \frac{-a(T_1 - T_0)}{n} \tag{E9.3-6}$$

Note that the temperature profile is linear, because we neglected viscous dissipation, but the velocity profile is nonlinear because the temperature dependence of m. Integrating the velocity profile yields the flow rate per unit width

$$q = \frac{HV_0}{2} U_2 \tag{E9.3-7}$$

where

$$U_2 = 2\frac{1 - b' - e^{-b'}}{b'(e^{-b'} - 1)} \tag{E9.3-8}$$

The factor $U_2 < 1$ for $b' < 0$ ($T_1 > T_0$); that is, flow rate drops if the temperature of the dragging surface is higher than the stationary wall, and vice versa. Since the shear stress is constant across the gap, in the former case, and the viscosity drops as we approach the moving plate, and, therefore, the shear rate must increase (so that the product is constant), and the velocity profile becomes convex. This effect, as we will see in the melting model discussed later, strongly affects the melting rate.

Now let us turn to the case of *nonisothermal* flow of a shear-thinning temperature-dependent polymer melts in combined pressure and drag flow. Colwell and Nicholls (3), explored nonisothermal effects of flow in the screw channels, neglecting the effect of cross-channel flow in parallel plate geometry. For a Power Law model fluid, their analysis parallels the nonisothermal effects considered in the preceding example, with pure drag flow replaced by combined pressure and drag flow. Figure 9.5 summarizes some of their results, plotting the ''screw'' characteristic (curve *A*). We note the typical S-shaped curve, but at nonisothermal conditions, the mean extrudate temperature varies slightly along the characteristic curve. There is interaction among heat transfer through the constant temperature walls, viscous dissipation, and the velocity profile, coupled through the temperature dependent viscosity. Colwell and Nichols (3) also calculated similar curves under adiabatic conditions, shown in Fig. 9.5 for high and low inlet temperatures. It is worth noting that the adiabatic screw characteristic curves exhibit maximum attainable pressures and a region of double values of flow rate for a given pressure rise.

Griffith (4), Zamodits and Pearson (5) and Yates (6) were the first to account for cross-channel flow of a temperature-dependent shear-thinning fluid, but they all assumed the flow to be two-dimensional and fully developed, both hydrodynamically and thermally $[v_x(y), v_z(y), T(y)]$, by numerical solution using the finite difference method. Figure 9.6 shows some of Griffith's results of isothermal Power Law model fluids in shallow channels, exhibiting the typical S-shaped curves, with increasing deviation from Newtonian behavior ($n < 1$), as well as a downward shift of the curves as a result of the cross-channel–down-channel coupling effect. This downward shift diminishes with diminishing helix angle. Griffith, who tested these results experimentally with a 1%

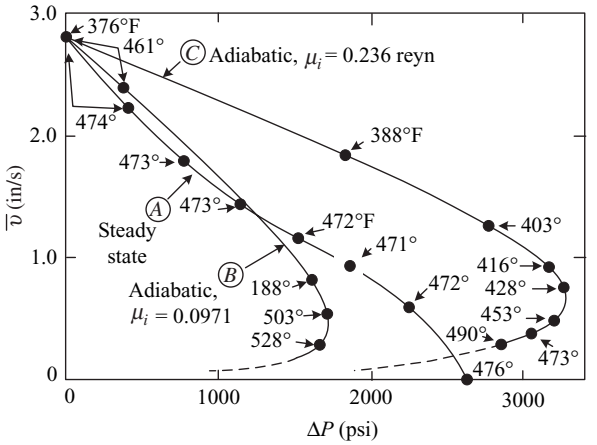

Fig. 9.5 Computed average velocities (proportional to volumetric flow rate) as a function of pressure drop. Length, 50 in; V_{bz} 5.66 in/s. Curve *A*, steady state; curve *B*, adiabatic high inlet temperature; curve *C*, adiabatic low inlet temperature. Note the double-valued flow rates at a given pressure rise in the adiabatic operation and the maximum pressure rise at finite flow-rate values. [Reprinted by permission from R. E. Colwell and K. R. Nicholls, "The Screw Extroder," *Ind. Eng. Chem.*, **51**, 841–843 (1959).]

solution of a carboxyvinyl polymer in water extruded in a 2-in-diameter extruder, reported good agreement with theoretical predictions. These solutions, however, neglect the rather significant effect of the down-channel convection on temperature. This was accounted for in the work of Yates (6), and later that of Fenner (7,8) and Elbirli and Lindt (9).

With the great strides in computational fluid mechanics made over the past decades, the current trend is toward applying sophisticated *finite element* methods. These include both two- and three-dimensional (10–15) methods, which in principle allow the computation of two- or three-dimensional velocity and temperature fields with a variety of boundary

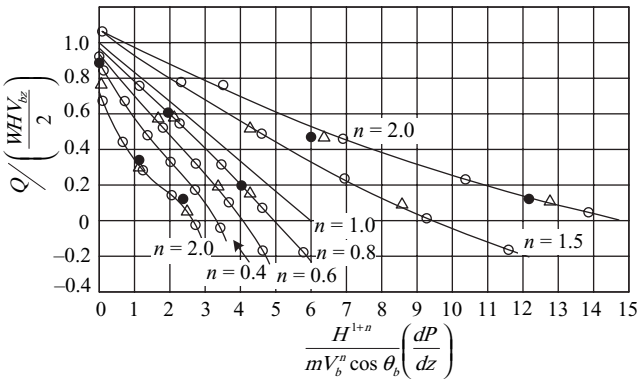

Fig. 9.6 Computed curves of dimensionless flow rate versus dimensionless pressure gradient for isothermal flow of a power law model fluid in shallow screw channels with the power law exponent n as a parameter, for helix angles θ_f as follows: O, 30°; Δ, 20°; •, 10°; solid curves are for a helix angle 30°. Note that for $n < 1$, the reduced flow rate is less than 1, with the deviation diminishing with decreasing of the helix angle. [Reprinted with permission from R. M. Griffith, "Fully Developed Flow in Screw Extruders," *Ind. Eng. Chem. Fundam.*, **1**, 180–187 (1962).]

conditions, while accounting for convection in both directions. Yet, convection terms, in particular the circulatory flow in the cross-channel direction, may give rise to numerical-stability problems. However, Syrjälä (16) recently computed very efficiently the three-dimensional fluid flow and heat transfer of a shear-thinning temperature-dependent fluid in a screw channel, accounting for convection in both the recirculation cross-channel flow, as well as the down-channel flow. He showed that the circulatory flow significantly alters the temperature, viscosity, and velocity profiles, as compared to two-dimensional solutions neglecting the cross-channel convection. Specifically, the temperature variation over the channel height is reduced by the recirculating flow, and the down-channel pressure profile deviates significantly from the two-dimensional computation. In real extruders, however, in addition to the recirculating flow, there is a series of additional factors and conditions that make accurate computation very difficult. For example, the leakage flow over the flight clearance, which both consumes significant power and may significantly alter the flow and temperature patterns in the screw channel; the nonprecise boundary conditions on the barrel surface; the root of the screw and the flights; the possibility of slip on the metal surfaces; and entrance and exit effects. Moreover, the polymeric material is frequently not a homogeneous fluid, but rather a filled or multicomponent system, such as a blend and alloy, or a reactive system with less well-defined rheological properties.

Still, sophisticated, exact, numerical, non-Newtonian and nonisothermal models are essential in order to reach the goal of accurately predicting final *product* properties from the total thermomechanical and deformation history of each fluid element passing through the extruder. A great deal more research remains to be done in order to accomplish this goal.

Lumped-parameter Models For *engineering design* of extruders, much simpler, lumped-parameter models may generally suffice. The main goal of the engineering design is to predict the pressure and mean melt temperature profiles along the extruder for a given screw geometry and output rate as a function of the operational parameters: screw speed, pressure at the die (or die characteristic), and barrel temperature profiles. In the models first proposed by Klein and Tadmor (17), the screw channel is divided into short axial segments, as shown in Fig. 9.7, where the inlet temperature and pressure are known from the calculation in the previous upstream segment. Within each segment, the temperature is

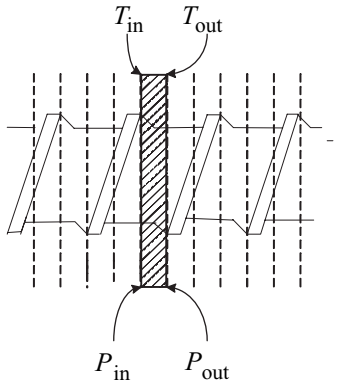

Fig. 9.7 The shaded area shows an axial slice of the screw with inlet melt temperature and pressure T_{in} and P_{in} and outlet temperature and pressure T_{out}, P_{out}.

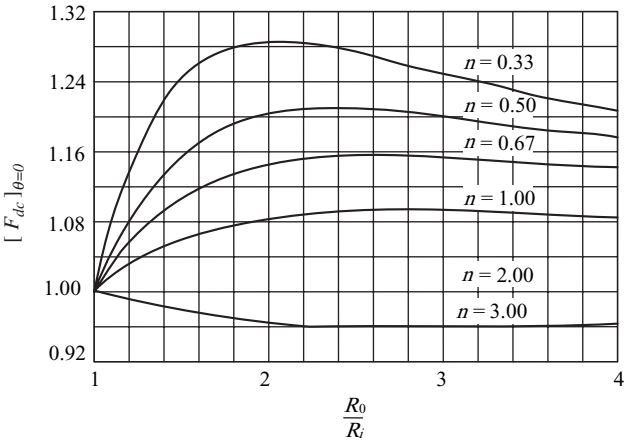

Fig. 9.8 Curvature correction factor for drag flow for a Power Law model fluid. $[F_{dc}]_{\theta=0}$ denotes the ratio of drag flow between parallel plates to drag (Couette) flow between concentric cylinders at equal gaps and moving surface velocities. The subscript $\theta = 0$ indicates that in screw extrusion this correction factor is rigorously valid only in the limit of a zero helix angle. [Reprinted by permission from Z. Tadmor and I. Klein, *Engineering Principles of Plasticating Extrusion*, Van Nostrand Reinhold, New York, 1970.]

assumed to be uniform and is equal to the mean temperature based on inlet and outlet temperatures: $(T_{\text{in}} + T_{\text{out}})/2$. Moreover, within each segment mean barrel and screw[7] temperatures are assumed, as well as constant channel depth, which is the mean value between entrance and exit. Using isothermal non-Newtonian models, the pressure change across the segment is computed applying rheological properties at the mean temperature within the segment. Then, via an enthalpy balance including heat fluxes from the barrel, and screw and viscous dissipation, we calculate the temperature change in the segment. From these, T_{out}, P_{out} are calculated, and the shaft power input and torque in the segment. The computation is, of course, iterative within each segment (because the mean temperature and pressure depend on the exit values) as well as over the whole extruder in order to converge on the particular output at which the pressure rise in the extruder equals the pressure drop over the die.

The details of the fluid mechanical computations within each segment can vary in complexity. One rather useful approach was found to be the previously mentioned general modeling approach of ''correcting'' the separately computed drag and pressure flow terms for Power Law model fluids for shape (18), curvature (Figure 9.8) (19), and viscosity ratio at barrel and melt temperature[8] (1d), and so on. The pressure-flow term is calculated using a Power Law model fluid. Of course, for a non-Newtonian fluid, drag and pressure flow cannot be superimposed as in the case of Newtonian fluids, but by introducing a ''superposition correction factor'' (1d), this error can be eliminated. These individual correction factors, in addition to providing some quantitative insight into the magnitude of the effects considered, were successfully applied to calculations by an appropriate

7. For ''neutral'' screws, that is, screws that are neither heated nor cooled through the shaft, it was found that the screw temperature at any given axial location equals that of the melt (1e).

8. The barrel temperature affects not only heat conduction into the barrel but it may strongly affect the drag capacity of the barrel; for example, if the barrel surface temperature is higher than the melt temperature, drag is reduced.

modeling scheme (1d,17). The analytical aspects of the foregoing procedure are given in great detail by Tadmor and Klein (1), and the computational aspects leading to computer program packages are given by Klein and Tadmor[9](17).

The lumped-parameter model approach becomes particularly useful when dealing with the plasticating extrusion process discussed in the next subsection, where, in addition to melt flow, we are faced with the elementary steps of solids handling and melting.

Extensive Mixing and Residence Time Distribution in Screw Extruders

The velocity profiles for an isothermal Newtonian fluid in the screw channel were derived in Section 6.3. We concluded that the fluid particles circulate in the cross-channel direction while flowing down the channel. Thus, the flow path is a ''helix within a helix.'' This, as we will see below, leads to good laminar mixing and to narrow residence time distribution (RTD). Having narrow RTD which approaches plug-flow conditions, is a useful characteristic in a polymer processing machine to avoid the risk of thermal degradation of the long-term ''tail'' of the RTD. On the other hand, it also implies that inlet time fluctuations of composition should be *avoided* because the extruder is ineffective in ''washing'' out these fluctuations.

We now derive the RTD function $f(t)\,dt$ and the strain distribution functions $f(\gamma)\,d\gamma$ for isothermal Newtonian fluids in shallow screw channels.

The cross- and down-channel velocity profiles are (see Section 6.3):

$$u_x = \xi(2 - 3\xi) \tag{9.2-18}$$

and

$$u_z = \xi + 3\xi(1 - \xi)\frac{Q_p}{Q_d} \tag{9.2-19}$$

Thus, the operating conditions affect the down-channel velocity profile, but not the cross-channel velocity profile. At closed discharge conditions $(Q_p/Q_d = -1)$, both the down-channel and cross-channel velocities vanish at $\xi = 2/3$, implying that the whole plane at this location is stagnant.

The Residence Time Distribution Function A fluid particle at height $\xi > 2/3$ will approach the ''pushing flight'' turnaround and move toward the trailing flight at height ξ_c. The relation between the two heights can be obtained by the following mass balance (neglecting leakage flow over the flights):

$$\int_0^{\xi_c} u_x\,d\xi = -\int_{\xi}^{1} u_x\,d\xi \tag{9.2-20}$$

Substituting Eq. 9.2-18 into Eq. 9.2-20 yields

$$\xi_c^2 - \xi_c^3 = \xi^2 - \xi^3 \tag{9.2-21}$$

9. Note that in Reference 17, Table 1, which gives the coefficients for the regression analysis of the superposition correction error, there is a misprint: $C_{82} = -0.02029$ and not -0.2029 as listed.

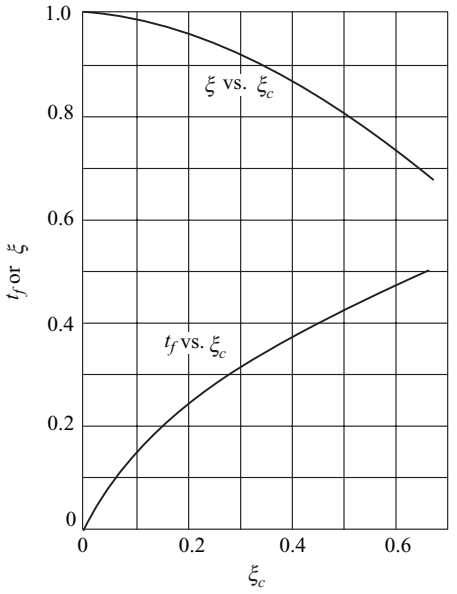

Fig. 9.9 Fluid particle position in the upper part of the channel, ξ, versus its position in the lower part of the channel, ξ_c, and the fraction of time t_f versus position ξ_c.

where $0 \leq \xi_c \leq \frac{2}{3}$ and $\frac{2}{3} \leq \xi \geq 1$.

Equation 9.2-21 can be solved to give

$$\xi = \frac{1}{2}\left(1 - \xi_c + \sqrt{1 + 2\xi_c - 3\xi_c^2}\right) \qquad 0 \leq \xi_c \leq \frac{2}{3} \tag{9.2-22}$$

and

$$\xi_c = \frac{1}{2}\left(1 - \xi + \sqrt{1 + 2\xi - 3\xi^2}\right) \qquad \frac{2}{3} \leq \xi \leq 1 \tag{9.2-23}$$

Figure 9.9 plots the relationship between ξ and ξ_c. In this analysis we disregarded the complex flow fields in the neighborhood of the flights, which are restricted to regions of the order of channel height distance from the flight. The exact flow fields can be obtained by standard numerical methods, which confirm the flow patterns previously described, though they indicate that in the lower corners small stagnant fluid regions appear where reverse circulation takes place.[10]

The residence time of a fluid particle at a given height in one cycle is obtained by dividing the channel width with the local cross-channel velocity given in Eq. 9.2-18. The residence time at ξ is different, of course, from that at ξ_c. It is easy to show that the

10. These solutions [e.g., O. R. Burggaf, "Analytical and Numerical Studies of the Structure of Steady Separated Flows," *J. Fluid Mech.*, **24**, 113–151 (1966)] were done with a rectangular channel. Real screws have rounded corners that most likely eliminate these stagnant pockets. However, we note that residence time and the strain distribution function are more sensitive to fine local flow structures then design equations relating pressure gradients and flow rates. Therefore, care should be exercised in using equations based on simple flow models.

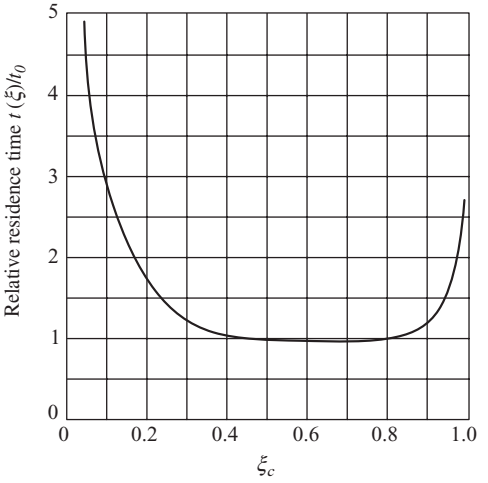

Fig. 9.10 The normalized residence time as a function of ξ.

fraction of time the fluid particle spends in the upper portion of the channel, $t_f(\xi)$, is given by

$$t_f(\xi) = \frac{1}{1 + \dfrac{|u_x(\xi)|}{|u_x(\xi_c)|}} = \frac{1}{1 - \dfrac{\xi(2-3\xi)}{\xi_c(2-3\xi_c)}} \tag{9.2-24}$$

Figure 9.10 plots $t_f\xi$ as a function of position. Results indicate that the further away the fluid particle is from $\xi = 2/3$, the shorter is the fraction of time it spends in the upper portion of the channel. The fluid particle, while alternating between layers ξ and ξ_c, also moves in the down-channel direction, as dictated by Eq. 9.2-19. The residence time of this fluid particle in an extruder of axial length l is

$$t = \frac{l}{V_b \bar{u}_l(\xi)} \tag{9.2-25}$$

where V_b is the barrel velocity relative to the screw and $\bar{u}_l(\xi)$ is the average velocity of the fluid particle in the axial direction given by

$$\bar{u}_l(\xi) = u_l(\xi)t_f(\xi) + u_l(\xi_c)\big[1 - t_f(\xi)\big] \tag{9.2-26}$$

The velocity profile in the axial direction is obtained from Eqs. 9.2-18 and 9.2-19 (see Section 6.3)

$$u_l(\xi) = 3\xi(1-\xi)\left(1 + \frac{Q_p}{Q_d}\right)\sin\theta\cos\theta \tag{9.2-27}$$

Substituting Eq. 9.2-26 and 9.2-27 into Eq. 9.2-25, together with Eqs. 9.2-22 and 9.2-23, gives the residence time of a fluid particle circulating between locations ξ and ξ_c

$$t(\xi) = \left[\frac{l}{3V_b\big(1 + Q_p/Q_d\big)\sin\theta\cos\theta}\right]\frac{3\xi - 1 + \sqrt{1 + 2\xi - 3\xi^2}}{\xi\left[1 - \xi + \sqrt{1 + 2\xi - 3\xi^2}\right]} \tag{9.2-28}$$

for $2/3 \leq \xi \leq 1$. The minimum residence time is at $\xi = 2/3$

$$t_{\min} = \frac{3l}{2V_b\left(1 + Q_p/Q_d\right)\sin\theta\cos\theta} = \frac{3z}{2V_{bz}\left(1 + Q_p/Q_d\right)} \tag{9.2-29}$$

where z is the helical distance and V_{bz} the down-channel barrel-velocity component. Figure 9.10 plots the normalize residence time $t/t_{\min}$ as a function of ξ.

Figure 9.10 indicates that over a broad region of the channel core, the residence time is close to the minimum, but as we approach the top or bottom of the channel, the residence time increases significantly. The importance of this, however, cannot be appreciated unless we derive the *RTD* function (20), which tells what *fraction* of the exiting flow rate that stays a given time t in the channel.

The fraction of flow rate in the upper portion of the channel between ξ and $\xi+d\xi$, corresponding to residence time t and $t + dt$, is

$$\frac{dQ}{Q} = \frac{V_{bz}WH}{Q}u_z(\xi)\,d\xi = \frac{V_{bz}WH}{Q}\left[\xi + 3\xi(1-\xi)\frac{Q_p}{Q_d}\right]d\xi \tag{9.2-30}$$

and that in the corresponding lower portion of the channel is

$$\frac{dQ_c}{Q} = \frac{V_{bz}WH}{Q}u_z(\xi_c)|d\xi_c| = \frac{V_{bz}WH}{Q}\left[\xi_c + 3\xi_c(1-\xi_c)\frac{Q_p}{Q_d}\right]|d\xi_c| \tag{9.2-31}$$

The total fraction of flow rate between time t and $t + dt$ is the sum of Eqs. 9.2-30 and 9.2-31, which is also the definition of the RTD function $f(t)\ dt$

$$f(t)dt = \frac{dQ + dQ_c}{Q} \tag{9.2-32}$$

By substituting Eqs. 9.2-30 and 9.2-31 into Eq. 9.2-32 and further deriving a relationship between $d\xi$ and $d\xi_c$ from Eq. 9.2-23, we get

$$d\xi_c = \frac{1 - 3\xi - \sqrt{1 + 2\xi - 3\xi^2}}{2\sqrt{1 + 2\xi - 3\xi^2}}d\xi \tag{9.2-33}$$

and noting that $|d\xi_c| = -d\xi_c$, we get

$$f(t)dt = \frac{3\xi\left[1 - \xi + \sqrt{1 + 2\xi - 3}\xi^2\right]}{\sqrt{1 + 2\xi - 3\xi^2}}d\xi \tag{9.2-34}$$

Equation 9.2-28 provides a unique relation between ξ and t; thus, the RTD function $f(t)\ dt$ can be easily evaluated. We note that the RTD functions depend on only one dimensionless group $l/3V_b\left(1 + Q_p/Q_d\right)\sin\theta\cos\theta$ in Eq. 9.2-28, which is a simple multiplier and does not alter the *shape* of the RTD.

The mean residence time can be evaluated from Eq. 9.2-32 and Eq. 9.2-28 to give

$$\bar{t} = \int_{t_{\min}}^{\infty} tf(t)\,dt = \frac{4}{3}t_{\min} \tag{9.2-35}$$

where $t_{\min}$ is given in Eq. 9.2-29.

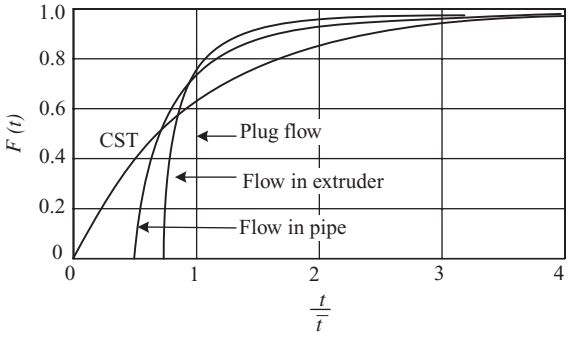

Fig. 9.11 The RTD function $F(t)$ versus reduced time $t/\bar{t}$ for flow in screw extruder compared to plug flow, isothermal flow of Newtonian fluids in pipes, and a continuously stirred tank vessel (CST).

The cumulative RTD function $F(t)$ is obtained by integrating Eq. 9.2-24 while recalling that the fraction of flow rate with a residence time less than t is located in the region is located between $\xi = 2/3$ and ξ:

$$F(t) = F(\xi) = \frac{1}{2}\left[3\xi^2 - 1 + (\xi - 1)\sqrt{1 + 2\xi - 3\xi^2}\right] \tag{9.2-36}$$

Once again $F(t)$ can be calculated from Eq. 9.2-36 in conjunction with Eq. 9.2-28. Figure 9.11 plots the RTD function $F(t)$ versus reduced time $t/\bar{t}$ and compares it to the RTD function of Newtonian laminar flow in a pipe and that in a well-stirred vessel. The RTD function in the melt extruder is quite narrow, approaching plug-type flow. Only about 5% of the flow rate stays more than twice the mean residence time in the extruder.

Wolf and White (21) verified the theoretical RTD function experimentally with radioactive tracer methods. Figure 9.12 gives some of their results, indicating excellent agreement with theory. RTD functions in extruders using non-Newtonian Power Law model fluids have also been derived (22,23).

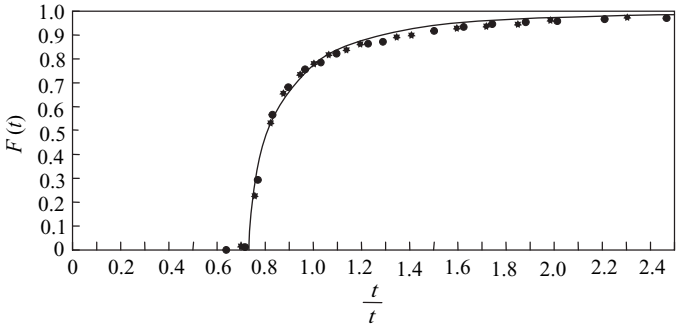

Fig. 9.12 Experimental verification of the RTD function in extruder by radioactive tracer techniques with a 44.2-mm-diameter, 24:1 *L/D* extruder, liquid polyester resin, and a radioactive manganese dioxide tracer: Asterisk, Experiment 1; •, Experiment 2; smooth curve indicates theoretical prediction. [Reprinted by permission from D. Wolf and D. H. White, "Experimental Study of the Residence Time Distribution in Plasticating Screw Extruders," *AIChE J.*, **22**, 122–131 (1976).]

The Strain Distribution Functions In Chapter 7 we established the relation between interfacial area stretching and the total strain imposed on the fluid. The strain is the product of rate of strain and time, and therefore strain is a function of location in the channel. The strain distribution function (SDF) was defined in Chapter 7 as the fraction of exiting flow rate that experienced a given strain in the extruder. Following similar lines to the derivation of the RTD functions we now derive the SDF.

The rate of strain components are obtained from Eqs. 6.3-16 and 6.3-17 (simplified for shallow channels)

$$\dot{\gamma}_{yx}(\xi) = \frac{V_{bx}}{H}\frac{du_x}{d\xi} = \frac{2V_b \sin\theta}{H}(1-3\xi) \tag{9.2-37}$$

and

$$\dot{\gamma}_{yz}(\xi) = \frac{V_{bz}}{H}\frac{du_z}{d\xi} = \frac{2V_b \cos\theta}{H}\left[1+3(1-2\xi)\frac{Q_p}{Q_d}\right] \tag{9.2-38}$$

According to our model, these are the only components of the rate of strain tensor. Thus, we can write an expression for the magnitude of the rate of strain tensor (cf. Eq. 2.7-11)

$$\begin{aligned}\dot{\gamma}(\xi) &= \left(\dot{\gamma}_{yx}^2 + \dot{\gamma}_{yz}^2\right)^{1/2} \\ &= \frac{V_b}{H}\left\{4(1-3\xi)^2\sin^2\theta + \left[1+3(1-2\xi)\frac{Q_p}{Q_d}\right]\cos^2\theta\right\}^{1/2}\end{aligned} \tag{9.2-39}$$

A corresponding expression for $\dot{\gamma}(\xi_c)$ is obtained by replacing ξ with ξ_c in Eq. 9.2-39. The direction of shear of a fluid particle differs at ξ and at ξ_c. This poses difficulties in evaluating the total strain experienced by a fluid particle circulating between these two positions, because depending on the specific position of ξ and the exact nature of the turnover at the flight, partial demixing may occur. The exact solution of the problem would require following the fluid particle in the true three-dimensional flow patterns, with the prerequisite of relating the increase of interfacial area to the invariants of the strain tensor. As a first approximation, however, we assume that total strains acquired in the upper and lower parts of the channel are additive. Thus, the total strain acquired by the fluid particle after time t is

$$\gamma(\xi) = \dot{\gamma}(\xi)t_f(\xi)t(\xi) + \dot{\gamma}(\xi_c)\left[1-t_f(\xi)\right]t(\xi) \tag{9.2-40}$$

Substituting Eqs. 9.2.24, 9.2.28, and 9.2.39 into Eq. 9.2.40 gives

$$\gamma(\xi) = \frac{l}{3H}\left(\frac{1}{1+Q_p/Q_d}\right)\left[E_1\left(\xi,\theta,Q_p/Q_d\right) + E_2\left(\xi,\theta,Q_p/Q_d\right)\right] \tag{9.2-41}$$

where

$$E_1\left(\xi,\theta,Q_p/Q_d\right) = \frac{2}{\cos\theta}\frac{t_f(\xi)\left[(1-3\xi)^2 + \dfrac{\cot^2\theta}{4}\left(1+3\dfrac{Q_p}{Q_d}-6\xi\dfrac{Q_p}{Q_d}\right)^2\right]^{1/2}}{\xi_c(1-\xi_c) + \left[t_f(\xi)\right](\xi-\xi_c)(1-\xi-\xi_c)} \tag{9.2-42}$$

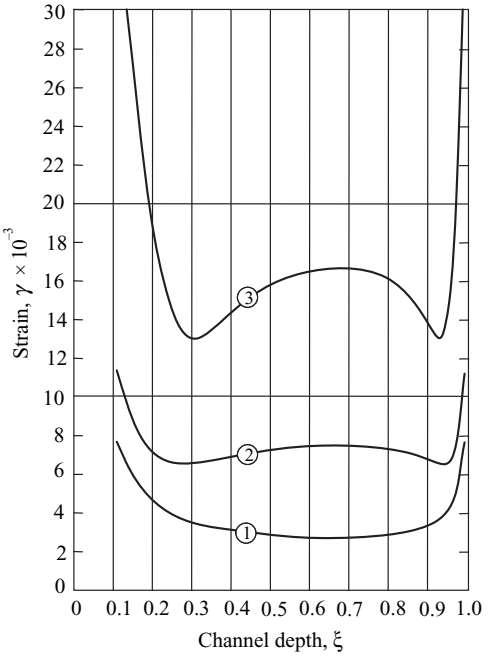

Fig. 9.13 Total strain as a function of position ξ in a screw channel. Calculations are based on a total axial length of 100 in, channel depth of 0.2 in, and 20° helix angle. Curve 1, $Q_p/Q_d = 0$; Curve 2, $Q_p/Q_d = -0.05$; and Curve 3, $Q_p/Q_d = -0.075(20)$.

and

$$E_2(\xi, \theta, Q_p/Q_d) = \frac{1}{\sin\theta} \frac{\left[1 - t_f(\xi)\right]\left[4(1-3\xi_c)^2 \tan^2\theta + \left(1 + 3\dfrac{Q_p}{Q_d} - 6\xi_c \dfrac{Q_p}{Q_d}\right)^2\right]^{1/2}}{\xi_c(1-\xi_c) + \left[t_f(\xi)\right](\xi - \xi_c)(1 - \xi - \xi_c)} \tag{9.2-43}$$

The time fraction $t_f(\xi)$ as a function of ξ and ξ_c is given in Eq. 9.2-24, and the relationship between ξ and ξ_c appears in Eq. 9.2-22. Thus, the total strain as a function of position t can be evaluated subject to the previously given assumption, without difficulties. Figure 9.13 presents the distribution of total strain as a function of ξ for various Q_p/Q_d values.

It is interesting to note that for pure drag flow the minimum strain is obtained (as expected) at $\xi = 2/3$, but when back pressure is applied ($Q_p/Q_d < 0$), the minimum strain is obtained elsewhere. Yet, like residence time, the total strain is rather uniform over a significant portion of the channel.

The SDF can be calculated by the same procedure used for the RTD function. For pure drag flow, where the minimum strain is obtained at $\xi = 2/3$, it is given by Eq. 9.2-36, with ξ uniquely related to γ in Eq. 9.2-40. For the more general case, however, the fraction of flow rate between $\xi = 2/3$ and ξ is *not* the fraction of flow rate experiencing a total strain of γ or less, as is evident from Fig. 9.13. First, the location of minimum γ must be established, then Eqs. 9.2-30 and 9.2-31 must be integrated over the appropriate limits. An alternative approach, which is also applicable to a plasticating extruder, in which the channel is broken up into small height increments and fluid particles are followed with

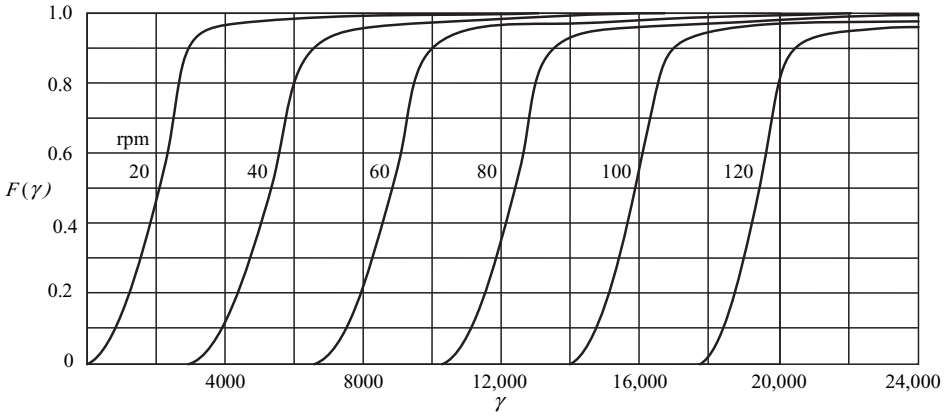

Fig. 9.14 Values of $F(\gamma)$ for a 6-in-diameter, 20:1 *L/D* extruder at constant flow rate (500 lb/h) with screw speed as a parameter. Simulation was made for a square pitched screw with a constant channel depth of 0.6 in. [Reprinted by permission from G. Lidor and Z. Tadmor, ''Theoretical Analysis of Residence Time Distribution Functions and Strain Distribution Functions in Plasticating Extruders,'' *Polym. Eng. Sci*., **16**, 450–462 (1976).]

time, was described by Lidor and Tadmor (24). Figure 9.14 gives the results of such computations for a 6-in-diameter plasticating extruder at 500 lb/h.

Melting is rapid at high screw speeds, and the SDF is essentially that of a melt extruder. Increasing the screw speed at constant flow rate implies an increase in back pressure, and we note a consequent shift of the SDF to higher strain ranges. Once again we observe that SDF in screw extruders is quite narrow. Hence, a good indication of the mixing performance can be obtained by calculating the mean strain $\bar{\gamma}$. The mean strain is proportional to l/H and a function of Q_p/Q_d and the helix angle θ. Figure 9.15 is a generalized plot of $\bar{\gamma}$ as a function of Q_p/Q_d, with the helix angle as a parameter. That the mean strain is proportional to l/H is borne out by engineering practice. Similarly, increasing the mean strain with increasing back pressure is also well supported by experience, and the same holds for the limited effect of the helix angle within the practical range of θ values.

Dispersive Mixing in Screw Extruders

While the common wisdom is that the SSE is a good extensive mixer, at least in the cross-channel direction, it is a poor dispersive mixer. This is not surprising because, as we showed in Chapter 7, good dispersion requires repeated passages of all fluid particles over high shear regions. However, in the single flighted SSE, the only high-shear zone is the flight clearance. Moreover, much of the material never passes or passes once or a few times over the flight and only small fractions pass it repeatedly. Finally, even the material that does pass the flights does not experience the stretching elongational flow, typical to shear regions in dispersive mixers, nor is it exposed to cool solid boundaries that are needed to maintain relatively low temperatures, and thus attain high shear stresses.

Next we derive a simple theoretical model to calculate the passage-distribution function (PDF) in a SSE[11] (25), assuming isothermal Newtonian fluids. We examine a small axial section of length Δl, as shown in Fig. 9.16.

11. In Reference 25 down-channel increments were used for the model. Here we use axial increments.

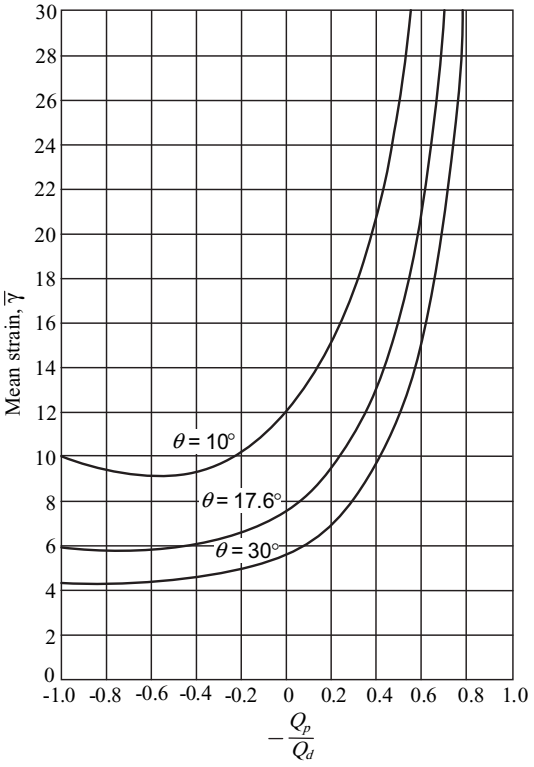

Fig. 9.15 Mean strain as a function Q_p/Q_d ratio with helix angle as a parameter for $l/H = 1$. When $Q_p/Q_d = -1$, γ goes to infinity; this condition corresponds to a closed discharge operation.

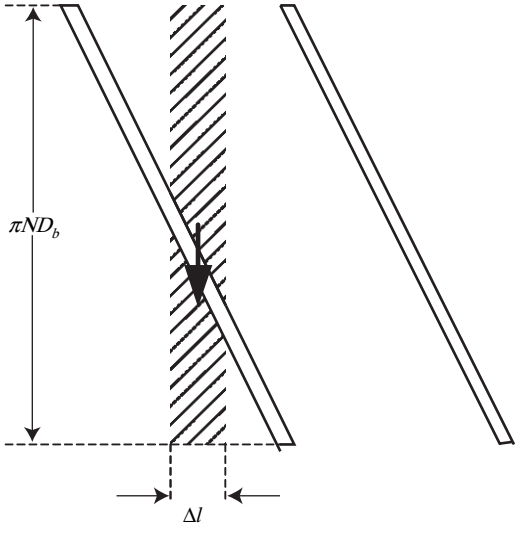

Fig. 9.16 An unwound single flighted screw, showing and axial increment of Δl.

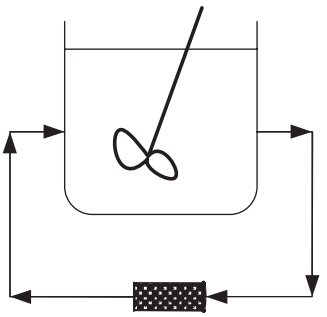

Fig. 9.17 Schematic representation of a well-stirred vessel with a recycling stream over a high-shear zone.

We recall that at closed discharge conditions fluid particles stay at a fixed axial position. This means that the fluid in the crosshatched incremental volume $\Delta V = \pi N \bar{D} H \Delta l$ does not leave it. Some fluid is dragged over the flight and recycled to the bulk, and since within the volume element the fluid circulates due to the drag of the barrel surface, we can model the system as a well-stirred tank with recycle, as shown in Fig. 9.17.

The PDF for this system, as shown in Chapter 7, is given by

$$g_k = \frac{\lambda^k}{k!} e^{-\lambda} \tag{9.2-44}$$

where $\lambda = t/\bar{t}$ is the ratio of the time elapsed to the mean circulation time in the vessel given by the ratio of the volume of the vessel to the volumetric flow rate over the flight. If we assume pure drag flow over the flight and neglect the flight width on the free volume this ratio is

$$\bar{t} = \frac{\pi \bar{D} H \Delta z}{\pi N D_b \Delta z \delta_f / 2} = \frac{2 H \bar{D}}{N D_b \delta_f} \tag{9.2-45}$$

We now extend the model to the positive net flow situation, and assume that the differential volume moves axially. Although the axial flow is not plug flow, this is not an unreasonable approximation because as we recall the RTD is rather narrow. In this case, the elapsed time t becomes the mean residence time in the extruder given by the ratio of screw channel volume and net flow rate

$$t = \frac{\pi L H \bar{D}}{Q} \tag{9.2-46}$$

Substituting Eqs. 9.2.45 and 9.2.46 into the definition of λ gives

$$\lambda = \frac{\pi N L D_b \delta_f}{2Q} = \frac{Q_f}{Q} \tag{9.2-47}$$

where Q_f is defined as the drag flow rate of the flight along the whole extruder. Thus, neglecting the flight width λ is simply the ratio of flow rates over the flight and the net flow rate over the extruder.

Example 9.4 Passage Distribution in a 60-mm Single Flighted Screw Extruder Calculate the PDF in a 60-mm diameter 10/1 *L/D* melt extruder with 0.125-mm flight clearance, turning at 100 rpm and extruding 100 l/h. Neglect the effect of flight width on the volume of the channel.

Solution Using Eq. 9.2-47, we compute the value of λ

$$\lambda = \frac{\pi \times (100/60) \times (10 \times 0.06) \times 0.06 \times 0.125 \times 10^{-3}}{2 \times (100/3600) \times 10^{-3}} = 0.424$$

Turning to Eq. 9.2-44 and substituting λ, yields $g_0 = 0.654$; $g_1 = 0.277$; $g_2 = 0.059$; $g_3 = 0.008$, which implies that in this particular case that 65.4% does not pass over the flight, 27.7 passes once, 5.9% twice, and 0.8% three times, and so on. Good dispersion, as mentioned in Chapter 7, requires 20–30 passages over high-shear zones.

Clearly, the single flighted single screw is a poor dispersive mixer. However, it is possible to design special multiflighted single screws that can provide multiple passages over appropriately designed shearing flights (26,27).

9.3 THE SINGLE SCREW PLASTICATING EXTRUSION PROCESS

Most SSEs used in the plastics industry are ''plasticating extruders,'' that is, they are fed by solid pellets or powder. The solids are fed gravitationally into the hopper and the screw channel, where they are conveyed and compressed by a drag-induced mechanism, then melted, or ''plasticated,'' by a drag-induced melt removal mechanism. Pressurization and mixing take place side by side with the melting step. Hence, the plasticating extrusion process, shown in Fig. 9.18, consists of all four elementary steps: handling of particulate solids in Regions 1, 2, and 3; and melting, pumping, and mixing in Regions 3 and 4. The fifth elementary step, devolatilization, may also occur in Regions 3 and 4 through

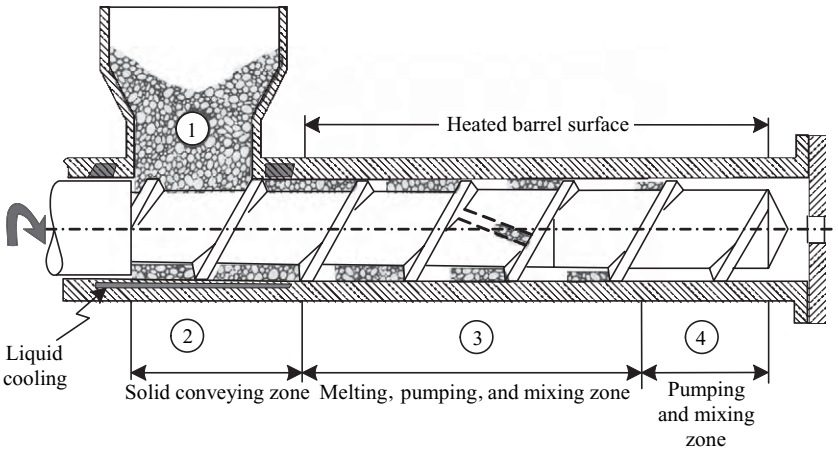

Fig. 9.18 Schematic representation of a plasticating screw extruder. The barrel is cooled in the hopper region and heated downstream. Typical plasticating SSE have length-to-diameter ratios of 24–26.

appropriate screw design (two-stage screw) and operating conditions, providing for a partially filled channel.

The Journey of a Polymer Particle in the Plasticating Extruder

It is easy to visualize the mechanisms that take place in the solids conveying zone of a screw extruder, and to develop appropriate mathematical models describing these mechanisms. This was done by Darnell and Mol (28) in 1956, and their model is discussed later in this section.

However, the melting or plasticating process that follows the solids conveying zone is a relatively complex one, and unlike the melt extrusion and solids conveying processes, the detailed physical melting mechanisms cannot be easily visualized, predicated, and modeled from basic principles without experimental investigation.

Indeed, the qualitative elucidation of the *melting mechanism* and its *quantitative* mathematical formulation by Tadmor (29) was done by observing and analyzing experimental samples obtained by Maddock using an ingenious experimental technique (30). This technique calls for abruptly stopping an extruder operating at steady state, chilling both barrel and screw (thereby solidifying the polymer in the screw channel), pushing out the screw from the barrel, unwinding the solidified helical ribbon of polymer from the screw (Fig. 9.19), and slicing thin representative sections perpendicular to the flights. To better visualize the details of the process, a small amount (3–5%) of colored polymer pellets is added as a tracer. This helps to distinguish between solids filled and molten regions. It also provides some information on flow patterns.

Figures 9.20–9.25 show the results of such ''cooling'' experiments obtained by Tadmor et al. (31) using the Maddock technique. The slices, sectioned every half-turn from the hopper to the die, are shown for each experiment. Next to each slice, the axial location in terms of the turn number (starting downstream from the hopper) is given. Figures 9.20–9.24 were obtained from a 2.5-in-diameter extruder with a metering-type screw having a 12.5 turns feed section with a channel depth of 0.370 in; a 10 turns compression section, and 4-turns-long metering section, 0.127-in deep. Results in Fig. 9.25 were obtained from an 8-in extruder with a metering-type screw. The polymers used and the operating conditions accompany each figure. Figure 9.19 illustrates the relative position of a typical ''slice'' or cross section. Thus the pushing flight is on the left and the trailing flight on the right; the barrel surface is on the top and the root of the screw on the bottom.

Analyzing the experimental results, we note that throughout most of the extruder, the solid and melt phases *coexist* side by side, and are clearly segregated from each other, with

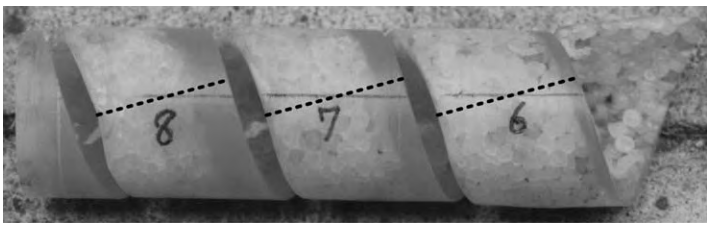

Fig. 9.19 Helical ribbon of LDPE, after it was taken off the screw following a cooling experiment. The numbers indicate turns downstream the hopper and cross sections for examination obtained by slicing it perpendicular to the flights, as shown by the broken line.

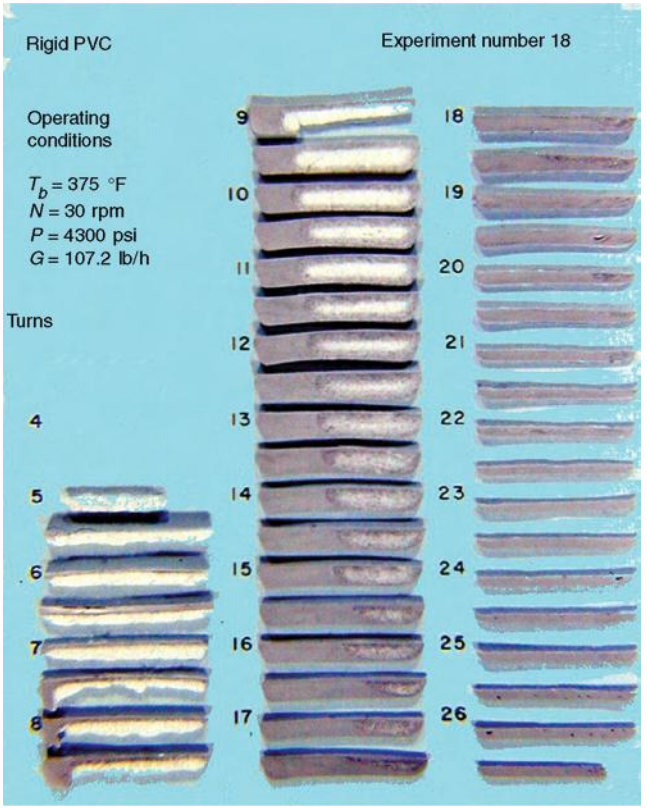

Fig. 9.20 Cross sections obtained from "cooling" experiments of a 2.5-in-diameter 26.5 length-to-diameter ratio screw extruder. Material: rigid PVC. Operating conditions are listed in the figure: T_b is the barrel temperature, N the screw speed, P the pressure at the die, and G the mass flow rate. Numbers denote turns from the beginning (hopper side) of the screw. The screw was of a metering type with a 12.5 turn feed section 0.37 in deep, a 9.5 turn transition section, and a 4.5 turn metering section 0.127 in deep. [Reprinted by permission from Z. Tadmor and I. Klein, *Engineering Principles of Plasticating Extrusion*, Van Nostrand Reinhold, New York, 1970. The experiments were carried out at the Western Electric Engineering Research Center, Princeton, NJ.]

the melt phase accumulating the pushing flight in a *melt pool* and the solids segregated at the trailing flight as a *solid bed*. The width of the melt pool gradually increases in the down-channel direction, whereas that of the solid bed generally decreases. The solid bed, shaped as a continuous long, helical ribbon of varying width and height, slowly turns in the channel (much like a nut on a screw) sliding toward the exit, while gradually melting. Upstream from the point where melting starts, the whole channel cross-section is occupied by the solid bed, which is composed, as the hopper is approached, of less compacted solids. The continuity of the solid bed provides an explanation for the capability of the screw extruder to generate melt that is free of air bubbles: the porous continuous solid bed provides uninterrupted air-filled passages from deep in the extruder all the way back to the hopper. Thus, particulate solids forming the solid bed move down-channel while the air is stationary.

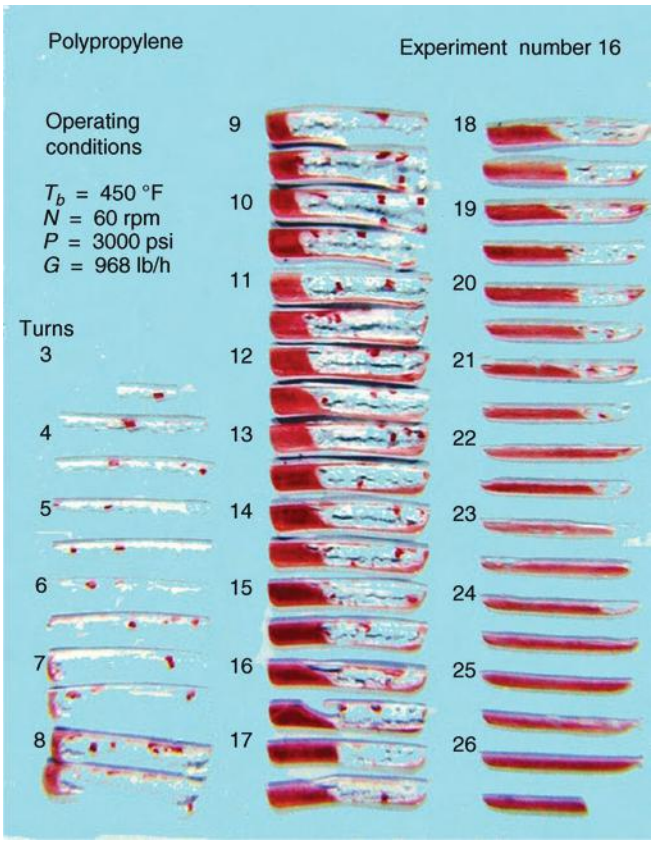

Fig. 9.21 Cross sections obtained from cooling experiments of a 2.5-in-diameter, 26.5 length-to-diameter ratio screw extruder. Material: PP. Operating conditions are listed in the figure ($G = 96.8$ lb/h). Symbols and screw descriptions as in Fig. 9.20.

Although the melting behavior in extruders just described appears to be quite general for amorphous and crystalline polymers, small and large extruders, and diverse operating conditions, it appears that, with certain PVC compounds, the melt pool accumulates at the trailing flight (32). Moreover, with large extruders, there was no segregated melt pool at the channel side, but rather a thickening layer of melt at the barrel surface was observed (33). Finally, dissipative mix-melting may take place in screw extruders under conditions that lead to high pressures in the feed zone. In this section, however, we concentrate on the commonly observed melting mechanism.

It should be noted that melting takes place along most of the extruder. Indeed, the production capacity of plasticating extruders is frequently determined by their plasticating capacity. Further visual analysis of the experimental results reveals a tendency of the melt pool to penetrate ''under'' the solid bed and, occasionally, to completely surround it; the continuity of the solid bed is frequently broken and a melt filled gap appears (e.g., turn 15.5, Fig. 9.23). This tendency for solid bed breakup seems to originate in the tapered sections of the extruder, and it appears to be a source of ''surging'' (i.e., fluctuation in time of temperature, pressure, and flow rate) of the extrudate at the die, as well as a source of entrapping some air bubbles into the melt stream.

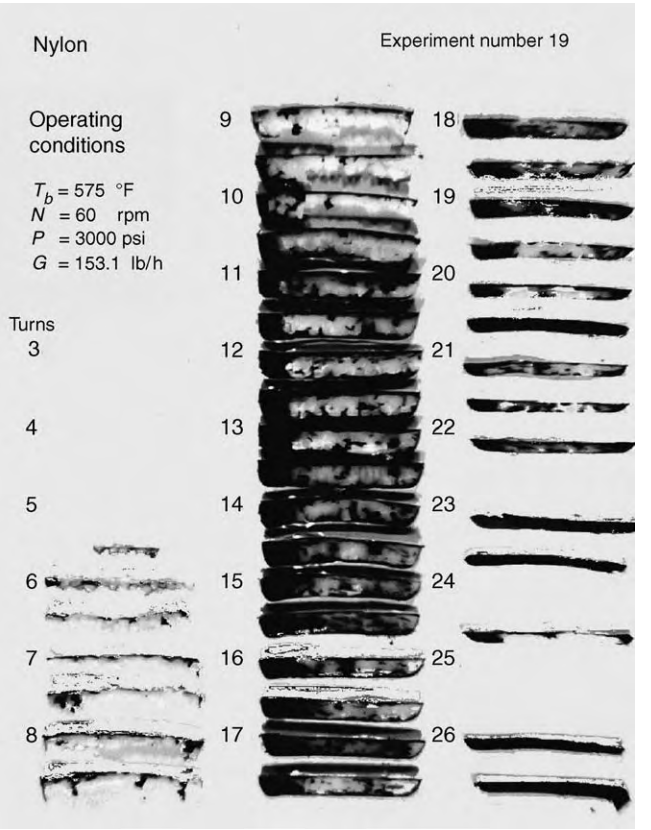

Fig. 9.22 Cross sections from "cooling" experiment. For details see Figs. 9.20 and 9.21. Material: nylon.

A close analysis of an individual cross section (Fig. 9.26) suggests further details on the physical mechanisms taking place in the screw channel. We observe a thin film of melt between the surface of the barrel and the solid bed. The relative motion of the barrel surface in the cross-channel direction drags the melt in the film into the melt pool, generating a cross-channel pressure gradient and a circulatory flow. This hydrodynamically generated pressure in the melt pool no doubt brings about the segregation of the solids at the trailing flight, and since melt is continuously removed by drag from the film, the solid bed must acquire a velocity component toward the barrel surface. But at the same time it also slides down channel; consequently, the size of the solid bed at a fixed position in the bed is continuously reduced until, at the end of melting, it completely disappears. At a fixed position in the screw channel, on the other hand, the size of the solid bed remains constant in time. Thus, all the elements have emerged for a *drag-induced melt removal, steady state, conduction melting mechanism*, discussed in Section 5.7. Moreover, the film region at the barrel surface is the only place where such a mechanism can develop. Recalling the significant difference between the rates of melting in conduction melting with and without melt removal, we can conclude that the melting at the root of the screw (even when there is melt penetration under the solid bed) as well as at the melt pool–solid bed interface, are second-order effects in most of the melting region.

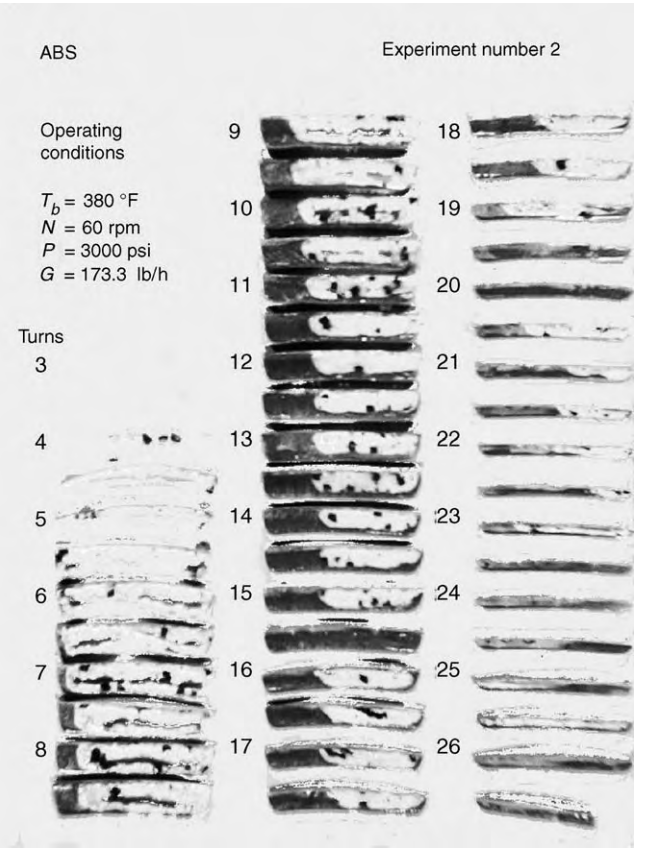

Fig. 9.23 Cross sections from the cooling experiments. See Figs. 9.20 and 9.21. Material: Acrylonitrile-Butadiene-Styrene (ABS).

With this overview on the physical mechanisms of melting in mind, we can proceed to examine the complete experience of the polymer in the extruder. We shall do this by launching a pellet and traveling with it throughout the extruder.

In the hopper, where only the elementary step of solids handling occurs, we commence a slow, somewhat erratic motion downward, repeatedly bumping into neighboring pellets and occasionally being hung up in a stable arch for short periods, until we reach the throat area. Here we observe the pellets in helical flight, being swept from underneath and pushed forward. The moment we are caught up by this flight and start rotating, our coordinate system changes. We now record our motion relative to the screw; hence, the barrel will appear to be rotating in the opposite direction. We find ourselves in a shallow channel confined between the flights, the roots of the screw, and the barrel surface.

We commence in slow motion down the channel, generally maintaining our position relative to the confining walls. As we move, the neighboring pellets exert an increasing force on our pellet, and the void between the pellets is gradually reduced. Most pellets are experiencing the same thing, except for those in contact with the barrel and those in contact with the screw. The former experience an intense frictional drag by the moving barrel surface, while the latter experience a frictional drag force in the up-channel direction by the screw surfaces.

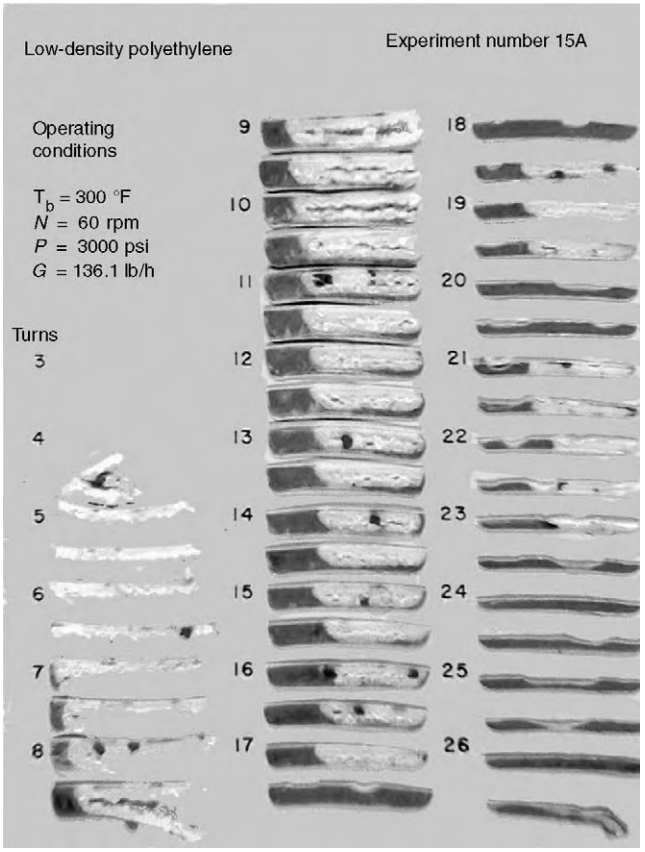

Fig. 9.24 Cross sections from cooling experiments. See Figs. 9.20 and 9.21. Material: Low density polyethylene (LDPE).

We know from Section 4.9 that this frictional drag at the barrel is the driving force of the solids conveying mechanism in the screw channel. Both these frictional processes result in heat generation, raising the polymer temperature, in particular the surface layer at the barrel surface. At some point, this temperature may exceed the melting point or softening range of the polymer, converting the frictional drag mechanism into a viscous drag mechanism. That is, the solids are conveyed forward in the channel by the shear stresses generated in the melt film.

A more common situation, however, is that before there is any significant frictional heating, an axial position is reached where the barrel is heated to well above the melting point, forcing the creation of a film of melt. In either case, this marks the end of that portion of the process in the extruder called the *solids conveying zone*, where only solids are present and the only elementary step that occurs is handling of solids.

By this time, we find our pellet somewhat deformed by the neighboring pellets, which have come together in a rather sturdy, but deformable, solid bed, which is moving in plug-like fashion down-channel. The thin film separating the bed from the barrel is sheared intensely. Heat is generated by this shearing action and conducted from the barrel to the solid bed. The temperature gradient is large because the barrel temperature drops to the melting point over a very thin film. As a result of this heat transfer, from this point on our

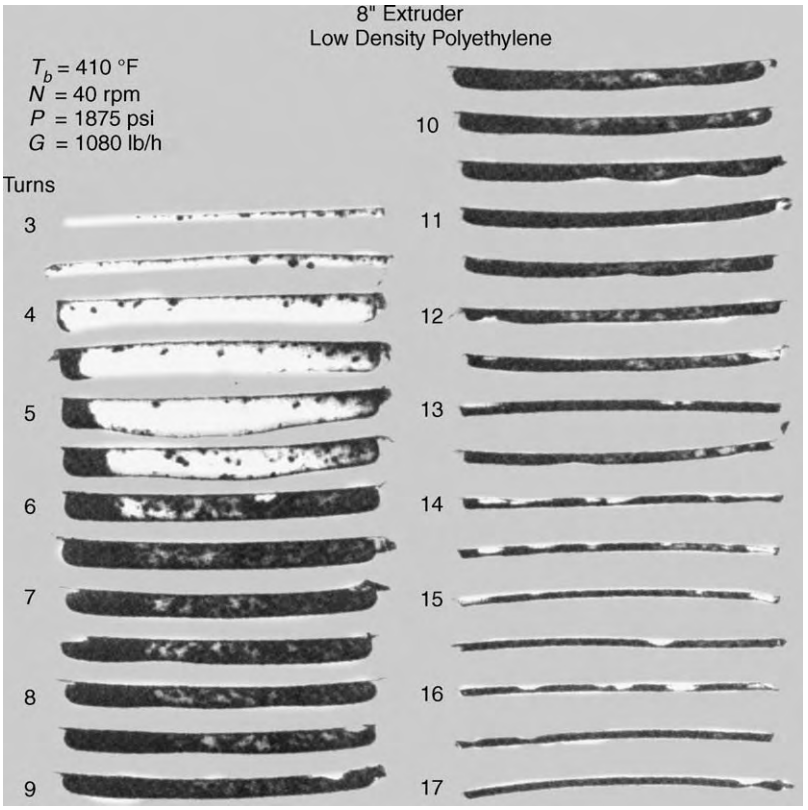

Fig. 9.25 Cross sections obtained from a ‘‘cooling experiment’’ of an 8-in-diameter extruder. Material and operating conditions indicated in the figure. [Reprinted by permission from Z. Tadmor and I. Klein, *Engineering Principles of Plasticating Extrusion*, Van Nostrand Reinhold, New York, 1970.]

pellet experiences a gradual rise in temperature. Since there is a small radial clearance between the tip of the flights and the barrel surface, until the melt film is thinner than the clearance, nothing drastic happens. This condition may continue for a few turns, during which the film thickens beyond the flight clearance. The flights then start to scrape the melt off the barrel and the melt starts accumulating at the pushing flight.

The portion of the process taking place from the end of the solids conveying zone to the point where the melt layer at the barrel surface first appears is called the *delay zone* (34). In this zone, the elementary step of melting occurs simultaneously with handling of solids. The melting mechanism, however, is contact melting without melt removal, but with heat generation in the molten film. In Fig. 9.20, the solids conveying zone ends at turn 3, where barrel heating starts, and the delay zone, which starts at this location, ends at turn 7, where the melt pool begins to form.

Returning to ‘‘our pellet,’’ we note the point where it reaches the end of the delay zone when the solid bed has acquired a small upward velocity toward the barrel surface. At some point in the extruder, our pellet will reach the melt film–solid bed interface, experiencing toward the end of this approach a quick (exponential) rise in temperature up to the melting point. After being converted into melt, our fluid particle is quickly swept

(b)

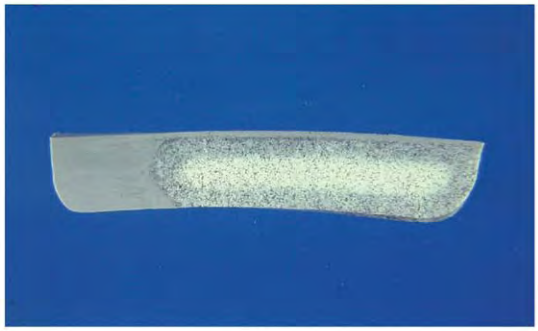

(a)

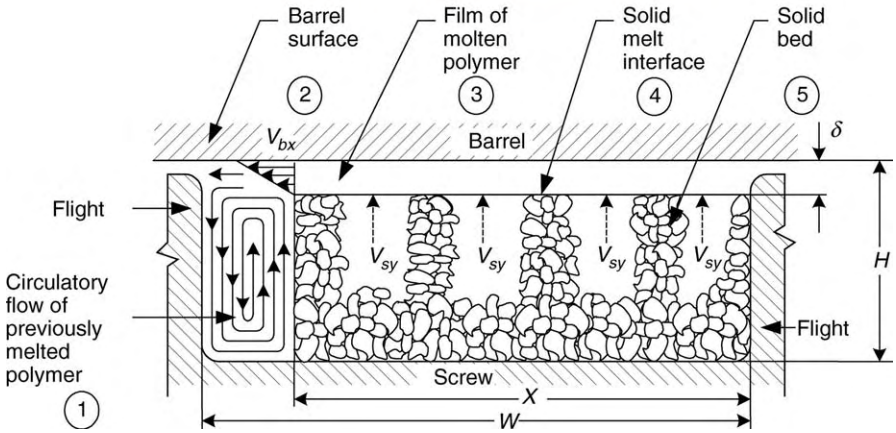

Fig. 9.26 Idealized cross-section compared to (a) the cross-section from a PVC "cooling" experiment and (b) the cross-section from an LDPE "cooling" experiment. [Reprinted with permission from Z. Tadmor and I. Klein, *Engineering Principles of Plasticating Extrusion*, Van Nostrand Reinhold Book Co., New York, 1970.]

into the melt pool. (For amorphous polymers, as the polymer softens, it moves both toward the barrel as well as toward the pushing flight.)

Once in the melt pool, the fluid particle settles at some position in the channel and commences the circulatory flow alternating between two positions. In the upper portion of the channel, it moves toward the pushing flight and down-channel relatively quickly, whereas in the lower portion of the channel, it moves toward the solid bed (which also slides down channel) or trailing flight (if melting is completed) and down channel relatively slowly. This continues until it leaves the screw channel.

In the melt pool, both the temperature and the pressure change; they generally increase. The portion of the process where melting takes place is called the *melting zone*, which lies

side by side with the *melt conveying zone*. The latter extends to the end of the screw. Clearly, then, in the melting zone, *all* elementary steps occur simultaneously; whereas in the melt conveying zone, as discussed in the preceding section, only pumping and mixing take place.

Modeling the Plasticating Extrusion Process

In addition to the modeling objectives listed for melt extruders (i.e., velocity, temperature, and pressure fields), which remain valid for plasticating extrusion, we add the following: gravitational flow behavior of particulate solids in hoppers, in particular pressure distribution, arching, and bridging; stress and temperature distribution of the compressed pellets into a deformable solid body in the solids conveying zone; length of the delay zone (i.e., the length from the axial location where polymer melts at the barrel surface, to the point where the melt is segregated into a melt pool at the pushing flight) and the evolution of the molten film at the barrel surface, as well as temperature and stress fields in the solid bed; length of the melting zone, rate of melting, mean width profile of the solid bed (solid bed profile, or SBP), stress and temperature distribution in the solid bed along the melting zone, mean temperature of the melt film flowing into the melt pool; power consumption in the solids conveying delay and melting zones; and surging conditions. We could generalize our modeling objectives to velocity, temperature, and stress fields in both solid and liquid phases, from which we could calculate all the other variables of interest. But in plasticating extrusion, more than in melt extrusion, it is very difficult to obtain a complete solution to this problem.

We now follow the modeling approach outlined for the melt extrusion process. We assume steady state conditions and a given mass flow rate; then, starting from the hopper, where initial conditions are known, calculations are made in finite steps, ending up at the die, with extrudate pressure, mean temperature, and solids content. If the flow rate at these conditions does not match that of the die, or if the calculations break down for some reason (e.g., insufficient solids conveying), calculations are repeated at a new mass flow rate.

The Solids Conveying Zone The conveying mechanism in screw extruders is one of drag-induced flow, as discussed in Section 4.9. Indeed, for shallow channels, we could turn directly to Eq. 4.9-7, which would form the solids conveying model. The feed section for screw extruders, however, is generally deep, and curvature effects are not negligible. Following Darnell and Mol (28), we derive a solids conveying model in a deep screw channel, subject to simplifying assumptions made in Section 4.9.

At steady state, the solid plug has a constant axial velocity V_{pl} and constant angular velocity $V_{p\theta}$, as sown in Fig. 9.27. The former is related to the mass flow rate by the following equation:

$$G = V_{pl}\rho_b\left[\frac{\pi}{4}\left(D_b^2 - D_s^2\right) - \frac{eH}{\sin\bar{\theta}}\right] \tag{9.3-1}$$

where D_b is the inside diameter of the barrel, $D_s = D_b - 2H$, H is the channel depth, e is the flight width, and $\bar{\theta}$ is the mean helix angle. The down-channel velocity of the solids is $V_{pl}/\sin\bar{\theta}$, which varies with channel depth. (Note that this velocity is equivalent to velocity u in Section 4.9.) It is more convenient to express the flow rate G in terms of the angle ϕ formed between the velocities of the solids and the barrel surface because

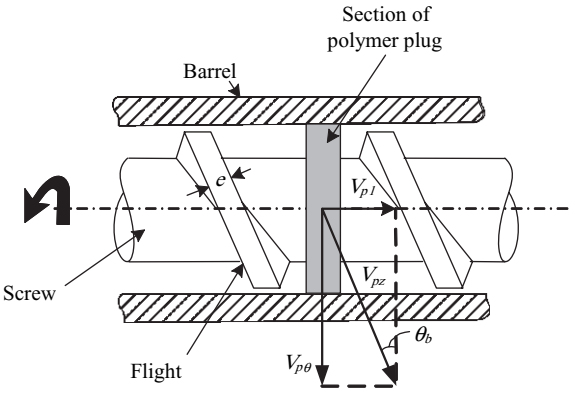

Fig. 9.27 Axial increment of the solid plug. Velocities given relative to a stationary screw: V_{pl} is the axial velocity of the plug, which is independent of the radial position; $V_{p\theta}$ and V_{pz} are the tangential and down-channel components of the plug surface velocity.

force and torque balances provide an expression for this angle. The relationship between V_{pl}, V_b, and the angle ϕ can easily be obtained, as shown in Fig. 9.28:

$$V_{pl} = V_b \frac{\tan\phi \tan\theta_b}{\tan\phi + \tan\theta_b} \tag{9.3-2}$$

where $V_b = \pi N D_b$ is the tangential velocity of the barrel surface. Clearly, at closed discharge conditions, $\phi = 0$ and $V_{pl} = 0$. Substituting Eq. 9.3-2 into Eq. 9.3-1, followed by rearrangements, results in

$$G = \pi^2 N H D_b (D_b - H)\rho_b \frac{\tan\phi \tan\theta_b}{\tan\phi + \tan\theta_b}\left[1 - \frac{e}{\pi\left(D_b - H\sin\bar{\theta}\right)}\right] \tag{9.3-3}$$

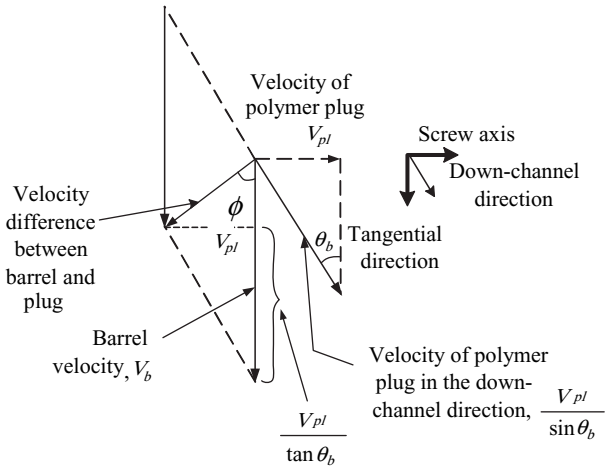

Fig. 9.28 Velocity vector diagram for calculating the velocity difference between barrel and solid plug. This is the velocity of the barrel surface observed by a viewer on the plug; the direction of its velocity relative to the viewer is ϕ.

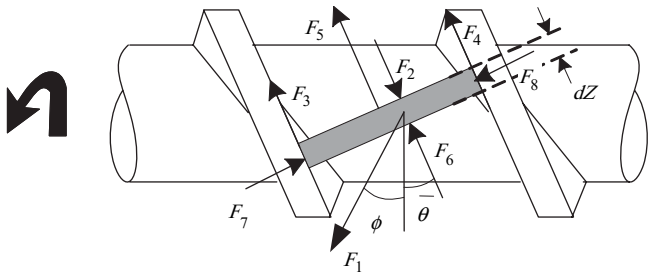

Fig. 9.29 Forces acting on a down-channel increment of the solid plug: F_1 is the forward dragging frictional force exerted on the plug by the barrel surface, $F_6 - F_2$ is the net force resulting from the down-channel pressure gradient, F_3, F_4, and F_5 are the frictional retarding forces of the screw, and F_7 and F_8 are the normal forces by the flights on the plug.

Equation 9.3-3 can be used either to calculate ϕ from G, or vice versa. If bulk density changes cannot be neglected, the calculations should be performed in small axial increments.

Next we proceed with the force and torque balances. Since pressure builds up in the down-channel direction, the force and torque balances are made on a differential increment in the down-channel direction; this is illustrated in Fig. 9.29, where the various forces acting on the element are also depicted. These forces can be expressed in terms of the coefficients of friction, local geometry, and the differential pressure increment, which compensate for the other forces and torques. For an isotropic stress distribution, these are

$$\begin{aligned} F_1 &= f_b P W_b \, dz_b \\ F_6 - F_2 &= H\bar{W} \, dP \\ F_8 &= PH \, d\bar{z} \\ F_7 &= PH \, d\bar{z} + F^* \\ F_3 &= f_s F_7 \\ F_4 &= f_s F_8 \\ F_5 &= f_s P W_s \, dz_s \end{aligned} \tag{9.3-4}$$

where the subscripts b and s, respectively, denote the surfaces of the barrel and the root of the screw, and the overbar denotes the mean value over the channel depth. The motion of the plug consists of a pure translation in the axial direction and pure rotation in the angular direction. Hence, by calculating the components of all the forces in the axial and tangential directions, a force balance can be written in the former direction and a torque balance in the latter direction. By solving the two equations simultaneously, the force F^* is eliminated and, subsequent to considerable algebraic rearrangements, the following simple expression is obtained:

$$\cos\phi = K_s \sin\phi + M \tag{9.3-5}$$

or

$$\sin\phi = \frac{\sqrt{1 + K_s^2 - M^2} - K_s M}{1 + K_s^2} \tag{9.3-6}$$

where

$$K_s = \frac{\bar{D}}{D_b}\frac{\sin\bar{\theta} + f_s\cos\bar{\theta}}{\cos\bar{\theta} - f_s\sin\bar{\theta}} \tag{9.3-7}$$

and

$$\begin{aligned} M = {} & 2\frac{H}{W_b}\frac{f_s}{f_b}\sin\theta_b\left(K_s + \frac{\bar{D}}{D_b}\cot\bar{\theta}\right) + \frac{W_s}{W_b}\frac{f_s}{f_b}\sin\theta_b\left(K_s + \frac{D_s}{D_b}\cot\theta_s\right) \\ & + \frac{\bar{W}}{W_b}\frac{H}{Z_b}\frac{1}{f_b}\sin\bar{\theta}\left(K_s + \frac{\bar{D}}{D_b}\cot\bar{\theta}\right)\ln\frac{P_2}{P_1} \end{aligned} \tag{9.3-8}$$

where P_1 is the initial pressure at $z = 0$ and P_2 is the pressure at any down-channel distance Z_b, where solids conveying is the only elementary step taking place. For a given flow rate, ϕ is obtained from Eq. 9.3-3, M is then calculated from Eq. 9.3-5, and the pressure rise, from Eq. 9.3-8. If a given pressure rise is needed, the process is reversed, with the angle ϕ being calculated from Eq. 9.3-6.

Finally, the total power consumption in the solids conveying zone is obtained by taking the product of the force between the barrel surface and solid plug F_1 and the barrel velocity in the direction of the force $\pi N D_b \cos\phi$

$$dP_w = \pi N D_b \cos\phi f_b W_b P\, dz_b \tag{9.3-9}$$

Integrating Eq. 9.3-9 after substituting the exponential relationship between P and Z_b, as expressed in Eq. 9.3-8, results in (35)

$$P_w = \pi N D_b W_b Z_b f_b \cos\phi \frac{P_2 - P_1}{\ln(P_2/P_1)} \tag{9.3-10}$$

Perhaps the most severe assumption in the Darnell and Mol model is the isotropic stress distribution. Recalling the discussion on compaction in Section 4.5, the stress distribution in the screw channel is expected to be complex. The first attempt to account for the nonisotropic nature of the stress distribution was made by Schneider (36). By assuming a certain ratio between compressive stresses in perpendicular directions and accounting for the solid plug geometry, he obtained a more realistic stress distribution, where the pressure exerted by the solids on the flights, the root of the screw, and the barrel surface are all different and less than the down-channel pressure. The ratio between the former and the latter is of the order of 0.3–0.4.

Another questionable assumption is that of constant temperature. Frictional forces lead to surface-heat generation. The total power introduced through the shaft is partly dissipated into heat at the barrel, flights, and root of the screw surfaces, and is partly used to generate pressure. However, most of the power is dissipated into heat at the barrel surface (Fig. 9.30). This quantity is given by the product of the force F_1 and the relative velocity between barrel surface and solid plug (35)

$$P_{wb} = \pi N D_b W_b Z_b f_b \frac{\sin\theta_b}{\sin(\theta_b + \phi)}\frac{P_2 - P_1}{\ln(P_2/P_1)} \tag{9.3-11}$$

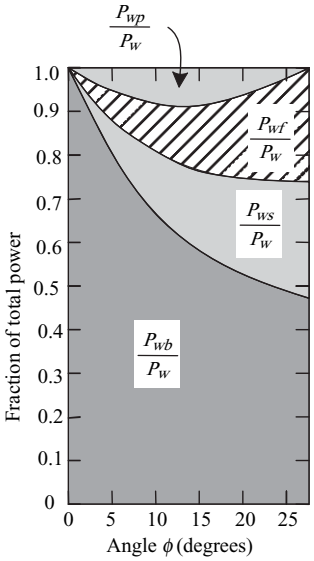

Fig. 9.30 Graphical representation of the various components of the total power consumption in the solids conveying zone of screw extruders for $H/D_b = 0.15$ and a constant f_s/f_b ratio as a function of the angle ϕ: P_{wb}, which is the major component of the power, is the power dissipated into heat at the barrel plug interface; P_{ws} and P_{wf} are the power dissipated on the root of the screw and flights, respectively; and P_{wp} is the power consumed for the pressurization of the plug. [Reprinted by permission from E. Broyer and Z. Tadmor, "Solids Conveying in Screw Extruders, Part I. A Modified Isothermal Model," *Polym. Eng. Sci.*, **12**, 12–24 (1972).]

This heat generated at the interface is partly conducted through the cooled barrel and partly conducted into the solid plug. Consequently, a temperature profile develops in the plug with a maximum temperature at the interface. If we neglect heat generation at the other surfaces, the problem reduces to a one-dimensional heat conduction problem soluble by methods discussed in Section 5.3. Since the rate of heat generation varies with axial location, numerical solution methods are needed. This was achieved by Tadmor and Broyer (37), with the results indicating that the solids surface temperature at the barrel increases exponentially. Clearly, once the melting point is reached, the frictional drag conveying mechanism changes into a viscous drag mechanism (34). This non-isothermal solids conveying mechanism explains the need for efficient barrel cooling in the solids conveying zone if high pressure generation is desired.

Finally, all solids conveying models require an estimate of the inlet pressure P_1. One approach for evaluating P_1 is to assume that it equals the pressure under the granular material at the hopper base (35), which can be evaluated from the equations given in Section 4.3. This approach neglects the complex transition between the gravitational flow in the hopper and the drag-induced flow of the pluglike solid in the closed screw channel. However, it does connect the extruder performance to hopper design and loading level. The need for such a connection follows from experimental observations that, under certain conditions, small variations in solids height in the hopper bring about significant variation in extruder performance, such as, for example, pressure variations at the die. In such cases, keeping the solids height above a certain level eliminates pressure surging at the die. One possible reason for this behavior is the effect of solids height on the inlet pressure.

Another approach to the problem, proposed by Lovegrove and Williams (38,39), is to disregard the hopper and assume that the initial pressure in the solids conveying zone is the result of local gravitational and centrifugal forces. This is a reasonable assumption, considering the generally low level of pressure values in the inlet region. However, it fails to account for the effect mentioned previously, relating the hopper design and loading level to extrusion performance. Clearly, there is a need for additional experimental observation and a detailed mathematical model encompassing the hopper, the portion of the screw under the hopper, and the inlet region in the extruder, where the Darnell and Mol model does not apply.

For an effective solids conveying performance, pressure should rise over this zone. However the maximum theoretical conveying capacity is obtained by setting $P_2 = P_1$. Analysis of the solids conveying equations indicates that there is an optimum helix angle as well as an optimum channel depth for maximum conveying capacity or maximum pressure rise. We pointed out before that P_1 is low; consequently P_2/P_1 must be very high to obtain a substantial pressure level P_2. Increasing P_1 by forced feeding (e.g., with a feeding screw in the hopper) will increase P_2. Equation 9.3-8 indicates that the pressure profile in the solids conveying zone of screw extruders is exponential, as it is in shallow rectangular channels discussed in Section 4.9. Solids conveying is improved by increased f_b/f_s and by increasing the screw speed (ϕ is decreased for a given G), provided that isothermal conditions are maintained and the coefficients of friction remain constant. An accurate measurement of the latter, however, involves some experimental difficulties as discussed in Section 4.1.

Example 9.5 Solids Conveying in Screw Extruders LDPE is extruded in a 6.35×10^{-2}-m (2.5-in) diameter, 26.5 turns long SSE, with a square pitched ($L = D_b$) metering type of screw. The feed section is 12.5 turns long and 9.398×10^{-3} m (0.37 in) deep, the transition section is 9.5 turns long, and the metering section is 3.22×10^{-3} m (0.127 in) deep. Flight width is 6.35×10^{-3} m (0.25 in), and flight clearance is negligible. Hopper diameter is 0.381 m (15 in) and $K = 0.286$, with a converging conical section of 90° and discharge opening of 0.127 m (5 in), as in Fig. E9.5. The barrel temperature is maintained at 149°C (300°F), and heating starts three turns from the beginning of the flights, with the hopper opening occupying the first two turns, leaving one turn for solids conveying. At a screw

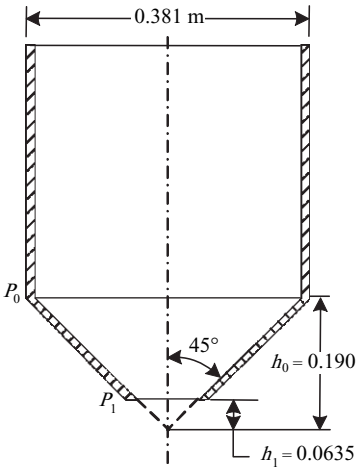

Fig. E9.5 A hopper consisting of cylinder over a truncated cone.

speed of 60 rpm, a mass flow rate of 67.1 kg/hr is obtained with polymer feed at 24°C (screw design and operating conditions correspond to the experiment reported in Fig. 9.24).

Calculate (a) the base pressure of the hopper, (b) pressure at the end of the solids conveying zone, and (c) power consumption in the solids conveying zone.

Assume isothermal operation and that the inlet pressure to the solids conveying zone equals the base pressure of a fully loaded hopper. Bulk density of the feed is 595 kg/m^3, the static coefficient of friction in the hopper is 0.3, and the dynamic coefficients of friction on barrel and screw are 0.45 and 0.25, respectively.

Solution First we compute some geometrical data (needed both in this and the following example), summarized in the following table:

Variable	Feed Section	Transition Section	Metering Section
Helix angle at the barrel surface θ_b	17.65°	17.65°	17.65°
Mean helix angle $\bar{\theta}$	20.48°	Varies linearly	18.45°
Helix angle at the root of the screw θ_s	24.33°	Varies linearly	19.51°
Channel width at the barrel surface, W_b	5.416×10^{-2} m	5.416×10^{-2} m	5.416×10^{-2} m
Mean channel width, $\bar{W}$	5.314×10^{-2} m	Varies linearly	5.358×10^{-2} m
Channel width at the root of the screw, W_s	5.151×10^{-2} m	Varies linearly	5.350×10^{-2} m
Axial length	10.5 turns	9.5 turns	4 turns
Axial length	0.666 m	0.603 m	0.2886 m
Mean helical length, $\bar{z}$	2.270 m	-	0.800 m

(a) We commence calculations in the solids conveying zone. The initial pressure in the solids conveying zone P_1 is assumed to equal the pressure under the solids in the hopper. We can calculate it using Eq. 4.3-5. The value P_0 is evaluated assuming that the height of solids in the vertical part of the hopper is sufficient to result in at least 99% of the maximum pressure. Thus, from Eq. 4.3-5 we have

$$P_0 = \frac{(0.99)(595)(9.806)(0.381)}{(4)(0.3)(0.286)} = 6.412 \times 10^3 \text{ N/m}^2$$

A more accurate calculation of the pressure under the hopper accounting for the conical section outlined in the first edition of the book results in a lower pressure of 3.776×10^3 N/m^2(= 0.55 psi).

(b) The axial velocity of the plug V_{pl} from Eq. 9.3-1, neglecting the effect of pressure on bulk density, is

$$V_{\text{pl}} = \frac{61.7/3600}{(595)\left\{\frac{\pi}{4}\left[(0.0635)^2 - (0.0447)^2\right] - \frac{(0.00635)(0.003226)}{\sin(20.48)}\right\}}$$
$$= 0.0187 \text{ m/s}$$

The velocity of the barrel surface $V_b = \pi N D_b = 0.1995\,\text{m/s}$. Hence, from Eq. 9.3-2, we obtain

$$\tan\phi = \frac{\tan\theta_b}{\left(V_b/V_{pl}\right)\tan\theta_b - 1} = \frac{\tan(17.65)}{(0.1995/0.0187)\tan(17.6) - 1} = 0.13288$$

and ϕ is 7.57°. Next K_s is evaluated from Eq. 9.3-7

$$K_s = \frac{(0.0541)}{(0.0635)}\frac{\sin(20.48) + (0.25)\cos(20.48)}{\cos(20.48) - (0.25)\sin(20.48)} = 0.5859$$

and M is evaluated from Eq. 9.3-5

$$M = \cos(7.57) - 0.5859\,\sin(7.57)$$

The pressure rise ratio P_2/P_1 over one turn of the solids conveying section ($Z_b = 0.0635/\sin 17.6° = 0.209$ m); from downstream the hopper to the location where the barrel heating starts, is obtained from Eq. 9.3-8:

$$\begin{aligned} 0.9141 = {} & (2)\frac{(0.009398)(0.25)}{(0.05416)(0.45)}\sin(17.6)\left[(0.5859) + \frac{(0.0541)}{(0.0635)}\cot(20.48)\right] \\ & + \frac{(0.05151)(0.25)}{(0.05416)(0.45)}\sin(17.6)\left[(0.5859) + \frac{(0.0447)}{(0.0635)}\cot(24.33)\right] \\ & \frac{(0.05314)(0.009398)\sin(20.48)}{(0.05416)(0.209)(0.45)}\left[(0.5859) + \frac{(0.0541)}{(0.0635)}\cot(20.48)\right]\ln\frac{P_2}{P_1} \\ = {} & 0.1676 + 0.34328 + 0.09813\ln\frac{P_2}{P_1} \end{aligned}$$

and this gives $P_2 = 60.9P_1$.

Thus, the exit pressure from the solids conveying zone is $3.776 \times 10^3 \times 60.9 = 2.3 \times 10^5\,\text{N/m}^2$ (33 psi). This result indicates that the solids conveying section functions properly and that higher outputs could be obtained at this screw speed before solids conveying limitations (e.g., ''starving'') were encountered. We should note, however, that the analysis of the solids conveying zone is very sensitive to the values of the coefficient of friction.

(c) The power consumption is calculated from Eq. 9.3-10

$$\begin{aligned} P_w &= (\pi)(1)(0.0635)(0.05416)(0.209)(0.45)\cos(7.57)\cdot\frac{\left(2.3\times10^5\right) - \left(3.776\times10^3\right)}{\ln 60.9} \\ &= 56.7\,\text{W}(= 0.076\,\text{hp}) \end{aligned}$$

The Melting Zone As we pointed out earlier, from the axial location where a melt film is formed at the barrel surface (either as a result of barrel heating or as a result of heat generation due to friction), to the axial location where a melt pool appears at the ''pushing'' flight, lies the *delay zone*. The conveying mechanism in this zone is one of viscous drag at the barrel surface, determined by the shear stresses in the melt film and,

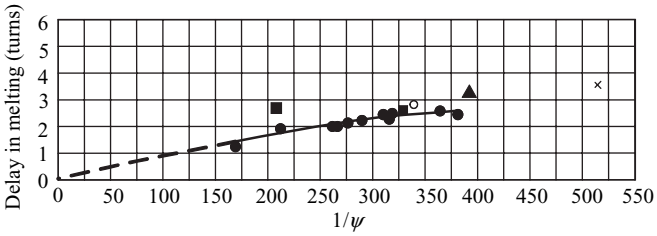

Fig. 9.31 Delay in melting expressed in ''turns'' from the point the barrel temperature exceeds the melting point (melt-film formed) to the point where a melt pool is segregated at the pushing flight, as obtained from cooling experiments versus calculated dimensionless group $1/\psi$. Solid curve for LDPE, ●; HDPE, ○; PP ▲; rigid PVC, ■; nylon, × . [Reprinted by permission from Z. Tadmor and I. Klein, *Engineering Principles of Plasticating Extrusion*, Van Nostrand Reinhold, New York, 1970.]

generally, frictional (retarding) drag on the root of the screw and the flights (34). Thickness of the melt film increases with down-channel distance and attains a value of several times that of the flight clearance at the end of the zone. But to predict the exact axial location where it ends would require information on the strength and stress distribution in the solid bed. Figure 9.31 gives an approximate empirical correlation based on limited experimental data, relating the length of the zone expressed in turns and a dimensionless group ψ related to melting rate, discussed below.

As mentioned earlier, the melting mechanism in screw extruders was first formulated by Tadmor (29) on the basis of the previously described visual observations pioneered by Bruce Maddock. The channel cross section and that of the solid bed are assumed to be rectangular, as in Fig. 9.26. The prediction of the solid bed width profile (SBP), that is the width of the solid bed X as a function of down-channel distance z, is the primary objective of the model, which can be experimentally verified by direct observation via the ''cooling experiment'' of the kind shown in Figs. 9.20–9.25. As shown by Zhu and Chen (40), the solid bed can also be measured dynamically during operation by equipping the extruder with a glass barrel.

The SBP provides a wealth of information: (a) it gives the total length of melting; (b) it offers a detailed view of the melting process, its efficiency and the interaction with screw geometry; (c) it gives an indication of likelihood of surging (i.e., time variation in flow rate and temperature); (d) it provides the width profile of the melt pool needed to compute pressure and temperature profiles along the screw; and (e) it guides the design engineer in the selection of the best location for mixing elements and barrier flights.

The model assumes steady state, which implies that the SBP is constant in time, as are the velocity and temperature profiles in the solid and melt phases. It is further assumed that melting takes place *only* at the barrel surface, where a drag-induced melt removal mechanism exists. The solid bed is assumed to be homogeneous, deformable, and continuous. Next we assume that the *local* down-channel velocity of the solid bed is constant. Slow variations of this velocity (e.g., possible acceleration in the tapered section), as well as those of physical properties (e.g., density of the solid bed), operating conditions (e.g., barrel temperature), and geometry, (e.g., channel depth) can easily be accounted for by a calculation procedure involving small, finite, down-channel increments. This can be viewed as an ''extended lubrication approximation,'' whereby changes in the direction of the main flow are assumed to be small as compared to changes in the perpendicular direction to this flow, and local changes are functions of local

conditions only. Finally, the fluid is assumed to be Newtonian, the local physical and thermophysical properties are assumed to be constant, and the solid bed–melt film interface is assumed to be a sharp interface at the melting point T_m.

The change in size of the solid bed over a small down-channel increment will depend on the rate of melting at the solid bed–melt film interface. Consider a small differential volume element, perpendicular to the solid–melt interface (Fig. 9.32). The solid bed has a local down-channel velocity V_{sz} and a local velocity component into the melt film of V_{sy}. The barrel surface velocity V_b is resolved into down-channel and cross-channel components V_{bz} and V_{bx}.

The relative velocity between barrel surface and solid bed is

$$\boldsymbol{V}_j = \boldsymbol{V}_b - \boldsymbol{V}_{sz} \tag{9.3-12}$$

or

$$\left|\boldsymbol{V}_j\right| = \left(\boldsymbol{V}_j \cdot \boldsymbol{V}_j\right) = \left(V_b^2 + V_{sz}^2 - 2V_b V_{sz}\cos\theta\right)^{1/2} \tag{9.3-13}$$

which determines the rate of viscous dissipation. For a linear velocity profile, the shear rate is V_j/δ, where δ is the local film thickness. The melt in the film, however, is removed only in the *cross-channel* direction, by the cross-channel velocity component of the barrel surface V_{bx}, which drags the melt into the melt pool, resulting in a reduction of solid-bed width. No such effective removal mechanism is possible in the down-channel direction; indeed, the film thickness variation in the down-channel direction is small.

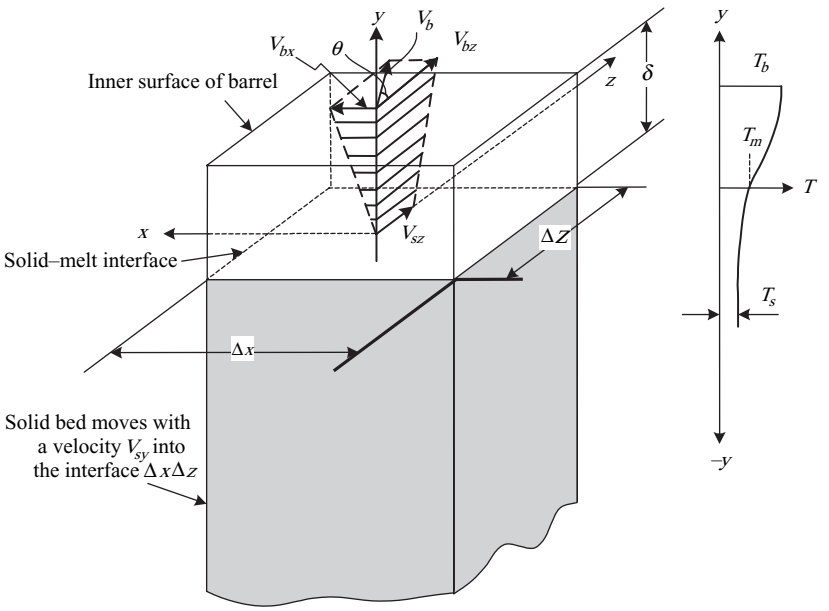

Fig. 9.32 A differential volume element perpendicular to the melt film–solid bed interface. Schematic view of temperature profile in the film and solid bed shown at right. Schematic views of velocity profiles (isothermal model) in the x and z directions are also shown.

In view of these assumptions, neglecting small changes in the down-channel direction over the differential element dz, we deal with a thin slice of solid bed that has a molten film, whose thickness varies in the x direction, and we regain the basic melting mechanism discussed in detail in Section 5.7. In particular, we can turn directly to Eq. 5.7-38, with solid-bed width, X, replacing W, T_b replacing T_0, V_{bx} replacing V_0 in the first term, and V_j replacing V_0 in the second term, to obtain the rate of melting per unit down-channel distance

$$w_L(z) = \left\{ \frac{V_{bx}\rho_m \left[k_m(T_b - T_m) + (\mu/2)V_j^2 \right] X}{\lambda + C_s(T_m - T_{s0})} \right\}^{1/2} \tag{9.3-14}$$

In this equation, the effect of convection on the temperature distribution in the melt film was neglected. This effect, however, is hardly negligible, and since equations with convection terms are hard to solve, we wish to include an approximate accounting for the effect.

Consider an imaginary model in which the newly melted polymer at the melt–solid interface is removed (by a Maxwell-type demon) and then brought to the location $x = 0$, heated up to the local melt temperature, and fed to the melt film. Thus, with convection into the film approximately taken care of in this fashion and the heat needed to heat up the melt from melt temperature to the cup-average temperature of the film accounted for. Moreover, with this approximation the film thickness can be assumed to remain constant with a fully developed velocity and temperature profile. The thermal energy needed to bring the ''removed'' melt from the melting point to the local melt-film temperature, which should be added to the heat of fusion, is given by $C_m\bar{\Theta}(T_b - T_m)$, where $\bar{\Theta}$ is the mean ''cup'' average temperature of the melt given in Eq. 5.7-33

$$\bar{\Theta} = \frac{2}{3} + \frac{\mathrm{Br}}{12} \tag{9.3-15}$$

where Br is the Brinkman number defined in Eq. 5.7-28 which, for a Newtonian fluid, reduces to

$$\mathrm{Br} = \frac{\mu V_j^2}{k_m(T_b - T_m)} \tag{9.3-16}$$

Deriving the rate of melting expression expressed in Eq. 9.3-14 under these conditions, we obtain the following expression

$$w_L(z) = \left\{ \frac{V_{bx}\rho_m \left[k_m(T_b - T_m) + (\mu/2)V_j^2 \right] X}{2[\lambda + C_s(T_m - T_{s0}) + C_m\bar{\Theta}(T_b - T_m)]} \right\}^{1/2} \tag{9.3-17}$$

Comparing the two equations, we note that, in the denominator, we have the total thermal energy needed to bring the solid from inlet temperature to mean melt temperature, including heat of fusion, and a factor of $\sqrt{2}$. Thus, as expected, neglecting convection would result in an overestimation of the rate of melting.

Given the rate of melting in Eq. 9.3-17, we make the following differential mass balance in the down-channel direction

$$\rho_s V_{sz}(H - \delta)X\big|_z - \rho_s V_{sz}(H - \delta)X\big|_{z+\Delta z} = w_L(z)\,\Delta z \tag{9.3-18}$$

which at the limit of $\Delta z \to 0$, neglecting the change in film thickness in the down-channel direction, results in

$$-\frac{d(HX)}{dz} = \frac{w_L(z)}{\rho_s V_{sz}} \tag{9.3-19}$$

By substituting Eq. 9.3-17 into Eq. 9.3-19, we get

$$-\frac{d(HX)}{dz} = \frac{\Phi\sqrt{X}}{\rho_s V_{sz}} \tag{9.3-20}$$

where

$$\Phi = \left\{ \frac{V_{bx}\rho_m \left[k_m(T_b - T_m) + (\mu/2)V_j^2 \right]}{2[\lambda + C_s(T_m - T_{s0}) + C_m\bar{\Theta}(T_b - T_m)]} \right\}^{1/2} \tag{9.3-21}$$

For a constant channel depth, Eq. 9.3-21 can be integrated to give

$$\frac{X}{W} = \frac{X_1}{W}\left[1 - \frac{\psi(z - Z_1)}{2H}\right]^2 \tag{9.3-22}$$

where X_1 is the solid bed width at location $z = Z_1$, and ψ is a *dimensionless* number that characterizes the rate of melting given by

$$\psi = \frac{\Phi}{V_{sz}\rho_s\sqrt{X_1}} \tag{9.3-23}$$

If Z_1 is the location of the beginning of the melting zone, then $X_1 = W$. The SBP can be computed from Eq. 9.3-22. If conditions change in the down-channel direction (e.g., the barrel temperature), computations can be made in small, down-channel increments.

For tapered channels with constant taper

$$-\frac{dH}{dz} = A \tag{9.3-24}$$

Eq. 9.3-20 can be written as

$$\frac{d(HX)}{dH} = \frac{\Phi\sqrt{X}}{A\rho_s V_{sz}} \tag{9.3-25}$$

which can be integrated to give

$$\frac{X}{W} = \frac{X_1}{W}\left[\frac{\psi}{A} - \left(\frac{\psi}{A} - 1\right)\sqrt{\frac{H_1}{H}}\right]^2 \tag{9.3-26}$$

where X_1 is the solid bed width at the down-channel location where the channel depth is H_1. The down-channel location is obtained from Eq. 9.3-24.

Equations 9.3-22 and 9.3-26 are the basic equations of the melting model. We note that the solid-bed profile in both cases is a function of one *dimensionless* group ψ, which in physical terms expresses the ratio of the local rate of melting per unit solid–melt interface $\Phi\sqrt{X_1}/X_1$ to the local solid mass flux into the interface $V_{sz}\rho_s$, where ρ_s is the local mean solid bed density. The solid-bed velocity at the beginning of melting is obtained from the mass-flow rate

$$V_{sz} = \frac{G}{\rho_s HW} \tag{9.3-27}$$

where H is the channel depth at the beginning of melting. In Eq. 9.3-27 we neglected the effect of the melt film. The solid bed velocity was measured experimentally (1f) and proved to remain virtually constant in the feed and moderately tapered sections. In extreme cases, however, and in particular for large tapers and for low rates of melting, solid bed acceleration is possible, as discussed earlier.

A better insight into the nature of the melting model can be obtained by first considering melting in a constant depth channel, with constant ψ throughout the melting zone. The latter implies both constant physical properties and constant solid bed velocity. Equation 9.3-22 with $Z_l = 0$ and $X_1 = W$ reduces to

$$\frac{X}{W} = \left(1 - \frac{\psi}{2}\frac{z}{H}\right)^2 \tag{9.3-28}$$

where ψ reduces in this case to

$$\psi = \frac{\Phi}{V_{sz}\rho_s\sqrt{W}} = \frac{\Phi\sqrt{W}H}{G} \tag{9.3-29}$$

Equation 9.3-28 indicates that the solid bed profile in a constant-depth channel is parabolic. The total (down-channel) length, Z_T, of melting is obtained from Eq. 9.3-28 by setting $X = 0$ to give

$$Z_T = \frac{2H}{\psi} \tag{9.3-30}$$

We therefore note that the length of melting is inversely proportional to ψ; that is, it is proportional to mass flow rate and inversely proportional to the rate of melting. Clearly, through Φ in Eq. 9.3-21, the effect of the various operating conditions on the length of melting can be evaluated. Thus, an increase in screw speed at a constant flow rate brings about an increase in the rate of melting, both because melt removal is improved (V_{bx} increases), and because viscous dissipation increases. An increase in barrel temperature initially brings about an increase in the rate of melting because the conduction term $k_m\ (T_b - T_m)$ increases. But because further increases in the barrel temperature decrease the melt-film viscosity and the amount of viscous dissipation, there is an optimum barrel temperature for maximum melting rate. (There is, however, an additional reason for the existence of the optimum, as we shall see later.) Finally, an increase in solids feed temperature, T_{s0}, increases the rate of melting and reduces Z_T.

Similar conclusions are drawn by considering melting in a tapered section with initial channel depth H and taper $A = dH/dz$. In this case, Eq. 9.3-26 reduces to

$$\frac{X}{W} = \left[\frac{\psi}{A} - \left(\frac{\psi}{A} - 1\right)\sqrt{\frac{H}{H - Az}}\right]^2 \tag{9.3-31}$$

and the total down-channel length, Z_T, of melting

$$Z_T = \frac{H}{\psi}\left(2 - \frac{A}{\psi}\right) \tag{9.3-32}$$

Comparing Eq. 9.3-32 to Eq. 9.3-30, we note that the length of melting in a tapered channel is always shorter than in a channel of constant depth.

Furthermore, the higher the taper, the shorter the melting, Z_T. But there is a limit to the taper that can be allowed, because a high taper may lead to conditions under which the solid bed width will tend to increase instead of decrease (the cross-sectional area, of course, always decreases), which may lead to plugging of the screw channel, solid bed acceleration, and surging conditions in general. It is common practice to characterize the tapered sections of screws by "compression ratio," that is, the ratio of the channel depth in the feed section to that in the metering section, although, from the preceding discussion, screw taper rather than compression ratio should be the value by which transition sections are characterized.

Figure 9.33 illustrates the effect of taper on the shape of the calculated SBP. The width of the solid bed drops if $A/\psi < 1$, it stays constant if $A/\psi = 1$, and it increases if $A/\psi > 1$. All these cases have been experimentally observed. An increase in solid bed width means that the reduction in channel depth is faster than the rate of melting. This condition frequently occurs in a tapered section following a constant depth feed section. Thus, at the beginning of the taper, $X < W$, and an increase in X is possible without generating either surging conditions or a breakdown of the drag removal melting mechanism. If, however, melting starts in a tapered section and conditions are such that $A/\psi > 1$, a stable drag removal melting mechanism, as described in this section, may not be attainable. Conceivably, under these conditions, other melting mechanisms may be triggered into action, such as the previously mentioned *dissipative mix-melting* discussed in Chapter 5.

Conditions that result in approximately constant solid bed width in the tapered section are desirable, and frequently used. Even moderate solid-bed width increases may often be tolerated. The experimentally measured SBPs of Figs. 9.20, 9.22, and 9.24 are plotted in Figs. 9.34–9.36. As predicted by the model, in all cases the solid bed drops continuously in the feed section (up to turn 12), it changes slope upon entering the tapered section, with plugging type conditions observed with nylon and stable constant width conditions observed with LDPE. In the metering section, experimental measurements are inaccurate because solid-bed breakup occurs, or because the bed is too narrow. These particular melting conditions are the combined result of operating conditions, screw design, and polymer properties.

The calculated SBPs in Figs. 9.34–9.36 are based on a model that is no different in concept from the one discussed previously, except that some of the simplifying assumptions were eliminated. In particular, a Power Law model fluid, with a temperature dependent parameter, replaces the Newtonian constant viscosity fluid assumption.

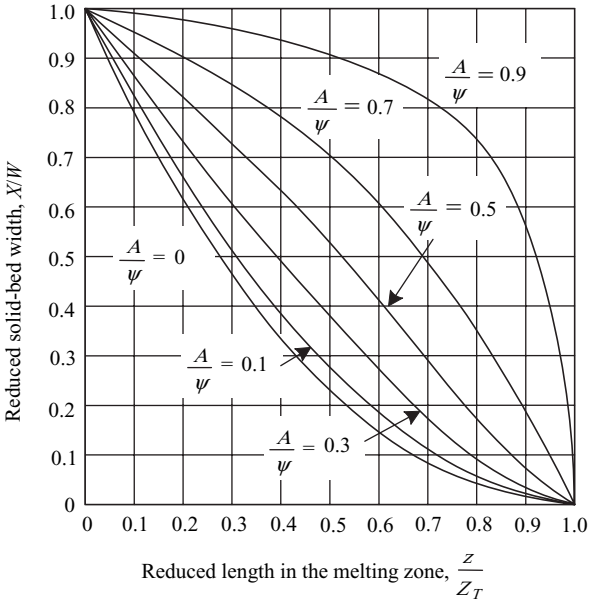

Fig. 9.33 Calculated SBP versus reduced length of melting in a single-section screw: $A/\psi = 0$ denotes a constant channel-depth section. The SBP becomes increasingly concave as A/ψ increases, either as a result of an increasing taper (i.e., increasing A) or a decreasing rate of melting (i.e., decreasing ψ). [Reprinted by permission from Z. Tadmor and 1. Klein, *Engineering Principles of Plasticating Extrusion*, Van Nostrand Reinhold, New York, 1970.]

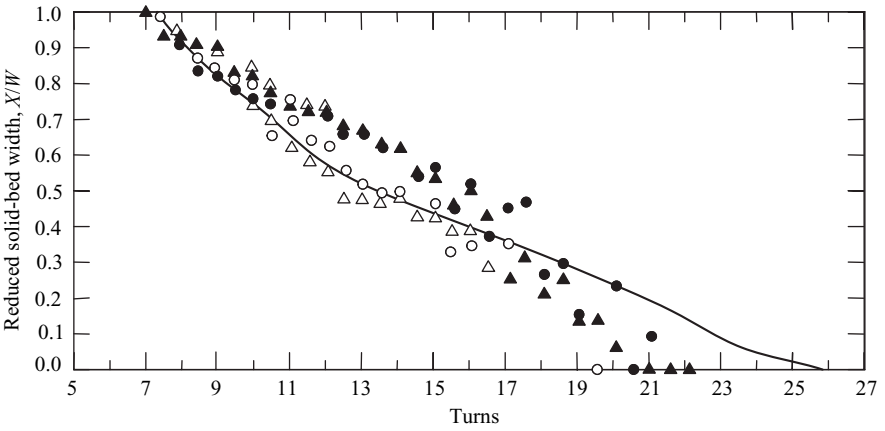

Fig. 9.34 Experimentally measured SBPs by "cooling" experiments as in Fig. 9.20 (PVC) and theoretically calculated SBP (solid curve). Circles and triangles denote two identical experiments. Solid circles and triangles denote solid-bed width at the barrel surface (maximum); open circles and triangles represent the solid-bed width at the root of the screw (minimum). Operating conditions as follows: $T_b = 375°$; $N = 30$ rpm; $P = 4300$ psi; $G = 107.2$ lb/h. [Reprinted by permission from Z. Tadmor and I. Klein, *Engineering Principles of Plasticating Extrusion*, Van Nostrand Reinhold, New York, 1970.]

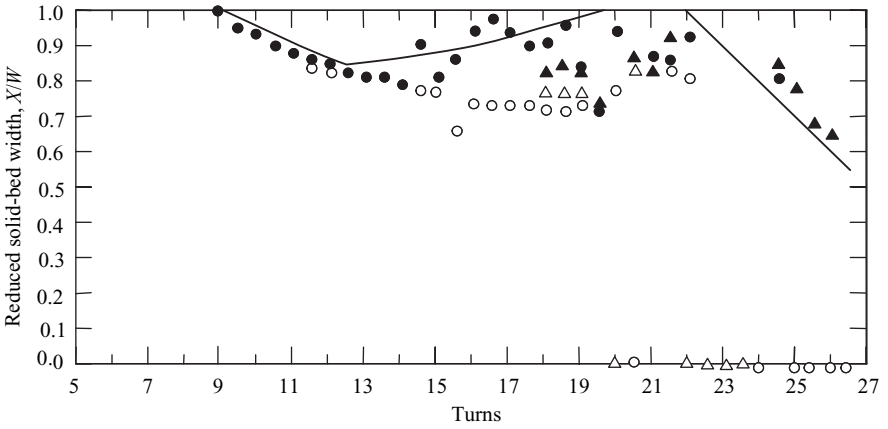

Fig. 9.35 Experimentally measured SBPs, by "cooling" experiments as in Fig. 9.22 (nylon) and theoretically calculated SBP (solid curve). Circles and triangles as in Fig. 9.34. Note the increasing solid-bed width in the tapered section. Operating conditions as follows: $T_b = 575°F$; $N = 60$ rpm; $P = 3000$ psi; $G = 53.1$ lb/h. [Reprinted by permission from Z. Tadmor and I. Klein, *Engineering Principles of Plasticating Extrusion*, Van Nostrand Reinhold, New York, 1970.]

Moreover, flight clearance and curvature effects were also accounted for. Figure 9.37 indicates that, in this particular case, the simple Newtonian model provides a reasonable estimate, although it overestimates the rate of melting. Note that the predicted curve should approach the closed circles and triangles, which are the measured solid bed width at the melt film, rather than the open circles and triangles, which are the corresponding values at the root of the screw. As observed experimentally, the width near the root of the screw is reduced as a result of melt pool circulation.

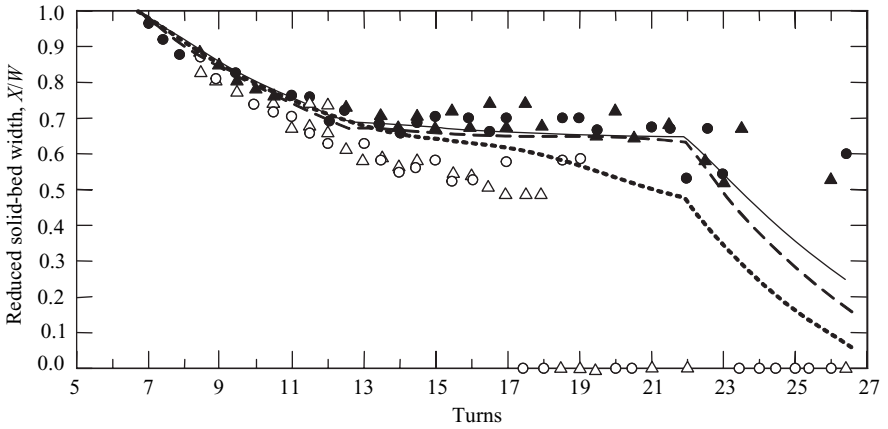

Fig. 9.36 Experimentally measured SBPs by "cooling" experiments as in Fig. 9.24 (LDPE) and theoretically calculated SBP (solid curve). Circles and triangles as in Fig. 9.34. Upper broken curve is the result of the calculation of the SBP in Example 9.6. Lower broken curve is the result of a simplified Newtonian model. Operating conditions as follows: $T_b = 300°F$; $N = 60$ rpm; $P = 3000$ psi; $G = 136.1$ Ib/h. [Reprinted by permission from Z. Tadmor and I. Klein, *Engineering Principles of Plasticating Extrusion*, Van Nostrand Reinhold, New York, 1970.]

In the melting model already described, the assumption of constant viscosity is particularly troublesome, since very large variations of viscosity are expected because of the large temperature variations. The rate of drag removal melting for a Power Law model fluid with temperature dependent viscosity is given in Eq. 5.7-55. The corresponding value of Φ, once again accounting for convection (31), is

$$\Phi = \left\{ \frac{V_{bx}\rho_m U_2[k_m(T_b - T_m) + U_1]}{2[C_s(T_m - T_{s0}) + \lambda + C_m\bar{\Theta}(T_b - T_m)]} \right\}^{1/2} \tag{9.3-33}$$

and the film thickness δ is

$$\delta = \left\{ \frac{[2k_m(T_b - T_m) + U_1]X}{\rho_m V_{bx} U_2 \left[C_s(T_m - T_{s0}) + \lambda + C_m\bar{\Theta}(T_b - T_m)\right]} \right\}^{1/2} \tag{9.3-34}$$

where U_2 is given by Eq. 5.7-51 (see Example 9.3)

$$U_2 = 2\frac{\left(1 - b' - e^{-b'}\right)}{b'(e^{-b'} - 1)} \tag{9.3-35}$$

and b' is defined[12] as

$$b' = \frac{-a(T_b - T_m)}{n} \tag{9.3-36}$$

and U_1 is given by in Eq. 5.7-53

$$U_1 = 2m_0 V_j^{n+1}\bar{\delta}^{1-n}\frac{\left(e^{-b'} + b' - 1\right)}{(b')^2}\left(\frac{b'}{1 - e^{-b'}}\right)^{n+1} \tag{9.3-37}$$

Equation 9.3-37 for constant viscosity Newtonian fluid ($n = 1$, $\mu = m_0$, and $a = 0$) reduces to μV_j^2. Finally, the mean temperature of the film $\bar{\Theta}$ is given by Eq. 5.7-57

$$\bar{\Theta} = \frac{b'/2 + e^{-b'}(1 + 1/b') - 1/b'}{b' + e^{-b'} - 1} \tag{9.3-38}$$

Modifications of this model, including a nonlinear temperature profile in the melt film, channel curvature effects, and an approximate method to account for the flight clearance effect, are presented by Tadmor and Klein (1), together with expressions for power calculations. Numerous other improvements of the melting model have been suggested in the literature (33,41–46). A detailed discussion of these, however, is beyond the scope of this text.

Example 9.6 Melting in Screw Extruders The screw geometry and operating conditions for the LDPE extrusion experiment (Figs. 9.24 and 9.36) were given in Example 9.5. Calculate the SBP, using the Power Law model with temperature-dependent viscosity and linear temperature profile.

12. Note that for $T_b > T_m, b' < 0$ and is identical to A_4 in Reference 1.

We assume that the polymer melt follows the Power Law model in the shear-rate and temperature ranges of interest

$$\eta = 5.6 \times 10^4 e^{-0.01(T-110)} \dot{\gamma}^{-0.655}$$

where η(N·s/m^2) is the non-Newtonian viscosity, T (°C) is the temperature, and $\dot{\gamma}$ (s^{-1}) the shear-rate. The melt density as a function of pressure and temperature follows the empirical relationship

$$\rho_m = 852.7 + 5.018 \times 10^{-7} P - 0.4756T$$

where ρ_m (kg/m^3) is the density, P (N/m^2) the pressure, and T (°C) the temperature. The melting point of the polymer T_m is 110°C, its thermal conductivity k_m is 0.1817 W/m°C, and heat capacity C_m is 2.596 kJ/kg°C. The density of the solid polymer is 915.1 kg/m^3, its heat capacity C_s is 2.763 kJ/kg°C, and the bulk density of the feed at atmospheric pressure is 595 kg/m^3. The heat of fusion is 129.8 kJ/kg.

Solution In this example we know the location of the beginning of the melting zone from experimental data. As Fig. 9.24 indicates, melting starts at turn number 7. Hence, we can proceed with the SBP calculation without evaluating the length of the delay zone. The first step is calculating Φ from Eq. 9.3-33. In the expression for Φ, we have the variables U_2, U_1, and $\bar{\theta}$, which we calculate from Eqs. 9.3-35, 9.3-37, and 9.3-38, respectively, with b' evaluated from Eq. 9.3-36:

$$b' = \frac{-(0.01)(149 - 110)}{(0.345)} = -1.1304$$

hence, U_2

$$U_2 = (2)\frac{1 + (1.1304) - e^{1.1304}}{(-1.1304)(e^{1.1304} - 1)} = 0.814$$

The physical meaning of this result is that the drag removal action of the barrel is reduced by a factor of 0.814 as a result of the temperature profile in the film on which the shear thinning effect is superimposed.

The down-channel velocity of the solid bed is obtained from Eq. 9.3-27

$$V_{sz} = \frac{(67.1/3600)}{(915.1)(0.009398)(0.05314)} = 0.0408\,\text{m/s}$$

The velocity of the barrel surface is

$$V_b = \pi(1)(0.0635) = 0.1995\,\text{m/s}$$

The absolute value of the velocity difference $\boldsymbol{V}_b - \boldsymbol{V}_{sz}$ from Eq. 9.3-13 is

$$V_j = \left[(0.1995)^2 + (0.0408)^2 - (2)(0.1995)(0.0408)\cos(17.65)\right]^{1/2}$$
$$= 0.161\,\text{m/s}$$

To calculate U_1 from Eq. 9.3-37, we must simultaneously solve Eqs. 9.3-34 and 9.3-37 with the aid of Eq. 9.3-38

$$U_1 = (2)\left(5.6 \times 10^4\right)(0.161)^{1.345}\ \delta^{0.655}\frac{\left[e^{1.1304} - (1.1304) - (1)\right]}{(1.1304)^2}\left(\frac{1.1304}{e^{1.1304} - 1}\right)^{1.345}$$
$$= 3163.8\delta^{0.655}$$

The mean dimensionless temperature $\bar{\Theta}$ from Eq. 9.3-38

$$\bar{\Theta} = \frac{e^{1.1304}\left[(1) - (1.1304)^{-1}\right] + (1.1304)^{-1} - (1.1304)/2}{e^{1.1304} - 1.1304 - 1} = 0.700$$

In Equation 9.3-34, for δ we face a difficulty with the density, whose value is a function of pressure and temperature. The pressure varies with the down-channel location, which couples the melting with melt conveying. This is a *weak* coupling, however, and we shall use a constant density at a mean temperature of $T = (0.7)(149 - 110) + 110 \approx 137^{\circ}C$ and estimated mean pressure of $6.89 \times 10^6\ \mathrm{N/m^2}(= 1000\ \mathrm{psi})$. Thus with $\rho_m = 791\ \mathrm{kg/m^3}$, Eq. 9.3-34 results in

$$\delta = \left\{\frac{[(2)(0.1817)(149 - 110) + U_1]X}{(0.1995)\sin(17.65)(0.814)(791)[(2763)(110 - 24) + (129.8 \times 10^3) + (2596)(0.638)(149 - 110)]}\right\}^{1/2}$$
$$= 2.438 \times 10^{-4}[(14.17 + U_1)X]^{1/2}$$

Next, we solve U_1 and δ simultaneously for a few X values. Results are given in the following table:

X (m)	U_1 (N/s)	δ (m)
0.055	16.07	3.144×10^{-4}
0.035	13.46	2.398×10^{-4}
0.025	11.81	1.965×10^{-4}

We note that the value of δ is very small compared to the channel depth. Next, from Eq. 9.3-33 we obtain

$$\Phi = \left\{\frac{(0.1995)\sin(7.65)(791)(0.814)[(0.1817)(149 - 110) + 0.5U_1]}{(2)(2763)(110 - 24) + (129.8 \times 10^3) + (2596)(0.638)(149 - 110)}\right\}^{1/2}$$
$$= 4.7474 \times 10^{-3}(14.17 + U_1)^{1.5}\ \mathrm{kg/s \cdot m^{1.5}}$$

By comparing U_1 values from the table to the value of 14.17, we note that viscous dissipation and heat conduction are about equal in this case.

Since melting starts in the feed section, we use Eq. 9.3-22 to compute the SBP. Melting starts at turn 7, and the constant channel feed section ends at turn 12.5. There are, therefore, 5.5 turns of constant channel depth that are left for melting to take place. Since Φ depends on U_1, which is a function of X, we make the calculation in increments. For this example, we take increments

one turn long and evaluate δ, U_2, and Φ at conditions prevailing at the entrance of the increment. A more accurate calculation procedure would involve the evaluation of these variables at conditions prevailing in the middle of each increment. In this example, this involves the solid bed width X appearing in the expression for δ. Hence, iterative calculation procedures are needed for this purpose. Such a procedure can easily be carried out on a computer. We calculate ψ from Eq. 9.3-23 subsequent to solving for U_1 and Φ by interpolation in the table (for the interpolation, we use $\delta_1/\delta_2 = X_1/X_2$). Results of the computations are tabulated below. When the SBP is calculated with Eq. 9.3-22, in the first increment, we use $X_1/W = 1$, and then the exit solid bed width of the upstream increment equals the inlet solid-bed width in the following increment:

Increment		Inlet Conditions				
Start (turns)	End (turns)	X_1 (m)	U_1 (N/s)	Φ (Kg/s·m$^{1.5}$)	ψ	X/W End of Increment
7	8	5.416×10^{-2}	15.99	0.0261	3.0006×10^{-3}	0.934
8	9	5.060×10^{-2}	15.64	0.0259	3.0862×10^{-3}	0.871
9	10	5.717×10^{-2}	15.28	0.0257	3.1173×10^{-3}	0.810
10	11	4.389×10^{-2}	14.71	0.0255	3.2616×10^{-3}	0.752
11	12	4.074×10^{-2}	14.14	0.0253	3.3521×10^{-3}	0.697
12	12.5	3.774×10^{-2}	13.79	0.0251	3.4617×10^{-3}	0.670

In the tapered section, we follow the same procedure in principle, but use Eq. 9.3-26 to calculate the SBP. The mean taper is

$$A = \frac{(9.398 \times 10^{-3}) - (3.226 \times 10^{3})}{(9.5)(6.35 \times 10^{-2})/\sin(19.51)} = 3.4169 \times 10^{-3}$$

Results are shown in the following table:

Increment		Channel Depth × 1000			Inlet Conditions					
Start (turns)	End (turns)	Start H_1 (m)	End H_2 (m)	H_1/H_2	X_1(m) × 100	U_1 (N/s)	Φ (Kg/sm$^{1.5}$)	ψ × 1000		X/W End of Increment
12.5	14.5	9.3980	8.0986	1.1604	3.628	13.61	0.025	3.519	1.030	0.667
14.5	16.5	8.0986	6.7993	1.1911	3.612	13.60	0.025	3.525	1.032	0.663
16.5	18.5	6.7993	5.4999	1.2362	3.592	13.57	0.025	3.534	1.034	0.658
18.5	20.5	5.4999	4.2005	1.3093	3.563	13.54	0.025	3.546	1.038	0.651
20.5	22.0	4.2005	3.2260	1.3020	3.525	13.49	0.025	3.562	1.042	0.643

From turn 22 to turn 26.5, we once again have a constant channel section, which is computed by the same procedure as in the feed section. The channel depth in Eq. 9.3-22 is that of the metering section.

Increment		Inlet Conditions				
Start (turns)	End (turns)	X_1 (m)	U_2 (N/s)	Φ (Kg/s·m$^{1.5}$)	ψ	X/W End of Increment
22	23	3.482×10^{-2}	13.44	0.0249	3.580×10^{-3}	0.502
23	24	2.720×10^{-2}	21.14	0.0243	3.955×10^{-3}	0.381
24	25	2.065×10^{-2}	11.10	0.0239	4.448×10^{-3}	0.279
25	26.5	1.511×10^{-2}	10.02	0.0233	5.087×10^{-3}	0.158

The fraction of unmelted polymer leaving the screw is obtained from the last X/W value. The fraction of unmelted polymer in the extrudate is G_s/G, where

$$\frac{G_s}{G} = \frac{(X/W)\bar{W}HV_{sz}\rho_s}{G} = \frac{(0.158)(3.585 \times 10^{-2})(3.226 \times 10^{-3})(0.0408)(915.1)}{67.1/3600}$$
$$= 0.055$$

Such a level of unmelted polymer can frequently be tolerated, because the screen pack and the die itself provide additional opportunities for melting and mixing.

Figure 9.36 plots the calculated SBP as a broken curve compared to experimental data. We note that the agreement is generally good except in the metering section where, as a result of the solid bed breakup, experimental data are scattered. The parabolic drop in constant depth sections, the sharp break in the slope of the SBP upon entering the tapered section, as well as the approximately constant solid-bed width (which is the combined result of channel taper and operating conditions) are all clearly evident in the experimental results and were predicted by the model. The solid curves are the result of computations with a more accurate model accounting for flight clearance and channel curvature effects (approximately offsetting each other in this example), as well as nonlinear temperature distribution in the film of melt and reevaluation of the rheological parameters at the local conditions. Nevertheless, the example demonstrates that calculations with a relatively simple model provide useful results.

Melt Conveying In a plasticating extruder, two distinct melt conveying regions can be found. One is downstream of the melting zone after the completion of melting, where the models derived in the preceding section can be applied without modifications. In addition, melt conveying occurs in the melt pool, which extends side by side with the solid bed profile. Here, the width of the melt pool changes in the flow direction. Moreover, the mass-flow rate of melt also changes as a result of the influx from the melt film. Both these quantities, as well as the mean melt-film temperature, are obtained from the melting model. Hence, the melt conveying model can be applied approximately to calculate local pressure gradients and temperature changes over small, finite axial increments using the mean local flow rate and melt pool size (1,47). The result of these calculations is the pressure and melt temperature profile over the length of the extruder.

Simulation of the Complete Process Having broken down the extrusion process into a series of submodels (solids flow in the hopper, solids conveying, melting and melt conveying), we are now in a position to combine these intimately interconnected submodels into a complete whole model, capable of simulating the whole plasticating extrusion process. This, however, requires a great deal of computation, which was made possible and convenient in the 1960s,

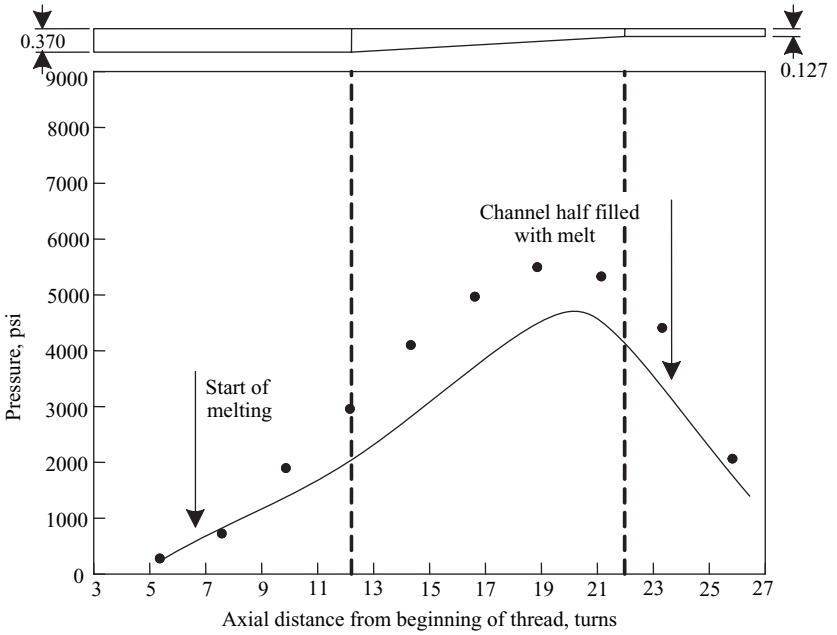

Fig. 9.37 Simulated and measured pressure profiles for an LDPE extruded in a 2.5-in-diameter, 26.5 length-to-diameter ratio extruder, with a metering-type screw having 12.5 feed section with channel depth of 0.37 in and 4.5 turns of metering section of depth of 0.1275. The flow rate is 136 lb/h, the screw speed 60 rpm, and the barrel temperature was set at 300°F. The SBP is shown in Fig. 9.24. The screw geometry is shown at the top of the figure. Simulation was carried out by the first computer simulation package for plasticating extrusion developed by the Western Electric Princeton Engineering Research Center team (17). [Reprinted by permission from Z. Tadmor and I. Klein, *Engineering Principles of Plasticating Extrusion*, Van Nostrand Reinhold, New York, 1970.]

when the theoretical model of melting was developed, by the revolutionary advent of digital computers. Indeed, the simulation of the plasticating extrusion process pioneered by the Western Electric Engineering Research Center team (17) was among the first *computer-aided design* (CAD) engineering software packages. Since that time numerous commercial computer simulation packages for extrusion have been developed and marketed.

Figure 9.37 presents the pressure profile of the experiment described in Fig. 9.24, simulated by the first complete extruder computer simulation package for plasticating extrusion developed by the Western Electric. Princeton Engineering Research Center team (17). As indicated, the simulated pressure profile agrees well with the measured one.[13] The program, of course, simulates the whole process, predicting, in addition to the pressure profile, among others the SBP, the melt temperature profile, residence times and strain, degree of fill in vented regions, power consumption (and power breakdown for the various functions), and expected temperature surging at the die.

13. It is worth noting that the simulation of the pressure profile is the most sensitive from all other simulated variables. Under many operating conditions minor changes in input data as, for example, geometry (e.g., flight clearance and metering channel depth), or operating conditions (e.g., screw speed) can result in very large variations in the predicted pressure values. Therefore, a parameter sensitivity study should be carried out to better judge the accuracy of predictions.

In this class of models, it is assumed that the melting step strongly affects the melt pumping step, but the possible impact of the latter on the former is neglected. In effect, the melt in the pool exerts pressure and viscous drag on the solid bed, which, together with the viscous drag over the melt film, the root of the screw, and the trailing flight, determine the stress distribution in the solid bed. Such an analysis coupling the two phases has been attempted (33,46), and in principle, it may provide the means to predict solid deformation, acceleration, and breakup.

Mixing in plasticating extruders is closely related to melting. In the melt channel, laminar mixing takes place, as is evident in the uniform color in the previously described melting experiments. Clearly, however, mixing can only be completed after all solids melt. In a well-designed ordinary screw extruder this should happen only toward the end of the screw leading to exit composition fluctuations in time and space as well as temperature fluctuations. However, both the effectiveness of melting and that of mixing can be significantly improved by mixing sections and barrier-type screws, as described in the following subsection.

Finally, we comment on residence distribution in plasticating extruders. Tracer measurement will indicate a relatively narrow RTD, because the solid moves as a plug and the RTD of the melt pool is quite narrow as well, as discussed earlier. But what matters for polymers is the RTD in a *molten state*. This, as shown by Lidor and Tadmor (24), may be quite wide, as is the SDF.

Screw Designs

The classic plasticating screw consisted of three sections: a deep-channel feed section, a tapered melting section, and a shallow metering section. The feed section must be deep enough to accommodate the low bulk density plastics pellets, to generate the necessary torque to convey the solids, and to generate sufficient pressure to compact the bed into a solid bed. The barrel in the feed section is cooled to sustain frictional drag by the barrel surface. Sometimes axial or helical grooves are machined into the barrel to create an effective higher coefficient of friction and thus increase the solids conveying efficiency. Much of the melting takes place in the relatively long tapered section. The decrease in channel depth is needed not to compensate for the increasing density of the solids, as is sometimes claimed, but to improve the melting efficiency. This is clearly suggested by the melting mechanism and the melting model supports it quantitatively. Finally the metering section, which really does not exclusively *meter* the flow rate, as this is determined jointly by the upstream sections and the metering section. Nor does it exclusively generate the pressures at the die—as often pressure drops in this region—but being shallow it can homogenize reasonably well the melt that contains partially molten regions left over from the melting zone, and bring them to a more uniform temperature. This function of the metering section can be improved by inserting into the channel ''mixing pins,'' as shown in Fig. 9.38, or by a variety of mixing heads attached to the screw, as shown in Fig. 9.39.

The elucidation of the melting mechanism has triggered a productive period of innovation in screw design. Most of these screw designs are *barrier*-type screws, that is, an auxiliary flight is added such that it starts at the ''pushing flight'' and ends at the ''trailing flight''; thus, it separates the solids from the melt in the main screw channel. The auxiliary flight has a larger flight clearance then the primary flight. This way, solids entering the screw channel cannot generally leave the screw without having to pass over the flight clearance of the auxiliary flight. Thus, solids are barred from leaving the screw.

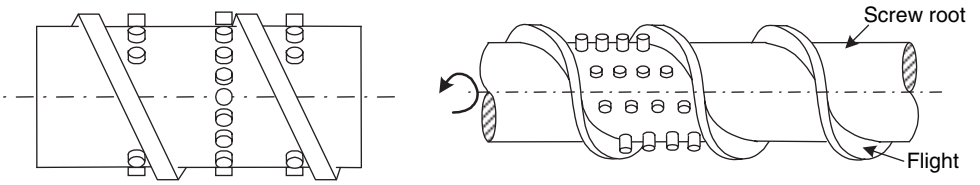

Fig. 9.38 Two arrangements of mixing pins in the screw channel.

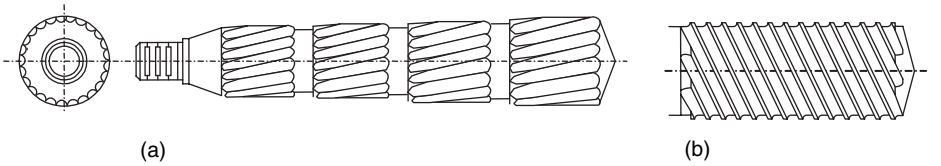

Fig. 9.39 Various mixing heads. (a) Torpedo extension. (b) Dulmage screw.

There are many barrier-type screws that differ from each other by the channel depth profiles of the melt and solids channels, by the helix angles, profiles, and the number of flights. We briefly review here just a few if these types of screw. The first barrier-screw design is due to C. Maillefer[14] and is shown in Fig. 9.40, in which the auxiliary channel follows roughly the solid-bed profile. Clearly, at certain conditions the auxiliary flight can restrict flow rate, but at all times it prevents solids from leaving the screw.

The MC-3 screw, shown in Fig. 9.41, developed by the Waldron Hartig Division of the Midland Ross Corporation, improves upon the Maillefer screw, maintaining from a certain down-channel point a constant helix angle of the auxiliary flight, with increasing depth in the melt channel (to accommodate the increasing melt flow rate), and a diminishing solids conveying channel, until the converge. The Dray and Laurence screw is very similar, but the helix angle of the primary channel is increased up to a point to create more space for the melt channel, as is the Kim Screw, in which the helix angle is continuously increased.

The Efficient screw of the Feed Screws Division, New Castle Industries, shown in Fig. 9.42, has a constant helix angle in the feed section, but at the point the auxiliary flight begins the helix angle increases, providing space for the new barrier flight and the melt channel. After the width of the new melt channel is established, the flights remain parallel through the transition section. Toward the end of the melting zone the open-ended melt channel merges with the solids channel.

Finally, the Union Carbide Bruce Maddock Fluted Screw Section, shown in Fig. 9.43, is really a compressed barrier-type screw, whereby the mixture of melt and solids enters a set

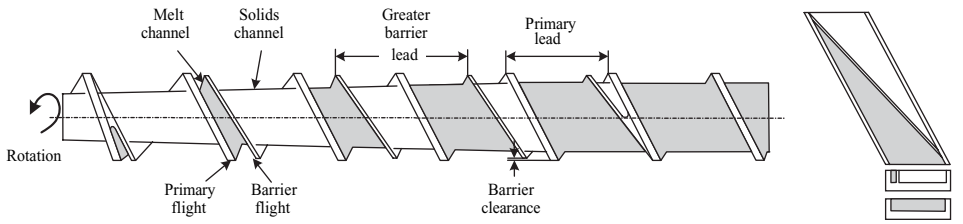

Fig. 9.40 Schematic view of the Maillefer barrier type screw.

14. C. Maillefer, *Mod. Plast*., **40**, 132 (1963).

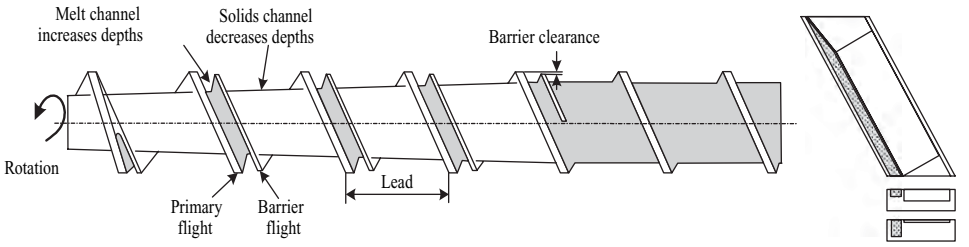

Fig. 9.41 Schematic view of the MC-3 of the Waldron Hartig Division of the Midland Ross Corporation. Smooth gray color indicates melt.

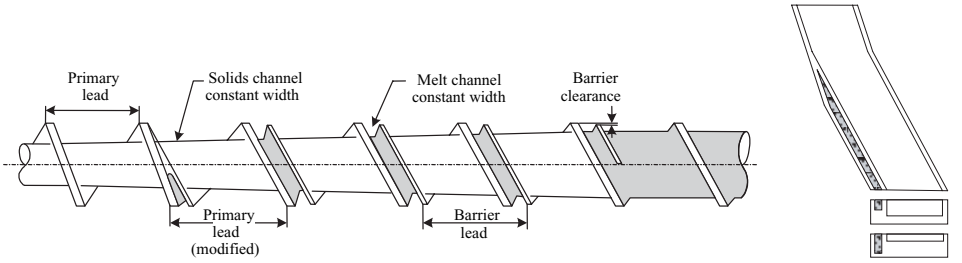

Fig. 9.42 Schematic view of the Efficient barrier-type screw by the Feed Screws Division, New Castle Industries. Smooth gray color indicates melt.

of parallel axial flutes or channel and is dragged by the barrel across barrier flights to a set of parallel exit flutes. The barrier flights do not separate solids from the melt, but merely prevent solids from leaving until they are melted. The pressure loss over the Maddock device, which was analyzed theoretically by Klein and Tadmor (49), is small and in certain conditions it may generate pressure. The device is frequently located at the end of the screw like a mixing head, or about two-thirds of the way downstream from the feed port.

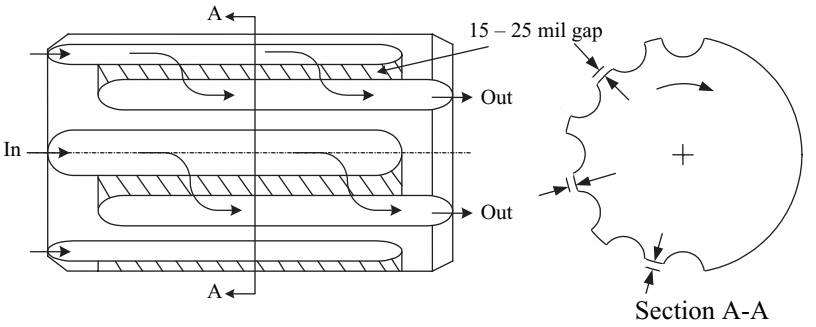

Fig. 9.43 The Union Carbide Maddock Fluted Mixing Screw Section.

9.4 THE CO-ROTATING DISK PLASTICATING PROCESSOR

Sections 9.2 and 9.3 discussed the elementary steps that make up the important and widely used screw extrusion process. The common and outstanding feature of all the elementary steps taking place in the screw channel is that they are induced by drag brought about by a single moving surface—that of the barrel. Solids are conveyed and compressed by the

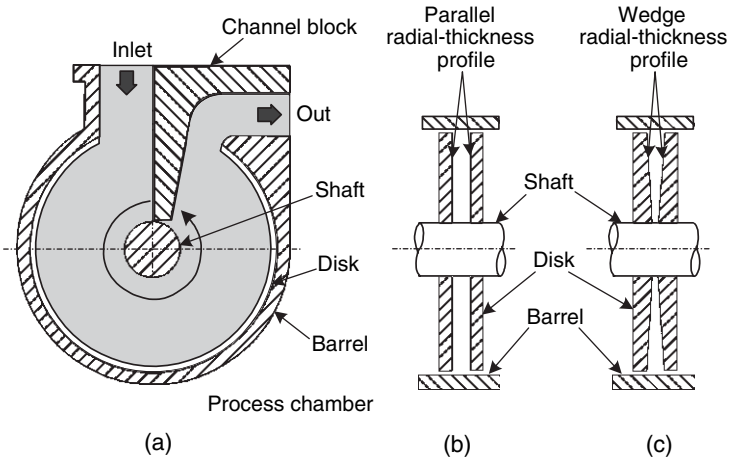

Fig. 9.44 (a) Schematic view of a co-rotating disk configuration. The disks are attached to the rotating shaft and enclosed in a housing. The channel block separates between inlet and outlet. (b) Parallel disk geometry and (c) wedge-shaped disk geometry.

frictional drag of the barrel surface; they are melted in a drag removal melting step, and the melt is pressurized and mixed by drag-induced flow. The other main surface of the channel, the stationary root of the screw, has no useful operational function except as a geometrical boundary. In fact, the efficiency of the elementary steps is even retarded by it.

In Section 6.2, however, we saw that, at least for pumping, there is a plethora of alternative geometrical configurations capable of generating pressure by a drag-induced mechanism. Specifically, in Section 6.6 we examined the *co-rotating disk* configuration based on Building Block 2 from Fig. 6.2 of jointly moving parallel plates. Table 6.1 summarized the design equation of such a pump.

In this section we examine the plasticating co-rotating disk configuration functioning as a complete plastics processor[15] in which all the elementary steps take place (49–51). This configuration demonstrates that it is possible to process (i.e., to melt, mix, devolatilize, and pump) polymers in machines other than screw-based ones, whether single or twin. This, we believe, will help the reader to better understand screw machines as well. In addition, it provides yet another demonstration of how to mathematically model processing machines.

In screw extruders, as we have seen, the processing takes place in the helical channel formed between the screw and the barrel. In a co-rotating disk processor (CDP), on the other hand, processing takes place in flat doughnut-shaped *processing chambers* formed by two neighboring disk surfaces, the inner surface of the barrel, the shaft to which the disks are attached, and the *channel block* attached to the barrel, with very small clearance to the disk surfaces. It thus blocks the channel and separates inlet from outlet, as shown in Fig. 9.44. Processing chambers can be connected in series, parallel, or any other

15. The CDP was developed by the Farrel Corporation in Ansonia, CT, and sold under the trade name Diskpack. Although over a dozen machines were manufactured, sold, and used in industry, the line was discontinued. A retrospective analysis of this development, which is instructive regarding the uphill battle of many engineering innovations that radically depart from the traditional practices, is given in Z. Tadmor, "Machine Invention, Innovation and Elementary Steps," *Adv. Polym. Technol.*, **21**, 87–97 (2002).

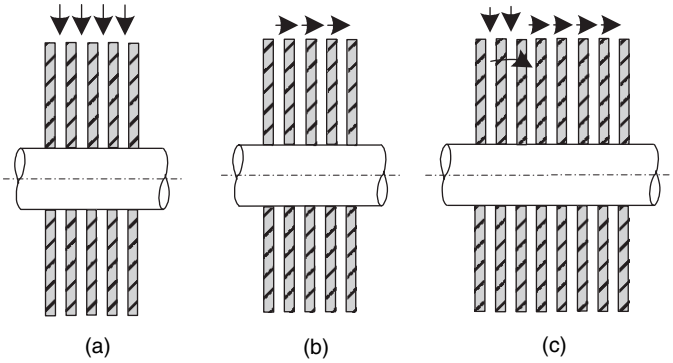

Fig. 9.45 Multiple disks attached to the shaft with (a) processing chambers connected in parallel, (b) processing chambers connected in series, and (c) combined parallel and series connection.

combination, as shown in Fig. 9.45. Generally, each chamber is designed to perform one of the elementary steps.

Example 9.7 Schematic Design of a Diskpack Co-rotating Disk Compounder Before discussing the mechanism and modeling of the various elementary steps in the processing chambers, and in order to gain a better understanding of this machine concept, we discuss the structure of a co-rotating disk compounder manufactured by the Farrel Corporation under the trade name Diskpack. This is shown schematically in Figure E9.7a.

This figure shows a schematic but representative design of a Diskpack compounder with 12 processing chambers. In this particular design, solids are fed in parallel into six melting chambers. The molten material is transferred through an axial transfer channel machined into the housing upstream of the channel block to a single mixing chamber (7). This mixing chamber is equipped with three mixing blocks (A, B, and C). Mixing blocks are similar to channel blocks, but have larger, wedge-shaped clearances to enable molten material to pass, thereby undergoing high shear stress. The channel block, which is 90° off the prior one forces the melt into another transfer channel, feeding two additional mixing–venting chambers in parallel (8 and 9). These chambers have a secondary port, either for adding additives or venting. In the latter case, a spreading insert (marked A) deposits the melt on the disk surfaces. Before exiting, the melt is mixed with yet another mixing block (B). Next the melt from the mixing–venting chambers is fed into a mixing–homogenizing chamber (10), also equipped with three mixing blocks (A, B, and C). Finally, the melt is transferred to a wedge-shaped pumping chamber, which normally operates partially filled, because a fraction of the circumference suffices to generate the pressure needed to extrude the melt through the die. Outboard of the pumping chamber, there is yet another chamber that collects any leakage through the viscoseals isolating the pumping chamber, and feeds it back to the pump. The melting chambers are generally wedge-shaped and wide enough to accept traditional solids feeding. The mixing chambers are parallel and the mixing blocks may come in a variety of shapes and be easily removed or replaced. Finally, the pump is wedge-shaped and narrow. The disks are hollow and can be temperature controlled with hot oil fed through the shaft via a rotary joint.

A 350-mm 12-chamber machine is shown in Fig. E9.7b. Unlike the case in the SSE described in the previous section, the journey of a polymer particle in a multichannel CDP is more predictable. Not only do the particles proceed through a sequence of chambers that is predetermined in the design stage, but in addition, each chamber is dedicated to a specific elementary step, as indicated in Example 9.7. This, of course, makes modeling and simulation easier.

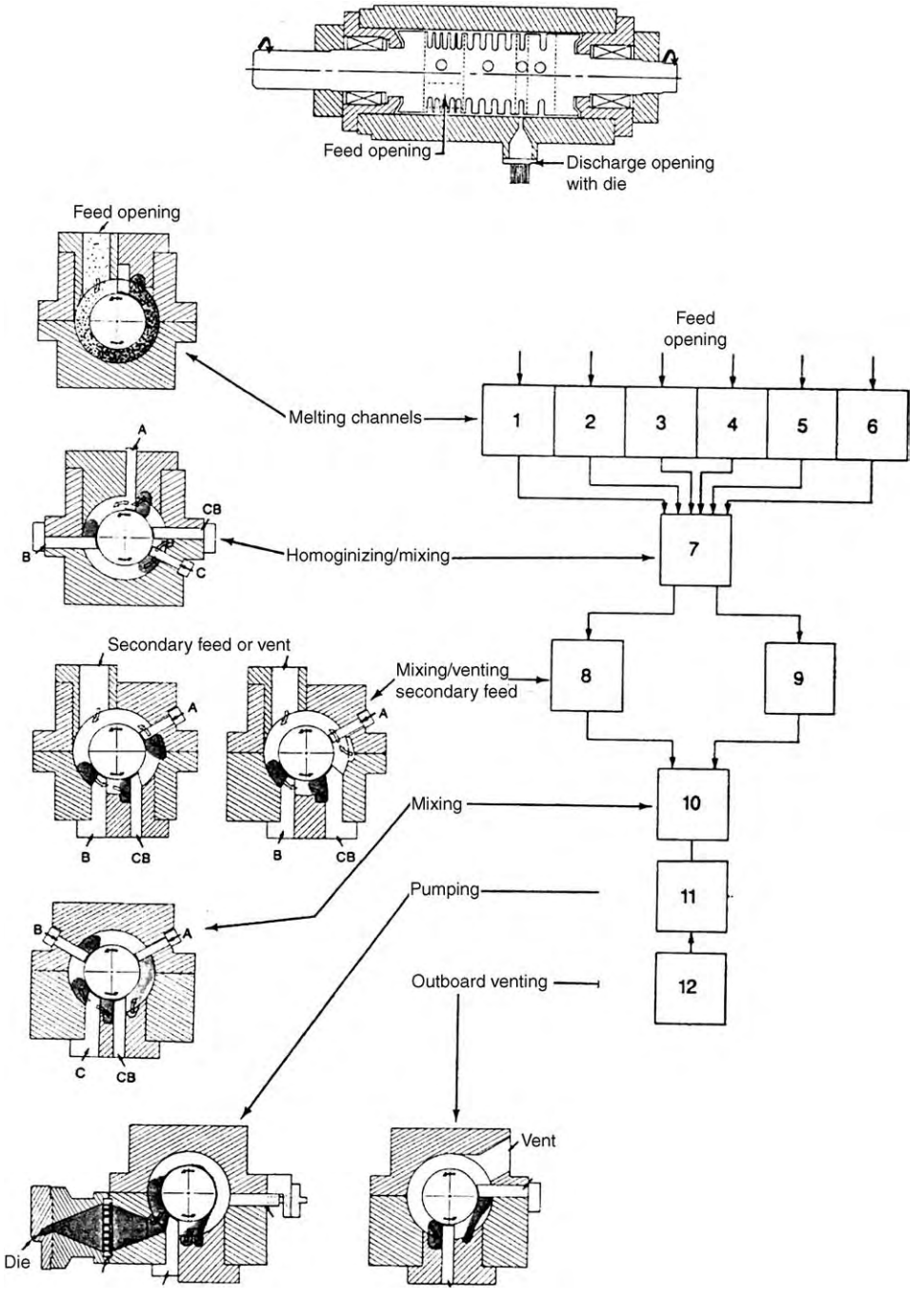

Fig. E9.7a A schematic but representative design of a 350-mm-diameter, 12-chamber Diskpack compounder. The rotor is shown at the top and the cross section of each separate chamber is shown in the sequence of the processing path. Each cross section shows the housing, the inlet and outlet, and the various inserts attached to the housing. [Courtesy of Farrel Corporation, Ansonia, CT.]

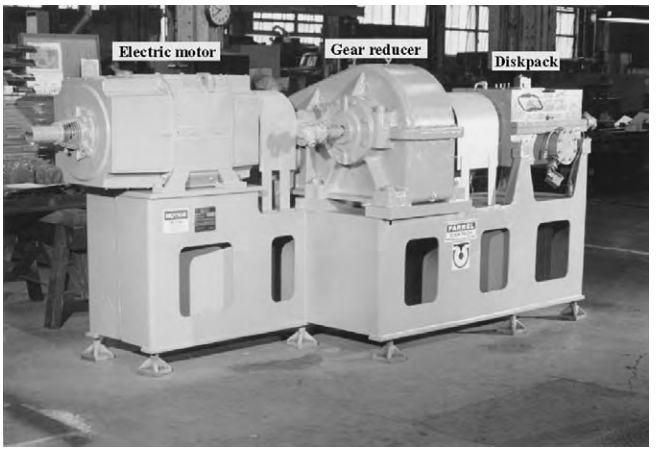

Fig. E9.7b Photograph of a 350-mm-diameter co-rotating disk Diskpack[16] compounder manufactured by the Farrel Corporation with a tested production capacity of 3000 lb/h. [Courtesy of Farrel Corporation, Ansonia, CT.]

Plasticating First we observe that, in a CDP, there is no solids conveying section or chamber, because the disks are heated and the pellets that come in contact with the rotating disks quickly melt. The solids are compressed into a solid bed as in the SSE, occupying $2\pi\varepsilon$ of the circumference, as shown in Fig. 9.46.

We invoke the drag removal melting mechanism with thin films of melt created at the hot disk surfaces. The thickness of the film grows toward the exit, as shown in Fig. 9.47,

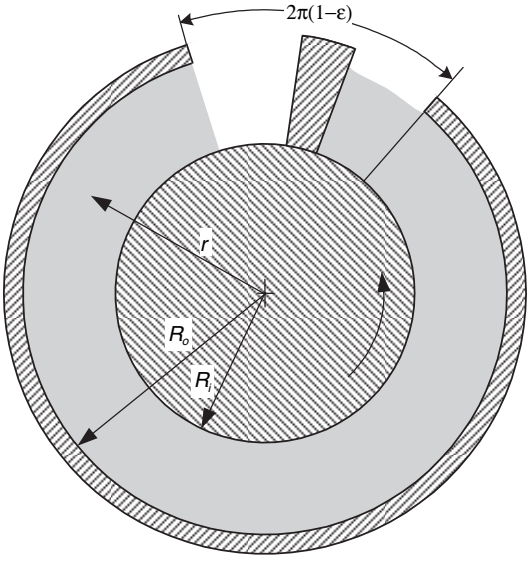

Fig. 9.46 A co-rotating disk melting chamber with solids filling up much of the channel.

16. This particular Diskpack machine had only four melting chambers.

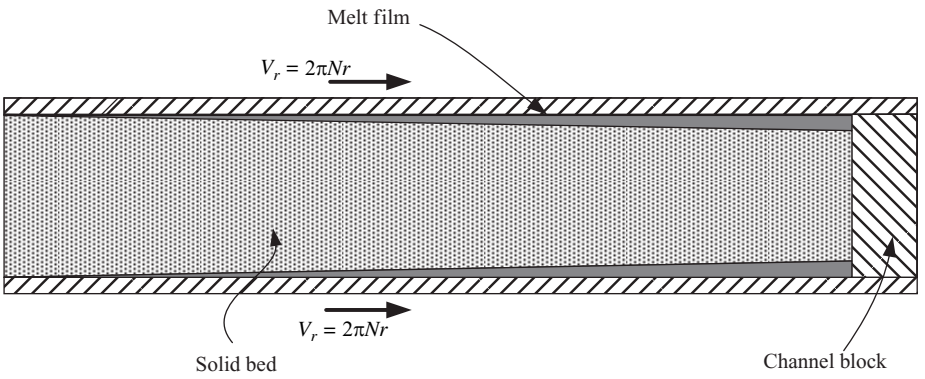

Fig. 9.47 Schematic representation of the drag removal melting mechanism along a plane of constant radius. Pressure builds by the drag exerted by the rotating disks with a maximum value at the channel block. The melt from the melt pool is discharged radically into a transfer channel to the next chamber.

which depicts schematically the solid bed along a constant radius. Pressure builds toward the channel block and, consequently, the melt in the exit region acquires a radial velocity component toward the exit. This melting model was experimentally observed by Tadmor et al. (50) for LDPE, HDPE, and Polypropylene (PP) with pelletized feed, using a freezing technique similar to the one used for elucidating the melting mechanism in SSEs.

We now derive a simple mathematical model for calculating the rate of melting in a melting chamber. The outer and inner radii of the disk are R_o and R_i, respectively, and the gap between them is H; the solid bed occupies $2\pi\varepsilon$ of the circumference; the disk speed N is constant, the disk temperature is T_d; the molten polymer is Newtonian with constant viscosity μ; the solids and melt have densities and specific heat ρ_s, c_s and ρ_m, c_m, respectively; the melting point is T_m; and the heat of fusion is λ. We now turn to Eq. 5.7-36, with W replaced by $2\pi r\varepsilon$, and the velocity V_0 by $2\pi rN$, to get the *rate of melting per unit distance in the r direction* (kg/(s·m))

$$\begin{aligned}\omega_r &= 2\left\{\frac{4\varepsilon\pi^2 r^2 N\rho_m[k_m(T_d - T_m) + 2\pi^2 r^2 N^2\mu]}{\lambda + C_s(T_m - T_s)}\right\}^{1/2} \\ &= 4\pi r\sqrt{\frac{\varepsilon N\rho_m}{\lambda + C_s(T_m - T_s)}}\sqrt{[k_m(T_d - T_m) + 2\pi^2 r^2 N^2\mu]}\end{aligned} \tag{9.4-1}$$

The *total rate* of *melting* (kg/s) is given by integrating ω_r:

$$\omega_T = \int_{R_i}^{R_o} \omega_r\, dr \tag{9.4-2}$$

Substituting Eq. 9.4-1 into Eq. 9.4-2 and integration, results in:

$$\begin{aligned}\omega_T = {} & \frac{2}{3\mu\pi N^2}\sqrt{\frac{\varepsilon\rho_m N}{\lambda + C_s(T_m - T_s)}} \\ & \left\{\left[2\mu\pi^2 N^2 R_0^2 + k_m(T_d - T_m)\right]^{3/2} - \left[2\mu\pi^2 N^2 R_i^2 + k_m(T_d - T_m)\right]^{3/2}\right\}\end{aligned} \tag{9.4-3}$$

Example 9.8 The Melting Rate in a Co-rotating Disk Chamber In this example we calculate the rate of melting of LDPE in a parallel chamber of width 0.75 in, outer radius of 3.75 in, inner radius 2.25 in as a function of disk speed with disk temperature set at 450°F. The viscosity is 0.035 $lb_f s/in^2$, the melting point is 231°F, the heat of fusion is 55.8 Btu/lb, the thermal conductivity of the melt is 0.105 Btu/ft°F·h, the specific heat of the melt and solids are 0.62 and 0.66 Btu/lb°F, respectively, and the solids and melt densities are 57 and 48 lb/ft^3, respectively.

Solution Substituting the given parameters into Eq. 9.4-3 in suitable units and assuming an inlet temperature of 86°F gives:

$$\omega_T = \frac{2 \times 60^2}{(3\pi \times 0.036 \times N^2)} \left[\frac{0.75 \times 48N\left(\frac{1}{12^3 \times 60}\right)}{(55.8 + 0.66 \times (231 - 86)) \times 60244} \right]^{1/2}$$
$$\left\{ \left[2 \times 0.036\pi^2 \times 3.75^2 N^2 \left(\frac{1}{60}\right)^2 + 0.105 \times (400 - 231)\left(\frac{60244}{12 \times 3600}\right) \right]^{1/2} \right.$$
$$\left. - \left[2 \times 0.036\pi^2 \times 2.25^2 N^2 \left(\frac{1}{60}\right)^2 + 0.105 \times (400 - 231)\left(\frac{60244}{12 \times 3600}\right) \right]^{1/2} \right\}$$

This can be rewritten as

$$\omega_T = 0.13088787 N^{-3/2} \left\{ \left[27.75826 \times 10^{-4} N^2 + 24.746059 \right]^{1/2} \right.$$
$$\left. - \left[9.992974 \times 10^{-4} N^2 + 24.746059 \right]^{1/2} \right\}$$

The rate of melting versus disk speed is shown in Fig. E9.8

However, experimental studies (50), using either powder feed or pelletized feed with some recycled melt over the channel block into the feed port, have not exhibited drag removal melting but a dissipative mix–melting mechanism, discussed in Chapter 5. As

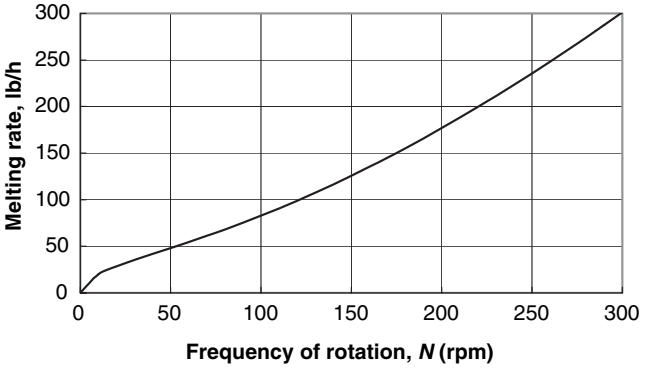

Fig. E9.8 Simulated rates of melting of LDPE in a 7.5-in-diameter co-rotating disk as a function of disk speed with the disk temperature as a parameter.

pointed out there, this melting mechanism is very efficient, although it creates a nonuniform plasticated melt with some entrapped air bubbles. The entrapped bubbles, however, can be removed in downstream chambers that also homogenize the melt. The interesting point is that, unlike in other machines, in this machine the dissipative mix–melting mechanism can be triggered by enabling melt recycle, at a desired rate, which is determined by the radial clearance of the channel block.

Mixing The extensive mixing in a co-rotating disk chamber was studied both theoretically and experimentally. The velocity profiles as predicted by the theoretical model described in Section 6.6 were verified experimentally (52), and the evolution of the interfacial area was studied using color tracers (53).

The velocity profile in a parallel channel given in Eq. 6.6-23 can be written in dimensionless form in terms of the pressure and drag flow rates as follows (52):

$$u_\theta = 1 - \frac{[(s+2)/(s+1)](R_d/r)^{s+2}\left(Q_p/Q_d\right)}{2\{(\alpha^{1-s}-1)/[(s-1)(1-\alpha^2)]\}}\left(1-\xi^{s+1}\right) \tag{9.4-4}$$

where $u_\theta = v_\theta/2\pi Nr$ is the dimensionless velocity, $\xi = 2z/H$, $s = 1/n$, where n is the Power Law exponent, $\alpha = R_s/R_d$, and Q_d and Q_p are the drag- and pressure-flow rates given by

$$Q_d = \pi NHR_d^2\left(1-\alpha^2\right) \tag{9.4-5}$$

and

$$Q_p = \frac{H^2R_d}{2(s+2)}\frac{(\alpha^{1-s}-1)}{(s-1)}\left[\frac{H}{2mR_d}\frac{\partial P}{\partial \theta}\right]^s \tag{9.4-6}$$

Mixing chambers are relatively wide and, therefore, the pressure and drag flows are close to each other. A good feel for the mixing condition can be obtained by examining the velocity profiles at various radial positions, as shown in Fig. 9.48. Clearly, the disks drag the fluid toward the channel block, where it must turn around and flow backward in the

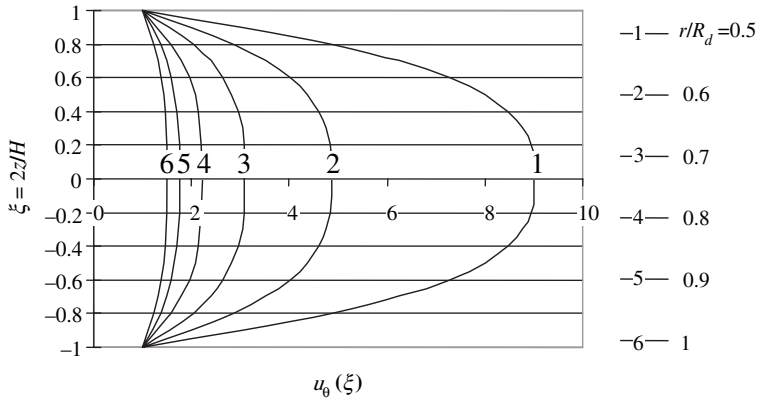

Fig. 9.48 Velocity profiles for a Power Law model fluid with $s = 2$, $\alpha = 0.5$ at various r/R_d values: 0.5, 0.6, 0.7, 0.8, 0.9, and 1.0, with $Q_p/Q_d = -1$.

center region of the channel. This circulatory flow at a fixed radius induces good extensive mixing. In a wedge-shaped chamber, under closed discharge conditions, fluid particles in a certain radial position stay at that plane. But in a parallel channel above a certain critical radius r^*, there is a net forward flow, whereas, below that value, there is a net backflow. The critical radius is given by

$$r^* = R_d \left[\frac{1}{2} \left(\frac{2n+1}{(n+1)} \right) \left(\frac{Q_p}{Q_d} \right) \frac{(1-s)(1-\alpha^2)}{(1-\alpha^{-s})} \right]^{n/(n+1)} \tag{9.4-7}$$

This implies that, superimposed on the circulatory flow at a fixed radius, there is an overall circulation perpendicular to the constant r plane. This overall circulation helps in randomizing the composition non-uniformity.

David and Tadmor (54) studied experimentally the evolution of the interfacial area using Thiokol rubber with a color tracer, and their findings are shown in Fig. 9.49. At one

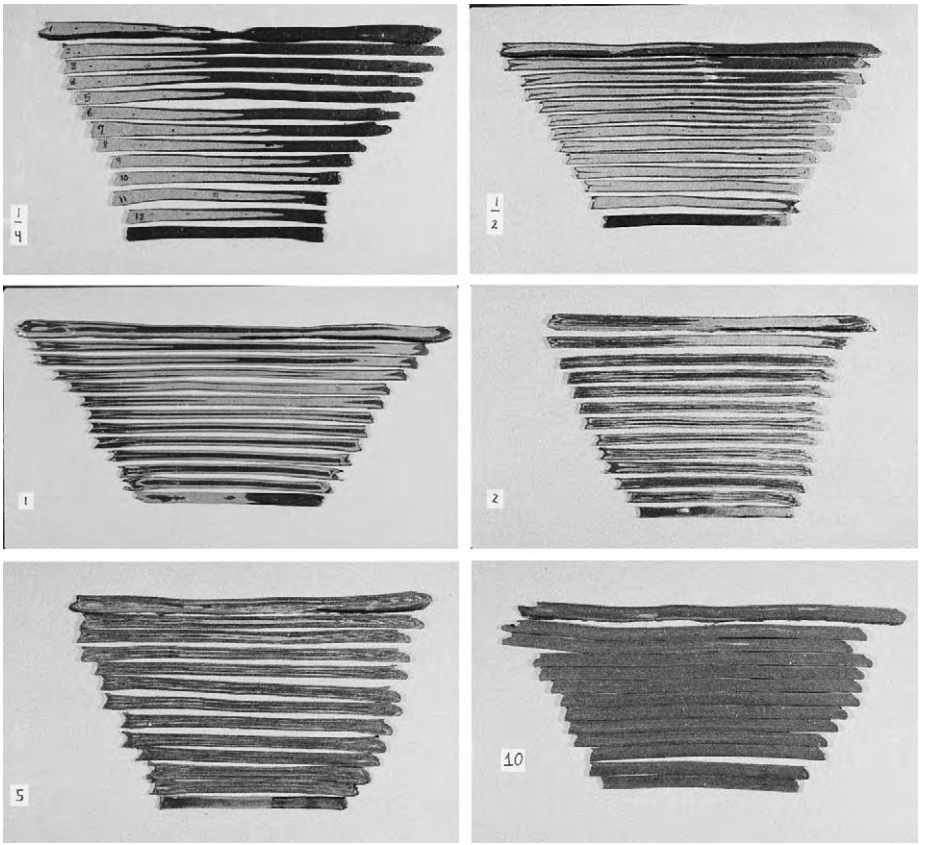

Fig. 9.49 The evolution of the interfacial area of a viscous Thiokol rubber in a 26.6-cm parallel-disk mixing chamber with $\alpha = 0.5$, with the number of turns. The rubber filled up half the chamber with one-quarter cream color (at the channel block at the left side) and one-quarter black. The numbers on the figure indicate the number of turns from 1/4 to 10. [Reprinted by permission from B. David and Z. Tadmor, ''Laminar Mixing in Co-rotating Disk Processors,'' *Int. Polym. Process.*, **3**, 38–47 (1988).]

quarter of a turn, the disks drag the black material at the disk surfaces all the way to the channel. At half a turn, the black material turns around and begins to penetrate the cream material, creating new striations and interfacial area. At one turn, the black material at the center reaches the feed end. With increasing turns we observe more striations and, due to the overall circulation, we notice, for example, at five turns, more black in the lower regions. After only 10 turns, the mixture appears homogeneous to the naked eye. The smaller the melt pool, the more striations will be created for the same number of turns.

Dispersive mixing requires high shear stresses. These can be obtained by inserting shearing pins into the chamber with a prescribed clearance and shape, where the number of passages over the high shear region (at no recycle) equals the number of pins (55).

Devolatilizing Devolatilization in a co-rotating disk chamber can be achieved by spreading the melt on the disk surfaces in a chamber under high vacuum, and collecting the foamed film in a circulating pool at the channel block where bubble rupture takes place. The partly devolatilized melt can then be fed into another chamber in series, and so on. Fig. 9.50 shows a setup of three consecutive devolatilizing chambers.

The separation efficiency of a single chamber is given by

$$\varepsilon = 1 - \frac{c_{\text{out}} - c_e}{c_{\text{in}} - c_e} \tag{9.4-8}$$

where c_{out} and c_{in} are the exit and inlet concentrations, respectively, and c_e is the equilibrium concentration at the imposed vacuum level. In a multiple-chamber setup with identical conditions in each, it is easy to show that the overall separation efficiency is given by

$$E_n = 1 - (1 - \varepsilon)^n \tag{9.4-9}$$

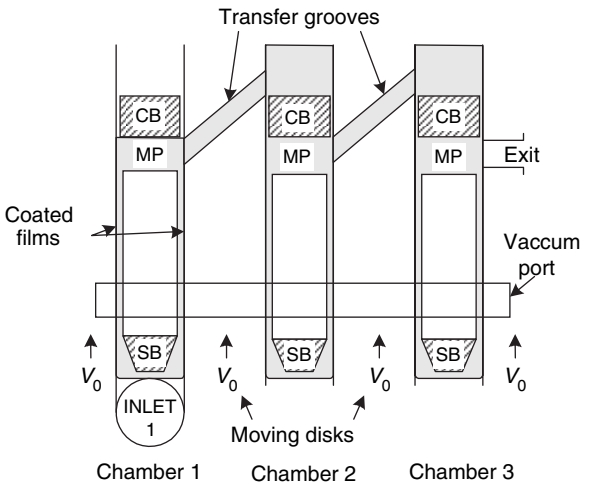

Fig. 9.50 Schematic view of a three-chamber co-rotating disk devolatilizer. The molten inlet feed is deposited on the disk surface of the first chamber by a spreading block (SB). The film is exposed to vacuum via the vacuum port. The melt is collected at the channel block (CB) and forced to flow over the top of the disk to the feed port of the second chamber. Similarly, the melt is fed into the third chamber from where the devolatilized melt exists.

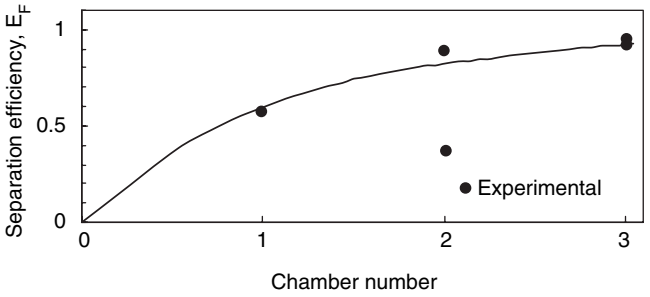

Fig. 9.51 Separation efficiency in consecutive chambers of 450°F PS melt fed at 42 lb/h into 0.54-in-wide chambers at 50-torr absolute pressure, with disks rotating at 30 rpm. [Reprinted by permission from P. S. Mehta, L. N. Valsamis, and Z. Tadmor, "Foam Devolatilization in a Multichannel Co-rotating Disk Processor," *Polymer Process Eng*., **2**, 103–128 (1984).]

Devolatilization in a co-rotating disk chamber was studied by Mehta et al. (56). They used a melt-fed, 7.5-in-diameter co-rotating disk devolatilizer, with three 1-in-wide chambers connected in series, and with $\alpha = 0.566$ and $\varepsilon = 93°$ as shown in Fig. 9.50. The polymer devolatilized was polystyrene (PS) with 1500–3000 ppm styrene. Figure 9.51 shows the efficiency of separation in the consecutive chambers. The efficiencies measured were 58%, 88%, and 94%, in one, two, and three chambers, respectively. These results conform reasonably well with Eq. 9.4-9.

Finally, Fig. 9.52 shows the overall efficiency of separation as a function of disk speed with flow rate as a parameter. Efficiency increases with flow rate (in spite of decreasing residence time), just as SSEs and TSEs, indicating that foaming, which was visually observed to take place, is quick, and the increased separation is most likely due to better bubble rupture and volatile release in the highly sheared melt pools.

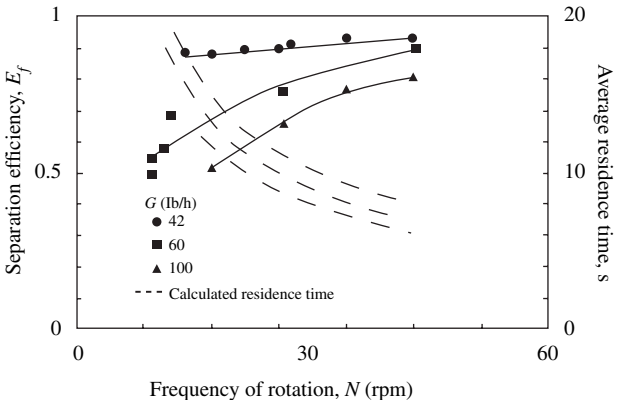

Fig. 9.52 Separation efficiency of a three-chamber co-rotating disk devolatilizer of 450°F PS melt containing 1500–3000 ppm styrene, fed at 42-lb/h into 0.54-in-wide chambers at 50-torr absolute pressure, as a function of disk speed and with flow rate as a parameter. Broken curves show calculated residence times. [Reprinted by permission from P. S. Mehta, L. N. Valsamis, and Z. Tadmor, "Foam Devolatilization in a Multichannel Co-rotating Disk Processor," *Polym. Process. Eng*., **2**, 103–128 (1984).]

REFERENCES

1. Z. Tadmor and I. Klein, *Engineering Principles of Plasticating Extrusion*, Reinhold, New York, 1970; (a) p. 234; (b) p. 310; (c) p. 328; (d) Chapters 6 and 8; (e) p. 186; (f) p. 90; (g) p. 133.
2. M. L. Booy, ''Influence of Oblique Channel Ends on Screw Pump Performance,'' *Polym. Eng. Sci*., **7**, 5–16 (1967).
3. R. E. Colwell and K. R. Nicholls, ''The Screw Extruder,'' *Ind. Eng. Chem*., **51**, 841–843 (1959).
4. R. M. Griffith, ''Fully Developed Flow in Screw Extruders,'' *Ind. Eng. Chem. Fundam*., **1**, 180–187 (1962).
5. H. Zamodits and J. R. A. Pearson, ''Flow of Polymer Melts in Extruders. Part I. The Effect of Transverse Flow and of Superposed Steady Temperature Profile,'' *Trans. Soc. Rheol*, **13**, 357–385 (1969); see also B. Martin, J. R. A. Pearson, and B. Yates, ''On Screw Extrusion. Part I. Steady Flow Calculations,'' University of Cambridge, Department of Chemical Engineering, Polymer Processing Research Center, Report No. 5, 1969.
6. B. Yates, ''Temperature Development in Single Screw Extruders,'' Ph.D. Thesis, University of Cambridge, Cambridge, 1968.
7. R. T. Fenner, ''The Design of Large Hot Melt Extruders,'' *Polymer*, **16**, 298–304 (1975).
8. R. T. Fenner, in *Computational Analysis of Polymer Processing*, J. R. A. Pearson, and S. M. Richardson, Eds., Applied Science, London, 1983.
9. B. Elbirli and J. T. Lindt, ''A Note on the Numerical Treatment of the Thermally Developing Flow in Screw Extruders,'' *Polym. Eng. Sci*., **24**, 482–487 (1984).
10. K. P. Choo, M. L. Hami, and J. F. T. Pittman, ''Deep Channel Operating Characteristics of Single Screw Extruder,'' *Polym. Eng. Sci*., **21**, 100–104 (1981).
11. D. Roylance, ''Use of Penalty Finite Element Analysis of Polymer Melt Processing,'' *Polym. Eng. Sci*., **20**, 1029–1034 (1980).
12. R. Y. Chang, C. W. Hsu, W. H. Yang, W. L. Yang, and D. C. Hsu, ''Three Dimensional Numerical Analysis of the Single Screw Plasticating Extrusion Process,'' *SPE ANTEC Tech. Papers.,* **47**, 173–175 (2001).
13. E. E. Agur and J. Vlachopoulos, ''Numerical Simulation of a Single Screw Plasticating Extruder,'' *Polym. Eng. Sci*., **22**, 1084–1094 (1982).
14. J. F. T. Pittman and K. Rashid, ''Heat Transfer in Recirculating Extruder Channel Flow,'' *J. Polym. Eng*., **5**, 1–48 (1985).
15. M. Viriyayuthakorn and B. Kassahun, ''A Three Dimensional Model for a Plasticating Extrusion Screw Design,'' *SPE ANTEC Tech. Papers*, **30**, 81 (1984).
16. S. Syrjälä, ''On the Analysis of Fluid Flow and Heat Transfer in the Melt Conveying Section of a Single Screw Extruder,'' *Num. Heat Trans*., Part A, **35**, 25–47 (1999).
17. I. Klein and Z. Tadmor, ''Operating Characteristics of a Plasticating Extruder,'' in *Computer Programs for Plastics Engineers*, I. Klein and D. I. Marshall, Eds., Reinhold, New York, 1968, Chapter 6.
18. S. Middleman, ''Flow of Power Law Fluids in Rectangular Ducts,'' *Trans. Soc. Rheol*., **9**, 83 (1965).
19. Z. Tadmor, ''Non-Newtonian Tangential Flow in Cylindrical Annuli,'' *Polym. Eng. Sci*., **6**, 202–212 (1966).
20. G. Pinto and Z. Tadmor, ''Mixing and Residence Time Distribution in Melt Extruders,'' *Polym. Eng. Sci*., **10**, 279–288 (1970).
21. D. Wolf and D. H. White, ''Experimental Study of the Residence Time Distribution in Plasticating Extruders,'' *AIChE. J*., **22**, 122–131 (1976).
22. M. Hirshberger, ''Two-Dimensional Non-Newtonian Flow in Rectangular Channels,'' M. S. Thesis, Department of Chemical Engineering, Technion–Israel Institute of Technology, Haifa, 1972.

23. D. Bigg and S. Middleman, ''Mixing in Screw Extruders: A Model for Residence Time Distribution and Strain,'' *Ind. Eng. Chem. Fundam.*, **13**, 66 (1974).
24. G. Lidor and Z. Tadmor, ''Theoretical Analysis of Residence Time Distribution Functions in Plasticating Screw Extruders,'' *Polym. Eng. Sci.*, **16**, 450–462 (1976).
25. I. Manas-Zloczower and Z. Tadmor, ''The Distribution of Number of Passes over the Flights in Single Screw Melt Extruders,'' *Adv. Plast. Tech.*, **3**, 213 (1983).
26. Z. Tadmor, ''Machine Invention, Innovation and Elementary Steps,'' *Adv. Polym. Technol.*, **21**, 87–97, (2002); also presented at the Fundamental Forums ''Invention and Innovation'' session at the 2001 ANTEC at Dallas, TX.
27. Z. Tadmor, ''Screw Elements Having Shearing and Scraping Devices,'' U.S. Patent 5,356,208, October 18, 1994; European Patent 0619173; German Patent 69327519.7-08, Great Britain Patent 133 19134 3.
28. W. H. Darnell and E. A. J. Mol, ''Solids Conveying in Extruders,'' *Soc. Plast. Eng. J.*, **12**, 20–28 (1956).
29. Z. Tadmor, ''Fundamentals of Plasticating Extrusion. I. A. Theoretical Model for Melting,'' *Polym. Eng. Sci.*, **6**, 185–190 (1966).
30. B. H. Maddock, ''A Visual Analysis of Flow and Mixing in Extruder Screws,'' *Tech. Papers, Vol. V, 15th Annu. Tech. Conf.*, Society of Plastics Engineers, New York, January 1959; also, B. H. Maddock, ''A Visual Analysis of Flow and Mixing in Extruder Screws,'' *SPE J.*, **15**, 383–389 (1959).
31. Z. Tadmor, I. J. Duvdevani, and I. Klein, ''Melting in Plasticating Extruders—Theory and Experiments,'' *Polym. Eng. Sci.*, **7**, 198–217 (1967).
32. G. Menges and K. P. Klenk, ''Melting and Plasticating of Unplasticized PVC Powder in the Screw Extruder,'' *Kunststoffe (German Plastics)*, **57**, 598–603 (1967).
33. J. T. Lindt, ''A Dynamic Melting Model for Single Screw Extruders,'' *Polym. Eng. Sci.*, **16**, 284–291 (1976).
34. L. Kacir and Z. Tadmor, ''Solids Conveying in Screw Extruders. Part I. The Delay Zone,'' *Polym. Eng. Sci.*, **12**, 387–395 (1972).
35. E. Broyer and Z. Tadmor, ''Solids Conveying in Screw Extruders. Part I. A Modified Isothermal Model,'' *Polym. Eng. Sci.*, **12**, 12–24 (1972).
36. K. Schneider, ''Technical Report on Plastics Processes in the Feeding Zone of an Extruder'' (in German), Institute of Plastics Processing (IKV), Aachen, Germany, 1969.
37. Z. Tadmor and E. Broyer, ''Solids Conveying in Screw Extruders. Part II. Non Isothermal Model,'' *Polym. Eng. Sci.*, **12**, 378–386 (1972).
38. J. G. A. Lovegrove and J. G. Williams, ''Solids Conveying in a Single Screw Extruders: the Role of Gravity Forces,'' *J. Mech. Eng. Sci.*, **15**, 114–122 (1973); also, ''Solids Conveying in a Single Screw Extruder: a Comparison of Theory and Experiments,'' *J. Mech. Eng. Sci.*, **15**, 195–199 (1973).
39. J. G. A. Lovegrove and J. G. Williams, ''Pressure Generation Mechanism in the Feed Section of Screw Extruders,'' *Polym. Eng. Sci.*, **14**, 589–594 (1974).
40. F. Zhu and L. Chen, ''Studies on the Theory of Single Screw Plasticating Extrusion. Part I: A New Experimental Method for Extrusion,'' *Polym. Eng. Sci.*, **31**, 1113–1116 (1991).
41. C. I. Chung, ''New Ideas About Solids Conveying in Screw Extruders,'' *Soc. Plast. Eng.*, **26**, 32–44 (1970).
42. C. I. Chung, ''A New Theory for Single Screw Extrusion. Part I and Part II,'' *Mod. Plast.*, **45**, 178 (1968).
43. R. Hinrich and L. U. Lilleleht, ''A Modified Melting Model for Plasticating Extruders,'' *Polym. Eng. Sci.*, **10**, 268–278 (1970).

44. R. C. Donovan, "A Theoretical Melting Model for Plasticating Extruders," *Polym. Eng*., **11**, 247–257 (1971).
45. J. R. Vermeulen, P. G. Scargo, and W. J. Beek, "The Melting of a Crystalline Polymer in a Screw Extruder," *Chem. Eng. Sci*., **26**, 1457–1465 (1971).
46. I. R. Edmundson and R. T. Fenner, "Melting of Thermoplastics in Single Screw Extruders," *Polymer*., **16**, 48–56 (1975).
47. J. Shapiro, A. L. Halmos, and J. R. A. Pearson, "Melting in Single Screw Extruders," *Polymer*., **17**, 905–918 (1976).
48. I. Klein and Z. Tadmor, "Operating Characteristics of a Plasticating Extruder," in *Computer Programs for Plastics Engineers*, I. Klein and D. I. Marshall, Eds., Reinhold, New York, 1968, Chapter 6, Secs. 1 and 2.
49. Z. Tadmor and I. Klein, "Design of Certain Fluted Mixing Sections of Extruder Screws," *Polym. Eng. Sci*., **13**, 382–389 (1973).
50. Z. Tadmor, U.S. Patents 4,142,805 and 4,194,841.
51. Z. Tadmor, P. Hold, and L. N. Valsamis, "A Novel Polymer Processing Machine—Theory and Experimental Results," *SPE ANTEC Tech. Papers.*, **25**, 193–202 (1979).
52. P. Hold, Z. Tadmor, and L. N. Valsamis, "Applications and Design of a Novel Polymer Processing Machine", *SPE ANTEC Tech. Papers.*, **25**, 205–211 (1979).
53. I. Edelist and Z. Tadmor, "Velocity Profiles in Corotating Disk Processors," *Polym. Process. Eng*., **1**, 1 (1983).
54. B. David and Z. Tadmor, "Extensive Mixing in Corotating Processors," *Int. Polym. Process*., **3**, 38–47 (1988).
55. L. N. Valsamis, A. M. Mekkaui, G. S. Donoian, P. S. Mehta, and Z. Tadmor, "Mixing, Dispersion and Blending in Corotating Disk Processors," *SPE ANTEC Tech. Papers.*, **30**, 987–992 (1984).
56. P. S. Mehta, L. N. Valsamis, and Z. Tadmor, "Foam Devolatilization in a Multichannel Corotating Disk Processor," *Polym. Process Eng*., **2**, 103–128 (1984).

PROBLEMS

9.1 ***Analysis of a Melt Extrusion Process*** Consider the extrusion process shown in Fig. 9.2 for pelletizing 8000 kg/h of polymer melt. The 40-cm-diameter and 12 L/D extruder has a square-pitched metering-type screw. The feed section is three turns long and 7.5 cm deep, and the metering section is six turns long and 2.5 cm deep. The flight width is 3 cm and the flight clearance is negligible. Neglecting the breaker plate and screen pack, the die consists of a 3-cm-thick pelletizing plate with 1000 holes over its surface of geometry, shown in Fig. 9.2, with $l_1 = l_2 = l_3 = 1$ cm, $R_1 = 0.5$ cm, and $R_2 = 0.25$ cm. The extruded polymer is an incompressible Newtonian fluid with a viscosity of 10^3 Ns/m^2 and a density of 0.75 g/cm^3. Calculate (a) the screw speed needed to obtain the required output and the resulting head pressure; (b) the power; and (c) the mean strain and residence time in the extruder. In addition, (d) specify if the isothermal assumption is valid, and (e) estimate the minimum size of a tubular inlet conduit for gravitational feeding.

9.2 ***Design of a Melt Extruder*** Design a 300-lb/h extruder pumping molten nylon at 400°F to generate 1200 psi head pressure. Assume a constant channel depth screw with axial length of 10 in. The melt density is 62.0 lb/ft^3, the viscosity is 0.38 lb$_f$·s/in^2, and the specific heat is 0.35 Btu/lb°F.

9.3 ***The Superposition Correction Factor*** Combined drag and pressure flow between parallel plates (or concentric cylinders[17]) of a Newtonian fluid at isothermal conditions leads to a flow-rate expression that is the linear sum of two independent terms, one for drag flow and another for pressure flow:

$$Q = Q_d + Q_p$$

The former vanishes when the velocity of the moving plate is zero, and the latter vanishes in the absence of a pressure gradient. (a) Explain on physical and mathematical grounds why the solution of the same flow problem with a non-Newtonian fluid, for example, a Power Law model fluid, no longer leads to the same type of expressions. (b) It is possible to define a superposition correction factor ε as follows

$$Q = \varepsilon\left(Q_d^* + Q_p^*\right)$$

where Q_d^* and Q_p^* are *hypothetical* drag and pressure flow terms, each calculated with a Power Law model, assuming the other equals zero. Thus, $Q_d^* = Q_d$ as the pure drag flow term, and Q_p^* is the pure pressure flow term of a Power Law model fluid. Show that ε in parallel-plate flow is a function of only Q/Q_d and n. Restrict your analysis to a positive-pressure gradient and no extremum in the velocity profile. (c) Explain how, by using a generalized plot of E, one can calculate in a straightforward manner the pressure gradient for a given geometry, plate velocity, and net flow-rate requirement.

9.4 ***Viscous Seals*** Vertical extruders with the feed end of the screw protruding into the hopper at the top, and the drive attached to the discharge end of the screw at the bottom, have the advantage of good feeding and high torque input capability. This is because the drive is on the side where the channel depth is shallow, and consequently the root of the screw has a higher diameter; however, it has the disadvantage of leakage at the high pressure end, because the screw at the discharge end becomes a shaft attached to a drive. The shaft rotates in a slider bearing where substantial leakage can occur, depending upon the clearance. One way to reduce the leakage or stop it completely is to cut a reverse flight on the shaft. Thus, the bearing with the shaft turns into a screw extruder that pumps the leaking polymer melt back into the high-pressure discharge region. This is called a *viscous dynamic seal***.** This design can be viewed as two extruders pointing head-on to each other. The main extruder has a certain throughput and generates a pressure P; the dynamic seal, if no leakage is allowed, generates the same P at zero flow-rate condition. Design a dynamic seal on a 2-in shaft to prevent leakage for $P = 1000$ psi. Assume a Newtonian fluid of viscosity 0.05 $\text{lb}_\text{f}\cdot\text{s/in}^2$ and isothermal conditions.

9.5 ***Solids Conveying of Nylon in Screw Extruders*** Consider a 1.991-in-diameter screw with 2-in lead, 1.375-in root diameter, and 0.2-in flight width, conveying nylon pellets with bulk density of 0.475 g/cm^3 and a coefficient of friction of 0.25. Assuming no pressure rise, calculate the solids conveying rate (g/rev) at the following conditions: (a) no friction between the screw and the solids; (b) no friction

17. Z. Tadmor and I. Klein, *Engineering Principles of Plasticating Extrusion*, Van Nostrand–Reinhold, New York, 1970, p. 323.

on the screw flights; (c) no friction on the trailing flight; and (d) friction on all contacting surfaces. (e) Compare the experimentally measured value by Darnell and Mol (28) of 14.9 g/rev with your results.

9.6 ***Solid Bed Profile in Screw Extruders*** Determine the solid-bed profile and length of melting of LDPE extruded in a 2.5-in-diameter, single flighted screw extruder with the following screw geometry and operating conditions: Feed section, 3.2 turns and 0.5-in channel depth; compression section, 12 turns with linear taper; and metering section, 12 turns and 0.125-in channel depth. The flight width is 0.25 in and the flight clearance is negligible. The operating conditions are 82 rpm screw speed, 150°C constant barrel temperature, and 120-lb/h flow rate. Use the polymer physical property data in Example 9.6 and assume that melting starts one turn before the end of the feed section.

9.7 ***The Rotating Flight Extruder*** The flight on the screw forms a helical spiral. Consider a processing machine consisting of a detached flight freely rotating on a smooth shaft in a lightly fitted barrel. The difference between this ''extruder'' and the conventional one is that the root of the screw is stationary relative to the flights, just like the barrel. (a) Derive a theoretical model for pumping (equivalent to the simple Newtonian melt SSE model). (b) Derive a theoretical model for melting (equivalent to the simple Newtonian melting model in screw extruders), assuming that screw temperature in this zone equals the barrel temperature. (c) Derive a theoretical model for solids conveying. (d) How do the theoretical predictions of the rotating flight extruder compare to an equivalent size screw extruder? (e) Discuss the engineering feasibility of the rotating flight extruder.

9.8 ***Wiped Surface and Heat Transfer Surface*** The accompanying figure shows the cross section of an SSE, a co-rotating intermeshing TSE, and a co-rotating disk processor. (a) Show the surfaces that the polymer comes in contact with. (b) Which of these surfaces are ''wiped''. (c) Which of them are temperature controlled? (d) Based on your findings, analyze the advantages and disadvantages of these machines regarding the risk of polymer degradation and efficiency of temperature control.

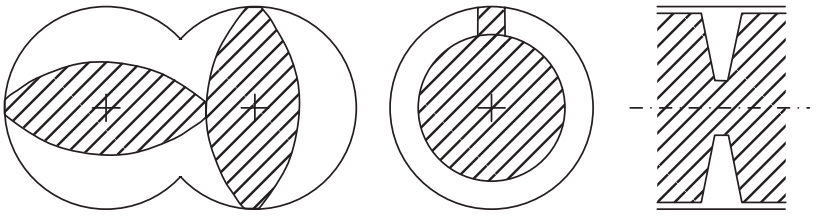

Twin screw Single screw Corotating disk

9.9 ***Melting in a Jointly Moving, Parallel Plate Configuration*** Figure 9.47 is also a schematic representation of a jointly moving, parallel-plate melter. Derive a mathematical model for this device, assuming that the plates are at constant temperature T_b, the melting process is steady (i.e., the molten polymer is continuously removed), the plate velocity is V_b, the molten material is Newtonian, and physical and thermophysical properties are constant and temperature independent.

9.10 ***Melting in a Co-rotating Disk Chamber*** Calculate the rate of melting in kg/s of a polymer fed at room temperature into a co-rotating disk chamber with an outer

diameter of 175 mm and an inner diameter of 100 mm, with $\varepsilon = 0.75$ rotating at 100 rpm and disk temperature 230°C. The melting point is 130°C, Newtonian viscosity of the melt is 400 Ns/m^2, the heat of fusion is 200 kJ/kg, the thermal conductivity is 0.101 J/m·s·°C, the melt density is 950 kg/m^3, and the specific heat of the solid is 2.3 kJ/kg°C.

9.11 ***Co-rotating Disk Scraped-surface Heat Exchanger***[18] (see accompanying figure) The heating and cooling of very viscous liquids is carried out in scraped-surface heat exchanges, in which the viscous liquid is deposited on the heat transfer surfaces and is repeatedly scraped and replaced by fresh material. A co-rotating disk processor chamber in which a viscous liquid or polymeric melt is deposited by a spreader on the disk surfaces and then scraped off by the channel block is, in fact, a scraped-surface heat exchanger (see photo below). (a) Show that the heat-transfer surface to volume ratio of a double-pipe heat exchanger is given by $A/V = 2/R$, where R is the radius of the heat-transfer surface. (b) Show that, for a multiple-disk co-rotating scraped-surface heat exchanger, the heat transfer to volume surface is $A/V = [2(1 - \alpha^2)/l] + (1 - \alpha)/R$, where α is the shaft radius to barrel radius and l is the axial separation between centerlines. (c) Compare the surface-to-volume ratios of (a) and (b) for a 20-cm-radius heat exchanger with $l = 3$ cm and $\alpha = 0.5$. (d) Assuming the molten film deposited on the disk is a semi-infinite medium, show that the heat-transfer coefficient is given by $h_i = 2\left(k\rho C_p N/\pi\right)^{1/2}$ (e) Plot the heat transfer coefficient for $k = 0.10$ Btu/hr·ft°F, $C_p = 0.46$ BTU/lb·°F, $\rho = 48$ lb/ft^3.

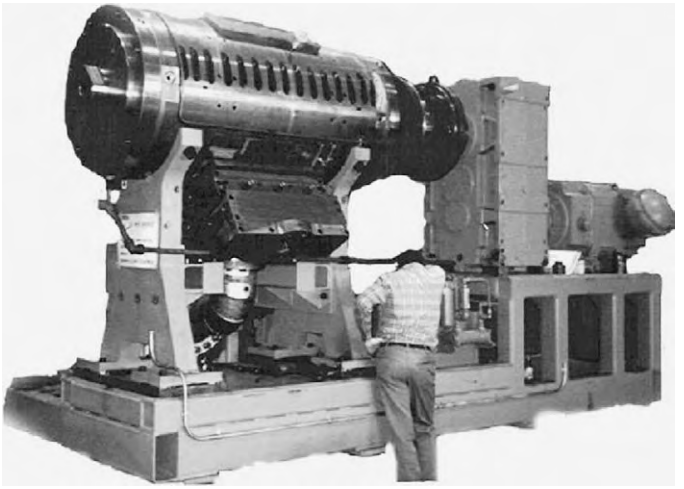

Photograph of a 550-mm-diameter Diskpack scraped-surface heat exchanger designed for reducing melt temperature from 400°F to 250°F for high Melt Index (MI) PE at 6000 lb/h. All 10 chambers were fed in parallel. The hot melt was spread on the cooled disk walls by self-adjusting floating spreaders. [Courtesy of the Farrel Corporation, Ansonia, CT.]

18. Z. Tadmor, "Co-rotating Disk Scraped-Surface Heat Exchanger," *Food Technol*., **39**, 67–74 (1985).